Ingénierie des interactions cellule/ matrice extracellulaire et cellule/cellule pour contrôler le comportement d'écoulements de suspensions de cellules à hautes fractions volumiques

Benoît Maisonneuve

THE UNIVERSITY OF QUEENSLAND
AUSTRALIA

UNIVERSITÉ DE GRENOBLE

THESIS

Submitted for the degree of

DOCTEUR DE L'UNIVERSITÉ DE GRENOBLE

Specialty : **Mécanique des fluides, Energétique, Procédés**
Arrêté ministériel : 7 août 2006

And of

DOCTOR OF PHILOSOPHY AT THE UNIVERSITY OF QUEENSLAND

Specialty : **Bioengineering**

Presented by

Benoît G.C. MAISONNEUVE

Thesis directed by **Denis C.D. ROUX** and
codirected by **Justin J. COOPER-WHITE**

prepared in the **Laboratoire Rhéologie et Procédés**
in the **École Doctorale I-MEP2**
and in the **Tissue Engineering and Microfluidic Laboratory**
in the **Australian Institute for Bioengineering and Nanotechnology**

Engineering cell/matrix and cell/cell interactions to control the flow behavior of high volume fraction cell suspensions

Thesis defended publicly on the **Monday 2nd of December**
In front of the jury:

Mr. Peter FISCHER	
Prof., ETH Zurich	Referee
Mr. Gareth McKINLEY	
Prof., MIT,	Referee
Mr. François MOLINO	
Assoc. Prof., Université Montpellier II	Examiner
Mr. Claude VERDIER	
Research Director, CNRS – UMR5588	Examiner
Mr. Denis ROUX	
Assoc. Prof., UJF	PhD director
Mr. Justin COOPER-WHITE	
Prof., University of Queensland	PhD co-director

Abstract

With the rapidly growing interest in the development of bioprocess systems to culture and expand mesenchymal stromal cells (MSCs) for cell therapy and regenerative medicine applications, greater understanding of the structure-function-property characteristics of mesenchymal cell suspensions is required.

In this thesis, the results of a detailed experimental study into the flow behaviour of concentrated suspensions of living mesenchymal cells over a wide range of cell concentrations and in the presence of two macromolecules (hyaluronic acid and polyethylene glycol) often used in cellular therapy applications are presented. The change in the shear viscosity as a function of shear stress and shear rate for cell volume fractions varying from 20 to 60% are firstly presented, showing that these suspensions exhibit highly complex but reproducible rheological footprints, including yield stress, shear thinning and shear-induced fracture behaviours.

The rheological properties of the suspension with the addition of hyaluronic acid (HA), a biomolecule with adhesion sequences for receptors on these types of cells, was then investigated. With the addition of HA, the rheology of these cell suspensions is significantly modified at all volume fractions. Using FACS and confocal imaging, we show that the observed effect of HA addition is due to it significantly modulating the formation of cellular aggregates in these suspensions, and thus the resultant volume spanning network. This understanding permits the rheology of concentrated mesenchymal cell suspensions to be tailored to suit particular processing scenarios.

The third part of this project focused on the addition of polyethylene glycol, a molecule which is not naturally present in tissues but commonly utilised in hydrogels as injectable delivery vehicles for cells to sites of tissue damage. Using three different kinds of PEG, the influence of the charge of the molecules is investigated. The results show the charge is also a crucial parameter to tailor the flow behaviour of cell suspension when biomacromolecules are added, influencing the formation and the compactness of the cellular aggregates.

Considering the aggregates as fractal structures, and by taking into account the changes in volume fractions with shear, a master curve for the range of conditions investigated was successfully achieved through the use of an analytical model. Critically, this model also permitted the estimation of the average adhesion force between cells, across a population of millions of cells. The outcomes of this study not only provide new insight into the complexity of the flow behaviours

of concentrated, dynamically adhesive mesenchymal cell suspensions, and their sensitivity to associative biomolecule and synthetic molecule addition, but also a novel, rapid method by which to estimate adhesion forces between cells.

Résumé

L'attention de la communauté scientifique, ainsi que le développement, pour les bioprocédés dédiés à la culture et à l'expansion de cellules souches mésenchymateuses (MSCs) pour la thérapie cellulaire et la médecine régénérative a considérablement grandi pendant ces dernières décennies. Une plus ample compréhension du lien entre la structure, la fonction et les propriétés des suspensions de cellules mésenchymateuses est devenue de première importance.

Dans cette thèse, nous présentons tout d'abord les résultats d'une étude expérimentale portant sur l'écoulement de suspensions concentrées de cellules vivantes d'origine mésenchymateuse pour une grande gamme de concentration cellulaire. Nous caractérisons l'évolution de la viscosité relative en fonction de la contrainte de cisaillement appliquée pour des fractions volumiques cellulaires allant de 20 à 60%. Ces matériaux ont des empreintes rhéologiques compliquées mais très reproductibles, incluant des comportements de fluide à seuil, rhéofluidifiants ainsi que des fractures liées à la contrainte de cisaillement.

Les propriétés rhéologiques de la suspension sont ensuite étudiées avec l'addition d'acide hyaluronique (HA), une biomolécule avec des séquences d'adhésion pour des récepteurs à la surface des cellules étudiées. Nous montrons que l'addition d'acide hyaluronique modifie substantiellement le comportement de la suspension et nous permet de contrôler les propriétés d'écoulement de la suspension à toutes les fractions volumiques. Cytométrie de flux et imagerie confocal à l'appui, nous montrons que l'effet observé est dû à un important changement dans la formation d'agrégats cellulaires dans la suspension, et donc dans l'envergure du réseau correspondant.

La troisième partie de cette thèse porte sur l'ajout de polyéthylène glycol, une molécule qui n'est pas naturellement présente dans l'organisme mais fréquemment utilisée dans la formulation d'hydrogel. En utilisant trois types de PEG, l'influence de la charge des molécules est étudiée. Les résultats montrent que la charge est un paramètre important dans le contrôle des propriétés d'écoulement de suspensions cellulaires, car déterminant dans la formation et la compacité des agrégats.

En considérant les agrégats comme des objets fractals, nous montrons qu'en prenant en compte les modifications de fractions volumiques avec le cisaillement, nous pouvons obtenir une courbe maitresse pour l'ensemble des conditions testées, et en extraire la force d'adhésion moyenne entre les cellules, au travers une population de plusieurs millions de cellules. Cette étude livre de nouveaux

aspects sur la complexité des propriétés en écoulement de suspensions de cellules méchymateuses, adhérentes et concentrées, sur leur sensibilité à l'ajout de molécules, qu'elles soient naturellement présentes dans les tissues ou non, ainsi qu'une nouvelle méthode pour mesurer la force d'adhésion entre les cellules.

Acknowledgement

As this work was carried out in two different laboratories, in two different countries, on two different continents, I have quite a number of people to thank. I apologize to anyone I may have forgotten. I would like to express my thanks to Prof. Peter Fisher, from ETH Zürich in Switzerland, and to Prof. Gareth McKinley, from the MIT in the United States of America for their thorough reviews of this manuscript and for the numerous questions that were asked the day of the defence. I believe their comments, questions and suggestions have strongly enhanced the quality of this work.

I would also like to thank Dr. Francois Molino and especially Prof. Claude Verdier for accepting being my examiners.

I would like to give my special thanks to my two supervisors, Prof. Justin Cooper-White and Dr. Denis Roux. Their support, guidance, help and patience during the last three years were very appreciated, and the invaluable discussions throughout the PhD are of course greatly acknowledged. They have both restlessly helped me a lot with different aspects of the project and I can only hope to become such a scientist one day. I would like to extend my gratitude to Prof. Peter Thorn from the University of Queensland, for allowing me to use his two-photon microscope and to access his lab whenever I needed it. This work had been significantly enhanced thanks to the two-photon microscope images, and this could have never been done without his help. I would also like to thank the different people in the TE&M and in the Laboratoire Rhéologie et Procédés. I am not going to name every single one of them, even though they would deserve it, but I do thank all of them for their friendship, their support and their help, for all the coffee breaks and the general good mood that made me happy to go the either lab every single day. More especially on the Aussie side, I would like to thank Clementine a.k.a. “ Mémé Pradou ” Pradal for the French talks, the outdoors rock-climbing and the soft potato chips she was giving me every single time she was having some for lunch (Merci Coupine!), Jess a.k.a.“ Britiiiiiiish ” Frith for her Britishness (that says it all) and her incredible patience when she was trying to teach me how to do FACS and all sort of biological things (you are kind of Boss for a British, maybe you have the potential to become a rheologist one day), Jane Fitzpatrick for all the talks while I was sitting on the ground at the entrance of her office, for the patience and the answers to my daily questions and for teaching me cell culture (and that’s quite an achievement, you should put it in your resume), Lien a.k.a. .“ Pinky ” Wong for her all her funny personal stories, Tania Banks for her enthusiasm and for showing me that it did not

matter how busy I was, she was always ten times busier (I still don't know how you manage everything at the same time!), Alejandro a.k.a. " Machete " Hidalgo Gonzalez for his friendship, the ciggy breaks, the mornings climbs at the gym and the blockish talks (ojo ojo!), Paul a.k.a " Lucky " Luckman for him being him (a bawssss), Anne Kozak (that's a cool new name) for reminding me that even if a PhD is a long process, it still ends one day, Donna a.k.a. " Booga Doc " Menzies for the fun talks and the help with the different PEGs and of course, all the others, who were there at some point or another, and helped to make the time in the AIBN incredible. On the French side, I would like to thank especially Etienne a.k.a. " Chatouille " Ghiringhelli for his friendship and all the daily fun we had through all these years, it was quite a relief to have such a friend in the lab in France, Anica a.k.a. " Anitsssa " Lancuski and Carhel Dassi for their patience while sharing an office with Chatouille and I, Abdul Abusaksaka, Nicolas Mougin, Yannick Molméret, Céline a.k.a. " Chécoleloulouttе " Colet and all the late comers: Yao, Chong, Nabil and Fiacre for making me laugh each and every day.

I would also like to thank my friends, both from Australia and France, for their support, but also for allowing me to have a life outside lab work. In no particular order, Renaud, Lapinou, Isa, Elsa, Tomitomette, Pierrot, Antho, Mymy, Hervé, Gab, Mike, Lucie, Jaz, Mo, Preece, Chuck, Chase, James, Jess Red, Jess Black, Jacqui, Hannah, Damian, Rima, Kim-Anh, Walshy, WussyWuss, Maddie, Panos, Benoît, Laure, Carl, Jason, Erika, Claire, Mareike, and Alex (this list is not exhausitive), thank you all for all the time together wether it was as friends or housemates. You have all contributed to this experience. To finish with the friends, a very special thanks to Daniel a.k.a. " Aspo " Aspinall (and his family) for everything. I can't even begin to enumerate all the reasons why I am thankful, but I deeply am.

Last but not the least, I would like to thank my entire family, for their love and their support as well as believing in me.

Contents

List of Figures

General Introduction

A suspension consists of discrete solid particles randomly distributed in a fluid medium. The rheology of suspensions in a Newtonian fluid has been widely studied, as many materials in use today are disperse systems where particles are dispersed in another phase. Therefore any new insights in the rheology of these systems can be of great practical importance.

The flow properties of suspensions are closely related to the nature of the particles within them. Various microscopic parameters intrinsic to the very nature of the particles being investigated, such as shape, size, affinity with other particles, elastic modulus, deformability and buoyancy, are highly correlated to tailoring the resultant macroscopic parameters relevant to continuous processing methodologies. In the end, the ability to predict and explain the differences in non-Newtonian behaviours of these complex systems lies in the ability to understand the evolution of the microscopic organization of the particles within the suspending fluid.

In this piece of research, we investigate the rheological behavior of suspensions of live cells of mesenchymal origin (mouse NIH-3T3) in their culture medium without serum, with and without the addition of various biomacromolecules. The two main molecules added are hyaluronic acid (HA) and poly(ethylene glycol) (PEG). Hyaluronic acid is a macromolecule widely present in several tissues, whereas polyethylene glycol is a synthetic molecule. According to the volume fraction of cells in the suspension, the type of molecules added, their concentrations and the shear applied on the material, several complex behaviour can be observed, as different microscopic re-arrangements occur.

The use of living cells induces biological variability, an input that is inherent to cellular systems, as well as the naturally complex aggregation mechanisms involved in cell-cell adhesion mechanisms. The macroscale properties of such materials remain largely unexplored. The lack of published work in this area is highly linked to the difficulties inherent to the use of living cells in traditional rheological measurements, which include the variability of the samples or the time and cost of culturing enough cells for a single test with conventional rheometry setups.

The rheology of NIH-3T3 cells suspensions is investigated thanks to conventional rotational rheometry setups. The microstructure created by the cells adhering to each other is studied using conventional bright field (2D) and two-photon (3D) microscopy. Conventional fluorescence techniques such as flow cy-

tometry are used to study the presence of different receptors of interest on the surface of the cells. This allows us to first, draw some conclusions on the impact of volume fraction and of the addition of HA and PEG biomacromolecules on the mechanical properties of the suspensions, and second to propose links between the mechanical properties and the microstructure.

This manuscript is divided and organised in several chapters as follows.

In the first chapter, we give an overview of the theoretical background of rheology and describe the different parameters of interest. This is followed by a section focussed on rheometry, describing the different existing tests as well as the different kinds of rheometers.

The second chapter reviews the main results and theory found in the literature about suspension mechanical properties, going from hard spheres suspensions to deformable spheres suspensions. The main kind of interactions in suspensions (and especially in colloidal systems) are reviewed, as well as the main known results on aggregated suspensions.

In the third and last chapter of the theoretical background, we focussed on the main notions about cell-cell interactions, as well as cell-matrix interactions. This is required as it allows us to understand more in depth the different biological mechanisms at play, and thus to link it with the mechanical properties of the suspensions studied in this project.

The fourth chapter is a materials and methods chapter. The different materials as well as the different protocols followed during this project are therefore detailed here. In this chapter, the main causes for errors are investigated, especially the ones concerning the rheology protocols (slippage, etc.).

The fifth chapter characterizes the rheology of the cells (NIH-3T3) in the culture medium without serum. Several volume fractions are investigated over a wide range of shear stresses. The results of the analysis of the conventional bright field (2D) and two-photon (3D) microscopy images are presented in term of fractal dimensions. An analytical model is then used to have the data collapse onto a mastercurve in a figure of the relative viscosity as a function of the effective volume fraction. From this collapse, the average adhesion strength between two cells is extracted and compare with reported literature values, with very good agreement.

The sixth chapter focusses on the addition of our first molecule: hyaluronic acid. The same protocols, as used in the previous chapter are used to investigate the influence of hyaluronic acid, at different concentrations, and of different molecular weight, on the rheology of concentrated cell suspensions. The presence of both the specific surface receptors and the hyaluronic acid molecules are confirmed experimentally, using flow cytometry and confocal imaging.

At last, the seventh and last chapter of this thesis aims to characterize the influence of the second kind of molecule added to the system: poly(ethylene glycol). Once again, the same protocols are used for three different kinds of poly(ethylene glycol) (PEG) molecules (PEG, PEG-NH_2, PEG-COOH). Polyethy-

lene glycol does not have any known specific receptors on the surface of cells, and therefore does not bind to them in a specific, defined manner. The three different kinds of eight armed PEG molecules used allows us to study the influence of the charge of the molecules on the flow behaviour of the suspension.

Introduction Générale

Le terme suspension désigne un matériau biphasique, composé d'une phase liquide dite continue dans laquelle une phase solide est dispersée. La rhéologie d'une suspension dans un fluide Newtonien a été amplement étudiée, puisque beaucoup de matériaux utilisés à l'heure actuelle peuvent être classée dans cette catégorie. De ce fait chaque avancée, théorique ou pratique, peut être d'une importance cruciale.

Les propriétés en écoulement des suspensions sont étroitement liées à la nature des particules du milieu dispersé. Plusieurs paramètres microscopiques intrinsèques à la nature des particules tels que leur forme, leur taille, l'affinité des particules entre elles, leur module élastique, leur déformabilité et leur densité sont intimement liés aux paramètres macroscopiques essentiels au développement de techniques ou méthodes pour utiliser les suspensions. La capacité à prédire et à comprendre les différences entre les comportements non-Newtoniens de ces matériaux complexes réside dans la faculté à comprendre l'évolution de l'organisation microscopique des particules au sein de la phase continue.

Dans ce travail de recherche nous nous intéressons à la rhéologie des suspensions de cellules mésenchymateuses vivantes (NIH-3T3 provenant de souris) dans leur média de culture dénué de sérum, avec ou sans l'ajout de plusieurs molécules. Les effets de chacune des molécules ajoutées (acide hyaluronique (HA) et polyéthylène glycol (PEG)) sont étudiés. L'acide hyaluronique est une macromolécule présente naturellement dans les divers tissues du corps, tandis que le polyéthylène glycol est une molécule purement synthétique. Plusieurs comportements complexes peuvent être observés selon la fraction volumique de cellules, le type de molécule ajoutée, sa concentration et la contrainte mécanique appliquée, en fonction des différents réarrangements possibles au niveau microscopique.

L'utilisation de cellules vivantes introduit une variabilité biologique inhérente aux systèmes cellulaires et aux mécanismes complexes d'agrégation entrant en jeu dans les contacts extra-cellulaires. Les propriétés macroscopiques de ces matériaux ont été très peu étudiées. Le manque de travaux publiés à ce sujet est fortement lié aux difficultés venant de l'utilisation de cellules vivantes avec les techniques de rheométrie conventionnelles, que ce soit dû au coût ou au temps nécessaires pour obtenir suffisamment de cellules pour un test ou à la variabilité des échantillons en eux-mêmes.

Les propriétés rhéologiques de NIH-3T3 en suspension sont étudiées au moyen d'un rhéomètre rotatif. La structure microscopique est étudiée grâce à

un microscope bi-photonique. Des techniques de fluorescence classiques, comme la cytométrie en flux sont utilisées pour s'assurer de la présence de récepteurs spécifiques à la surface des cellules. Ceci nous permet tout d'abord de comprendre plus en détail l'impact de la fraction volumique ainsi que de l'ajout de molécules d'HA et de PEG sur les propriétés mécaniques de la suspension, et ensuite de proposer des liens entre ces mêmes propriétés mécaniques et la microstructure de la suspension.

Chapter 1

Rheometry and Rheometers

Contents

Résumé du Chapitre

Dans ce premier chapitre, nous introduisons les notions de bases nécessaires à la compréhension des propriétés non-Newtoniennes des matériaux.

Nous présentons dans un premier temps les différents concepts utilisés en rhéologie, comme la contrainte de cisaillement, le tenseur de déformation ou le taux de déformation.

Les principaux éléments servant à caractériser le comportement complexe de tels matériaux sont ensuite abordés, ainsi que les principaux types de tests utilisés pour les déterminer.

La troisième partie se concentre sur les différents types de rhéomètres rotatifs existants, tout en définissant leurs avantages et leurs inconvénients.

La quatrième et dernière partie de ce chapitre se focalise d'avantage sur les différentes géométries principalement utilisées sur ce genre de rhéomètres, pour passer en revue les hypothèses, les équations et les avantages relatifs à chacune d'entre elles.

1.1 Introduction

"Πὰνταα ῥεῖ". Read 'Panta rhei', meaning 'Everything flows'. This famous aphorism of Simplicus to characterize Heraclitus's thought inspired Eugene C. Bingham and Markus Reiner to win the term 'Rheology'. The idea behind it is that everything has a time scale, and if one is prepared to wait long enough, then everything will flow. The term 'Rheology' is now used to describe the study of the flow of matter, whether it is liquid, 'soft' solid or solid. This area of science, at the border of physics, mathematics, chemistry and biology, find applications in pretty much everything that surrounds us. Its industrial impact goes from petroleum process to pharmaceutical applications, from paints to food, from muds to blood and so on. For a long time, only two constitutive laws existed to describe the deformation of materials, according to their state. The material could either be an elastic solid, and therefore follow Hooke's law [1], or a liquid, and follow Newton's law [2]. However, as it is now known, these two laws are two limiting cases. In between are pretty much all the materials around us.

1.2 Basic definitions

When one talks about elasticity, Hooke's law is the first thing that comes to mind. Robert Hooke experimentally studied the deformation of springs and long wire in tension. He showed that when he doubled the weight attached to the springs, the extension doubled. He thus proposed that the force was proportional to the change in length. However, if he changed of wire length or diameter, he found a new constant. Therefore his constant was not only a material property, it was also related to the geometry of the sample. To find the true material constant, the elastic modulus, Hooke needed to develop concepts that are still used nowadays, such as stress (force per unit area) and strain. Stress and strain are essential in rheology, and are defined in more details below, along with the basics of this science.

1.2.1 Stress tensor

1.2.1.1 Definition

[1] $\sigma = E\gamma$ where σ is the stress, E is the Young's modulus and γ is the strain.
[2] $\sigma = \eta\dot{\gamma}$ where σ is the stress, η is the viscosity and $\dot{\gamma}$ is the rate of strain.

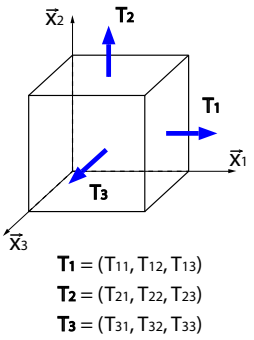

Figure 1.1: Infinitesimal unit cube in the state-of-stress in terms of forces.

In continuum mechanics, the stress is a measure of the internal forces acting within a deformable body. As drawn in Figure 1.1, a material can be virtually cut into small infinitesimal cubes. We note $(\overrightarrow{dF_j})_{j=1,2,3}$ the forces exerted by the material exterior to the cube on its face perpendicular to the j direction and $(dF_{ij})_{i,j=1,2,3}$ the components on the i directions. The stresses acting on the different planes of the cubes are all related, and can be determined from the stress tensor, noted $\overrightarrow{T}(M, \overrightarrow{n})$ at the center M of a surface ds and defined as:

$$\overrightarrow{dF} = \overrightarrow{T}(M, \overrightarrow{n})ds \tag{1.1}$$

Where $\overrightarrow{n}$ is the normal vector to the surface ds.

The state-of-stress tensor $\mathbf{T}(M)$ is then defined by:

$$\overrightarrow{T}(M, \overrightarrow{n}) = \mathbf{T}(M).\overrightarrow{n} \tag{1.2}$$

The ij components of the state-of-stress tensor are given by:

$$T_{ij} = (\frac{dF_{ij}}{ds})_{i,j=1,2,3} \tag{1.3}$$

1.2.1.2 Symmetry

The stress tensor is symmetric, meaning the rows and the columns of the matrix for the components of $\mathbf{T}$ can be interchanged without changing $\mathbf{T}$. An easy way to show the symmetry of the stress tensor is to consider a small tetrahedron, like the one in Figure 1.2. The component T_{23} produces a moment about the x_1 axis. This moment must be balanced by the one produced by T_{32} or the angular momentum would not be conserved. This implies $T_{23} = T_{32}$. By using a similar argument on the other different shear components, we got $T_{12} = T_{21}$ and $T_{13} = T_{31}$. Thus the stress tensor is symmetric and we can write:

$$\mathbf{T} = \mathbf{T}^T \tag{1.4}$$

where $\mathbf{T}^T$ is the transpose of $\mathbf{T}$.

1.2.1.3 Pressure

One particular simple stress tensor is the one of uniform pressure. When a fluid is at rest, it can support only a uniform normal stress. Thus, in a fluid under hydrostatic pressure, the state-of-stress tensor simplifies in an isotropic tensor (equation 1.5) in which **I** is the unit tensor.

$$\mathbf{T} = -p\mathbf{I} \tag{1.5}$$

In an incompressible fluid, only the pressure gradients affect the flow motion. Thus, the state-of-stress tensor is usually decomposed as:

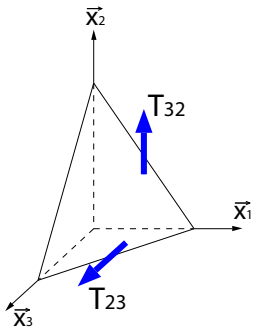

Figure 1.2: To keep the angular momentum balance, the two shear stress components acting on the tetrahedron must be equal.

$$\mathbf{T} = \boldsymbol{\sigma} - p\mathbf{I} \tag{1.6}$$

where $\boldsymbol{\sigma}$ is called the extra or viscous stress tensor, and accounts for the forces affecting the motion of the fluid. It often happens that **T** is referred to as the total stress tensor and $\boldsymbol{\sigma}$ as just the stress tensor.

1.2.2 Deformation tensors

After defining the stress tensor used to determine the state of stress in a material, we define the deformation gradient. To do so, we consider a piece of material, as shown in Figure 1.3. A is a point embedded in the body and B a neighboring point separated by a small distance $d\overrightarrow{x}(t_0)$ at a time t_0. The area vector $d\overrightarrow{s}(t_0)$ represents a small area around B. This is a past time or initial configuration. From this state, we apply a deformation on the piece of material. During this deformation, the points A and B move with the material. The distance between them will stretch and rotate. This displacement will be indicated by the magnitude and the direction of $d\overrightarrow{x}(t)$. We can link $d\overrightarrow{x}(t)$ to $d\overrightarrow{x}(t_0)$ thanks to the deformation gradient tensor **F**, defined as:

$$d\overrightarrow{x}(t) = \mathbf{F} \cdot d\overrightarrow{x}(t_0) \tag{1.7}$$

The deformation gradient describes the state of deformation and rotation in our piece of material. It can be noted that through this definition the present position $\overrightarrow{x}$ is a function of the past position and of the time.

1.2.3 Velocity gradient

It is useful to define a way to determine the velocity gradient in any direction at a point in the fluid. We consider two points A and B embedded in a flowing

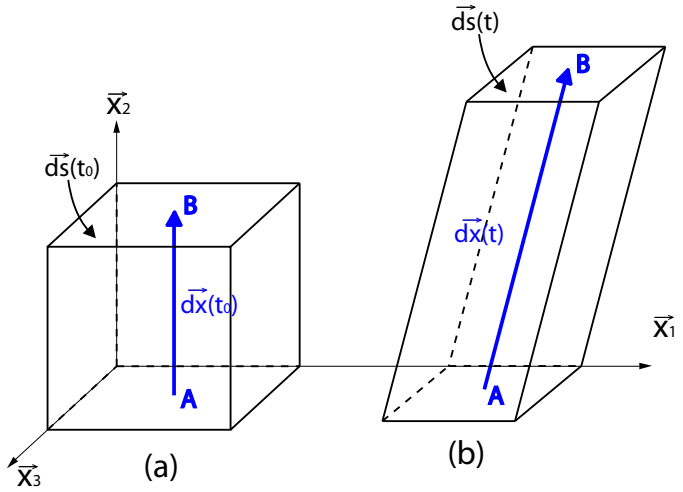

Figure 1.3: Deformation of a piece of material showing the motion of two neighboring points A and B, (a) is at rest, (b) after deformation.

fluid, separated by a small distance $d\overrightarrow{x}(t_0)$ as shown in Figure 1.4. In general, the velocity in a fluid is a function of both position and time. Thus, the velocity at point A is $\overrightarrow{V}$ and $\overrightarrow{V} + d\overrightarrow{V}$ at the point B. The relative rate of separation $d\overrightarrow{V}$ of the two points can be estimated at any point in the fluid by taking the gradient of the velocity function:

$$d\overrightarrow{V} = \frac{\delta \overrightarrow{V}}{\delta \overrightarrow{x}} \cdot d\overrightarrow{x} = \mathbf{L} \cdot d\overrightarrow{x} \tag{1.8}$$

where $\mathbf{L}$ is the velocity gradient tensor. The velocity gradient tensor and the deformation gradient tensor described earlier are clearly related. By taking the time derivative of equation 1.7, we can write:

$$\frac{\delta(d\overrightarrow{x}(t))}{\delta t} = \frac{\delta \mathbf{F}}{\delta t} \cdot \overrightarrow{dx(t_0)} + \mathbf{F} \cdot \frac{\delta(\overrightarrow{dx(t_0)})}{\delta t} \tag{1.9}$$

$d\overrightarrow{x}(t_0)$ is fixed at a certain time t_0, so $\delta(d\overrightarrow{x}(t_0))/\delta t = 0$. The previous equation then becomes:

$$\frac{\delta(d\overrightarrow{x}(t))}{\delta t} = d\overrightarrow{V} = \dot{\mathbf{F}} \cdot \overrightarrow{dx(t_0)} \tag{1.10}$$

Using this with the equations 1.8 and 1.7 gives:

$$\dot{\mathbf{F}} \cdot \overrightarrow{dx(t_0)} = \mathbf{L} \cdot d\overrightarrow{x} \tag{1.11}$$

In the limit as the past displacement is brought to the present, we can write:

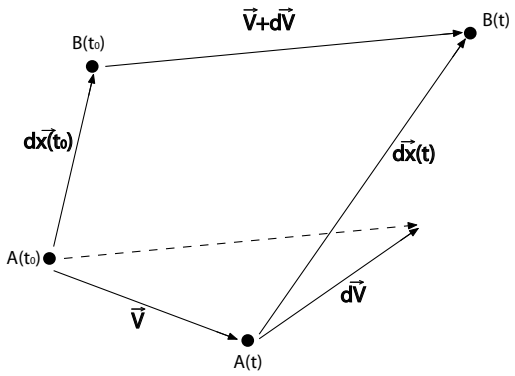

Figure 1.4: Relative velocity between two points moving in a fluid.

$$\begin{aligned} \lim_{t_0 \to t} \mathbf{F} &= \mathbf{I} \\ \lim_{t_0 \to t} \dot{\mathbf{F}} &= \mathbf{L} \end{aligned} \tag{1.12}$$

1.2.4 Rate of deformation

1.2.4.1 Rate-of-deformation and vorticity tensors

We can extract rotation from the velocity gradient by defining $\mathbf{F}$ in terms of stretch $\mathbf{V}$ and rotation $\mathbf{R}$ tensors:

$$\mathbf{F} = \mathbf{V} \cdot \mathbf{R} \tag{1.13}$$

Taking the time derivative,

$$\dot{\mathbf{F}} = \dot{\mathbf{V}} \cdot \mathbf{R} + \mathbf{V} \cdot \dot{\mathbf{R}} \tag{1.14}$$

If we let the past displacement coming up to the present, there should be no displacements, therefore

$$\lim_{t_0 \to t} V(t_0) = \lim_{t_0 \to t} R(t_0) = \mathbf{I} \tag{1.15}$$

Using the equation 1.12, we obtain:

$$\lim_{t_0 \to t} \dot{F} = \mathbf{L} = \dot{\mathbf{V}} + \dot{\mathbf{R}} \tag{1.16}$$

which leads to

$$\mathbf{L}^T = (\dot{\mathbf{V}} + \dot{\mathbf{R}})^T \tag{1.17}$$

The time derivative of the stretching tensor is usually called the rate-of-deformation tensor $2\mathbf{D}$ and is symmetric. $\dot{\mathbf{R}}$ is antisymmetric and is called the vorticity tensor $\mathbf{W}$.

$$\begin{aligned} 2\dot{\mathbf{V}} &= 2\mathbf{D} = \mathbf{L} + \mathbf{L}^T \\ 2\dot{\mathbf{R}} &= 2\mathbf{W} = \mathbf{L} - \mathbf{L}^T \end{aligned} \tag{1.18}$$

1.2.4.2 Finger and Cauchy-Green tensors

There are two other tensors which can be useful to determine the state of deformation of a material: the Finger and the Cauchy-Green tensors. The Finger tensor, noted $\mathbf{B}$, describes the area change around a point on a plane. Thus, $\mathbf{B}$ can give the deformation at any point in terms of area change by operating on the normal to the area defined. The Cauchy-Green tensor, noted $\mathbf{C}$, gives the deformation in terms of length change. They are defined as:

$$\begin{aligned} \mathbf{B} &= \mathbf{F} \cdot \mathbf{F}^T \\ \mathbf{C} &= \mathbf{F}^T \cdot \mathbf{F} \end{aligned} \tag{1.19}$$

1.2.5 Shearing flows

Several flow configurations exist to characterize the flow properties of a material. Shearing flow is one of them, and certainly one of the simplest. One of the main advantages of such flow is that several components of the stress tensor and of the rate-of-deformation tensor become null.

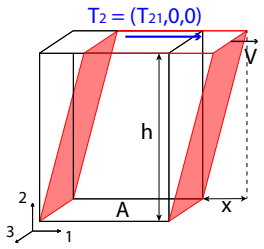

Figure 1.5: Schematic of a shearing flow between two parallel plates.

Using various level of approximation, several flow geometries can be used in order to produce an homogeneous state of stress and strain within a fluid. The easiest way to understand and to illustrate a shearing flow is represented in Figure 1.5. Here, we consider a piece of material confined between two parallel plates. The bottom plate is fixed, whereas the top plate is moving at a constant speed V. We are assuming a laminar flow and a no-slip condition on the two plates, which means:

$$\begin{aligned} v_1(x_2 = 0) &= 0 \\ v_1(x_2 = h) &= V \end{aligned} \tag{1.20}$$

Under such conditions, the deformation of the bulk material can be considered as the sliding of thin fluid layers one over the others. Then, considering a

two dimensional flow, the only non null component of the velocity at the distance x_2 from the fixed bottom plate is v_1, with its profile given by:

$$v_1(x_2) = \frac{V}{h} x_2 \tag{1.21}$$

From that, we can easily deduce that the rate-of-deformation tensor, as defined in 1.2.4.1 is given by:

$$D_{12} = D_{21} = \frac{V}{2h} = \frac{\dot{\gamma}}{2} \tag{1.22}$$

Where $\dot{\gamma}$ is the shear rate. Such flow conditions also give rise to simple expressions of the stress tensor. The relative movement of each layer of material induces a friction force corresponding to the force which is necessary to move the upper plate. In this type of flow, the stress tensor is often referred to as the shear stress, and is given by:

$$\sigma_{12} = \sigma_{21} = \frac{F}{A} \tag{1.23}$$

Where F is the necessary force to move the plate, and A the surface of the plate. The shear viscosity of a material can then be defined as the ratio between the shear stress and the shear rate.

$$\eta = \frac{\sigma_{12}}{\dot{\gamma}} \tag{1.24}$$

In the simplest case, the fluid is Newtonian and the shear viscosity is a constant so the shear stress is directly proportional to the shear rate. Furthermore, the shear stress is the only non null component of the stress tensor so that the knowledge of the shear stress is enough to fully characterize the material under shear flow conditions. In complex fluids however, the relation between the shear stress and the shear rate is not that simple. Indeed, the shear stress experienced by the material can be a function of the applied stress and of the shearing time. The shearing process can also induce normal forces so that the diagonal components of the stress tensor are not equal to zero. In these cases, the knowledge of the shear viscosity is not enough to fully characterize the material flow properties. Therefore, the shear ratio between the shear stress and the shear rate is then referred as the apparent shear viscosity and is defined as:

$$\eta(\dot{\gamma}, t) = \frac{\sigma_{12}(\dot{\gamma}, t)}{\dot{\gamma}} \tag{1.25}$$

1.3 Complex behaviors

When the ratio between the shear stress and the shear rate is not constant, the fluid is referred to as non-Newtonian. The fluid can then have both a viscous

part and an elastic part. It is therefore also called a viscoelastic fluid. The link between the shear stress and the shear rate can sometimes be complex to understand because of its dependence to a wide range of parameters such as shear applied, shear history, ageing... A range of test has been developed through the years to help and characterize this kind of materials [1, 3, 4, 5].

1.3.1 Normal stress in shearing flow

When a viscoelastic material is sheared between two parallel surfaces, in addition to the viscous shear stress τ_{12}, there are normal stress differences N_1 and N_2 defined as follow:

$$\begin{aligned} N_1 &= T_{11} - T_{22} \\ N_2 &= T_{22} - T_{33} \end{aligned} \tag{1.26}$$

In this case, "1" represents the flow direction, "2" the perpendicular direction to the surfaces between which the fluid is sheared and "3" is the neutral direction. The apparition of normal forces will tend to push apart, or to pull together closer, the two parallel surfaces, depending on its sign.

1.3.2 Viscoelasticity

1.3.2.1 Integral relation between the shear stress and the shear rate

In the early attempts to characterize viscoelastic solids, Boltzmann[2] suggested that small changes in stress are due to small changes in strain:

$$d\sigma = Gd\gamma \tag{1.27}$$

This equation can be rewritten as:

$$d\sigma = G\frac{d\gamma}{dt}dt = G\dot{\gamma}dt \tag{1.28}$$

Integrating this equation over all past time, as suggested by Maxwell [1, 5]:

$$\sigma(t) = \int_{-\infty}^{t} G(t-t')\dot{\gamma}(t')dt' \tag{1.29}$$

Where t' is the past time variable running from the infinite past to the present time t. The elapsed time $t - t'$ is often denoted s. Thus, equation 1.29 becomes:

$$\sigma(t) = \int_{0}^{\infty} G(s)\dot{\gamma}(t-s)ds \tag{1.30}$$

It is then possible to say the stress is an integral, over all past time, of the relaxation modulus times the ratio of strain. Since the deformation does not have to be constant through the time, $\dot{\gamma}$ is a function of time. This form is frequently used because $G(t)$ can be measured directly. A way to express $G(t)$ is to write it as a series of relaxation time λ_k multiplied by a weighting constant G_k:

$$G(t) = \sum_{k=1}^{N} G_k e^{-\frac{t}{\lambda_k}} \tag{1.31}$$

Which in equation 1.29 gives the general linear viscoelastic model:

$$\sigma(t) = \int_{-\infty}^{t} \sum_{k=1}^{N} G_k e^{-\frac{t-t'}{\lambda_k}} \dot{\gamma}(t') dt' \tag{1.32}$$

It is also possible to introduce a memory function M as the time derivative of $G(t)$ and express the previous equations with it. Note that equation 1.29 can be easily written in three dimensions by using the extra stress tensor σ for the shear stress and the rate of deformation $2\mathbf{D}$ for $\dot{\gamma}$:

$$\boldsymbol{\sigma} = \int_{-\infty}^{t} G(t-t') 2\mathbf{D}(t') dt' \tag{1.33}$$

1.3.2.2 Relaxation spectrum

In the past, another approach which has been widely used is the relaxation spectrum $H(\lambda)$. This approach has mainly been used because it provides a continuous function of relaxation time λ rather than a discrete set, like introduced in the previous part. The relation used to link the relaxation modulus and the spectra is:

$$G(s) = \int_{0}^{\infty} \frac{H(\lambda)}{\lambda} e^{-s/\lambda} d\lambda \tag{1.34}$$

Several forms for $H(\lambda)$ exist, and a consequent part of the literature is in terms of it [3].

1.3.2.3 Viscoelastic models

Viscoelastic models can be created in order to describe viscoelastic behavior of materials. A way to do so is to use mechanical components such as springs or dashpots to build the models. Such approach is based on the mechanical components defined in Figure 1.6.

The models described in Figure 1.7 are basic viscoelastic models. The first one is called the Maxwell model. For slow motions, the dashpot or Newtonian behavior dominates, whereas for rapidly changing stresses, the derivative term

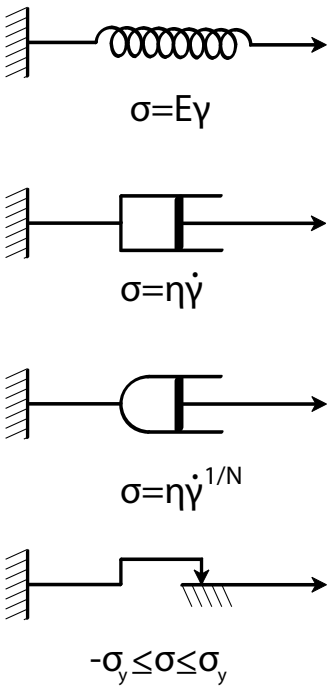

Figure 1.6: Schematic of the basis mechanical components used to model viscoelastic behaviors.

dominates, thus at short times, the model approaches elastic behavior. We can define from this model the Maxwell 's relaxation time λ:

$$\lambda = \frac{\eta}{E} \tag{1.35}$$

Where E is the elastic modulus.

As written in equation 1.31, some materials do not have one but several relaxation times. A way to model this is to use the generalized Maxwell model, also known as the Maxwell-Weichert model. This model can have several representations, like the one in Figure 1.8-a. It is the most general form of the linear model for viscoelasticity, and it takes into account that the shorter molecular segments contribute less than longer ones, creating a varying time distribution. Several other models exist to describe viscoelasticity (such as the ones shown in Figure 1.8-a,b), plasticity (as Figure 1.8-c) and elastoviscoplasticity (Figure 1.8-d for example), mainly build from the components defined before.

1.3.3 Small strain material functions

Several types of small strain experiments are used in rheology. The three more common techniques are stress relaxation, creep and sinusoidal oscillations. These three different experimental methods give different quantities to characterize a material. It is often difficult to transform results from one type of experiment

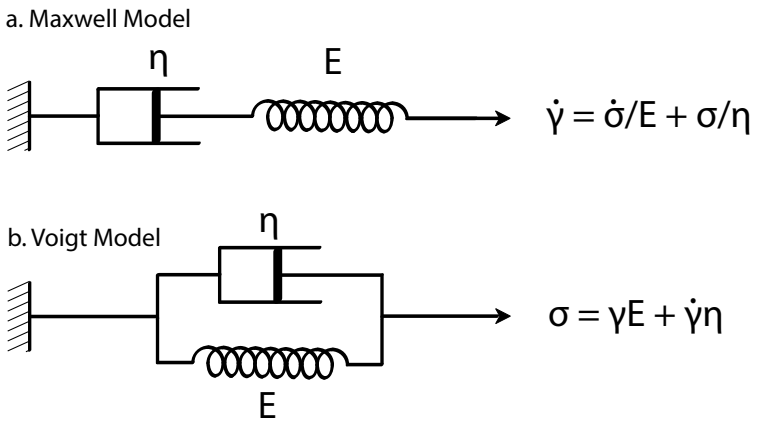

Figure 1.7: Schematic of the Maxwell and the Voigt models

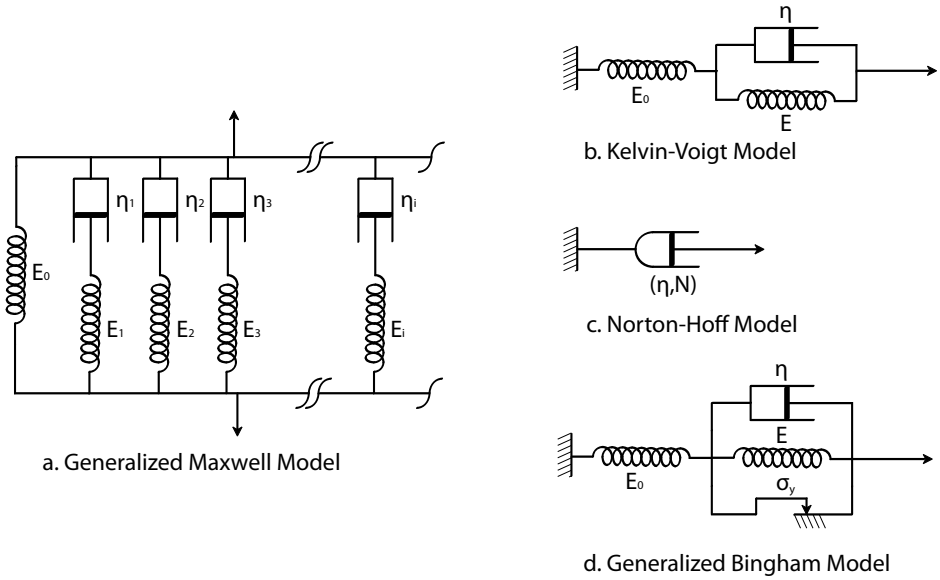

Figure 1.8: Schematic of other models

to the other. The passage from the creep compliance to the stress relaxation modulus for example is generally difficult.

1.3.3.1 Stress relaxation

The relaxation modulus is defined as the stress relaxation after a step strainγ_0. Data from stress relaxation experiments can directly be linked to the relaxation modulus thanks to:

$$G(t) = \frac{\sigma(t)}{\gamma_0} \tag{1.36}$$

However, it is impossible experimentally to have a instantaneous jump

of strain γ to γ_0. A short rise and stabilization time is required for current instruments. Thus, it is difficult to get data for $t < 0.01s$ by stress relaxation methods. It is also difficult to measure the decay of the stress on a wide range of decades (typically more than three) with one transducer. This means that other methods are needed to measure the short and long time ends of the relaxation spectra.

1.3.3.2 Creep

Creep is the tendency of a material to move or deform under the influence of stresses. Creep experiments are useful for the long time end of the relaxation spectra. In such an experiment, the stress is increased instantly from 0 to σ_0 and the strain is recorded as a function of time, see Figure 1.9.

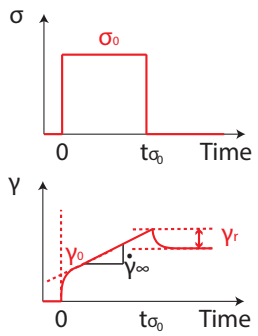

Figure 1.9: Schematic of a creep experiment, where the stress is increased from 0 to σ_0 at $t = 0$, while the strain is recorded as a function of time.

Most of the time, data are expressed in term of creep compliance, defined as:

$$J(t) = \frac{\gamma(t)}{\sigma_0} \tag{1.37}$$

A steady state creep compliance, denoted J_e^0, can be defined as the extrapolation of the limiting slope of the graph of the compliance as a function of the time to $t = 0$. The slope is the inverse of the viscosity at low shear rate η_0. Thus, if we define $\dot{\gamma}_\infty$ as a steady rate of straining reached eventually, in steady creep regime we have

$$J(t) = \frac{\gamma_0}{\sigma_0} + \frac{t\dot{\gamma}_\infty}{\sigma_0} = J_e^0 + \frac{t}{\eta_0} \tag{1.38}$$

If we use the simple Maxwell model (the single relaxation time model defined in Figure 1.7), we obtain

$$J(t) = \frac{1}{E} + \frac{t}{\eta} = \frac{1}{E} + \frac{1}{\lambda E} \tag{1.39}$$

However, for more general models, it is more difficult to calculate the compliance. If we write equation 1.29 for creep experiments, we got

$$\sigma(t) = \int_0^\infty G(t - t')\dot{\gamma}(t')dt' \tag{1.40}$$

Reminding equation 1.29, and considering that at long time the shear rate becomes steady, we can write

$$\sigma(t) = \int_{-\infty}^{t} G(t-t')\dot{\gamma}_\infty dt' \tag{1.41}$$

We change the integration variable t' in $s = t - t'$ and we equal the two previous equations [1, 5]

$$\dot{\gamma}_\infty \int_0^\infty G(s)ds = \int_0^t G(s)\dot{\gamma}(t-s)ds \tag{1.42}$$

We can rewrite it as

$$\dot{\gamma}_\infty \int_t^\infty G(s)ds = \int_0^t G(s)[\dot{\gamma}(t-s) - \dot{\gamma}_\infty]ds \tag{1.43}$$

We then integrate both sides from $t = 0$ to $t = \infty$ and then interchange the order of integration of s and t, which finally give [1]

$$\frac{\gamma_0}{\dot{\gamma}_\infty} = \frac{\int_0^\infty sG(s)ds}{\int_0^\infty G(s)ds} = \lambda_0, \text{the longest relaxation time} \tag{1.44}$$

Or since $\gamma_0 = J_e^0\sigma_0$, we finally have

$$J_e^0 = \frac{\int_0^\infty sG(s)ds}{[\int_0^\infty G(s)ds]^2} \tag{1.45}$$

The relaxation modulus can thus be used to calculate limiting portions of the creep wave.
Another type of experiment often done in conjunction with creep is creep recovery, which is the recoil of strain just after the stress is removed. If the stress imposed during the test was within the linear range of a viscoelastic material, after the stress is removed, the recovered deformation can then defined as a recoverable creep function

$$J_r(t) = \frac{\gamma_r(t)}{\sigma_0} \tag{1.46}$$

where σ_0 is the stress before the recovery start. If the recovery is performed after a steady state creep, so $\dot{\gamma}(t) = \dot{\gamma}_\infty$, the equilibrium creep recovery directly measures J_e^0:

$$\lim_{t\to\infty} J_r(t) = J_e^0 \quad \text{for} \quad \dot{\gamma}(t) = \dot{\gamma}_\infty \tag{1.47}$$

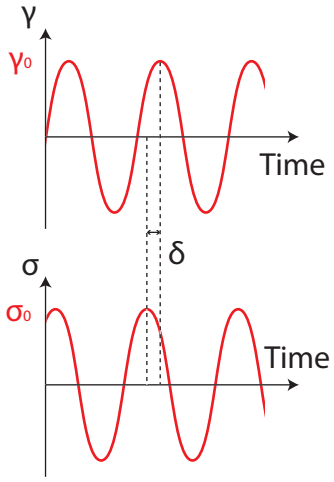

Figure 1.10: Schematic sinusoidally oscillating shear strain, producing a sinusoidal stress phase shifted by an amount of δ.

1.3.3.3 Sinusoidal oscillations

In this kind of small strain experiment, the material is deformed sinusoidally within the linear regime. The measured stress will generally oscillate at the same frequency, but will be shifted by a phase angle δ with respect to the strain wave, as show in Figure 1.10. This can be expressed mathematically as follow [5]:

$$\begin{aligned} \gamma &= \gamma_0 \sin(\omega t) \\ \sigma &= \sigma_0 \sin(\omega t + \delta) \end{aligned} \tag{1.48}$$

The stress can then be decomposed into two signals, one in phase with the strain ($\delta = 0°$) and one out of phase with the strain ($\delta = 90°$). Thus:

$$\begin{aligned} \sigma &= \sigma' + \sigma'' \\ &= \sigma'_0 \sin(\omega t) + \sigma''_0 \sin(\omega t + 90°) \\ &= \sigma'_0 \sin(\omega t) + \sigma''_0 \cos(\omega t) \end{aligned} \tag{1.49}$$

From this, two very useful dynamic moduli can be defined

$$\begin{cases} G' = \frac{\sigma'_0}{\gamma_0} \\ G'' = \frac{\sigma''_0}{\gamma_0} \end{cases} \tag{1.50}$$

G' being the in-phase or elastic or storage modulus, and G'' being the out-of-phase or viscous or loss modulus. According to the previous equations, δ can be written as:

$$\tan \delta = \frac{G''}{G'} = \frac{\sigma''_0}{\sigma'_0} \tag{1.51}$$

These notations come from the complex numbers: the prime represents the real part of a complex number and the double prime its imaginary part, such as $\sigma' = \Im\{\sigma_0 e^{i\omega t}\}$ and $\sigma'' = \Re\{\sigma_0 e^{i\omega t}\}$. This leads to the definition of the complex number G^*:

$$\begin{aligned} \sigma_0 &= |G^*|\gamma_0 \\ G^* &= G' + iG'' \end{aligned} \tag{1.52}$$

So,

$$\begin{aligned} \sigma_0 &= |G^*|\gamma_0 \\ \sigma &= G'\gamma_0 \sin(\omega t) + iG''\gamma_0 \cos(\omega t) \end{aligned} \tag{1.53}$$

Another way to characterize these experiments is in terms of a sinusoidal strain rate [1, 5], leading to the definition of a dynamic viscosity material function η^*.

$$\begin{cases} \eta' = \frac{\sigma_0''}{\dot{\gamma}_0} = \frac{G''}{\omega} \\ \eta'' = \frac{\sigma_0'}{\dot{\gamma}_0} = \frac{G'}{\omega} \end{cases} \tag{1.54}$$

1.4 Different types of rotational or shear rheometers

In order to carry out the tests described earlier, measuring devices have been developed, the rheometers. There are several kind of rheometers, each with some advantages and some drawbacks. We will focus here on shear rheometers and describe the different ways the test is controlled.

1.4.1 Controlled strain rheometers

A controlled strain, or CR, rheometer applies a controlled shear rate as an input and determine the resulting shear stress. Two different kind of measuring systems exist.

1.4.1.1 CR rheometer with a Searle type measuring system

The upper plate (rotor) is driven by a motor, which speed is controlled, see Figure 1.11. The lower plate is held at rest and can be jacketed for an accurate temperature control. The resistance of the liquid being sheared between the two boundaries (one is stationary, one is rotating) of the sensor system results in a viscosity-related torque which is acting on the upper plate which counteracts the torque provided by the drive motor. A torque detector is placed between the

drive motor and the shaft of the upper plate. In this case, Searle means that both the rotor and the torque detector are acting on the same motor axis.

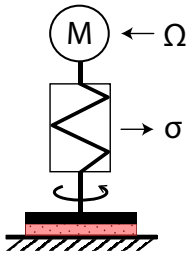

Figure 1.11: Searle type sensor on CR rheometers: rotor rotates, torque is measured on the rotor axis, while the lower plate or outer cylinder (depending on the geometry in use) is stationary.

A change in the geometry of the sensor system allows to also use coaxial cylinders and cone-and-plate geometry.

1.4.1.2 CR rheometer with a Couette type measuring system

The lower plate is driven by a motor at a define speed, see Figure 1.12. The resistance of the liquid against the flow transmits a viscosity-related torque on the upper plate, which would induce it to rotate as well. This torque in measured by determining which value of the counteracting torque is needed to hold the upper plate still. The Couette design here means the drive acts on the lower plate or the outer cylinder, while the viscosity-related torque is measured on the shaft of the upper plate, the upper cone or the inner cylinder. Instead of a spring as a torque sensing element, a secondary motor provides the torque necessary to prevent the upper plate, the upper cone or the inner cylinder from starting to rotate. Couette type measuring systems maintain laminar flow even when low viscosity liquids are tested at high shear rates, and it is in this area that they usually surpass Searle-type CR-rheometers. Assuming for Searle and Couette measuring systems that the gap used is very small and that the same value of rational speed is used on either the upper or lower plate, the viscosity of a Newtonian liquid is constant across the gap and equal for both measuring systems.

1.4.2 Controlled stress rheometers

When using a controlled stress, or CS, rheometer a user-defined torque is applied to the material, while the resulting shear rate or the motor speed is measured. As with CR rheometers, Couette and Searle measuring systems can also be used. Viscosity measurements are then done using the pre-set torque value to calculate the shear stress, and the measured rotor speed to calculate the shear rate, and so the viscosity.

Originally, the CS-rheometers were designed to provide a higher sensitivity at very low shear rates. They are also especially designed to determine the visco-elastic properties of fluids and solids, which, subjected to small strains in a creep test or to small oscillation amplitudes in a dynamic test are just elastically deformed but are never forced to flow. Because of their design, they can more

accurately measure non-Newtonian parameters such as yield stress and thus better account for switch from solid to viscous behavior of materials as a function of shear rate or history. Nowadays, several rheometers have the ability to control both the torque and the displacement, making them versatile tools to characterize complex materials.

1.5 Different types of geometry

Once the controlling and the measuring systems are chosen, one has to choose between a range of geometry. The links between torque and shear stress and between angular velocity and shear rate depend on the chosen geometry. Each geometry comes with specificities, and with a set of hypothesis that has to be verified to ensure the relevance and the validity of the test.

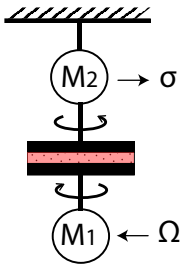

Figure 1.12: Couette type sensor on CR rheometers: lower plate or outer cylinder (depending on the geometry in use) rotates, the torque is sensed on the inner non-rotating cylinder, plate or cone.

1.5.1 Concentric cylinders

1.5.1.1 Assumptions and equations of motion

This concept was first made practical by Maurice Couette in 1890 [5]. Couette used a rotating outer cup and a torsion wire suspended inner cup. Working on the equations linking the shear stress with the torque measurements, the shear rate with the angular velocity, and the normal stress coefficients with the radial pressure difference is essential in order to fully understand experimental settings and experimental data. These equations are given below. We consider the flow of a fluid confined between concentric cylinders with a rotating inner cylinder, as shown in Figure 1.13.

The equations of motion in cylindrical coordinates are reminded in A.2. Several assumptions can be defined in order to simplify the equations:

- Steady, laminar and isothermal flow
- $v_\theta = r\omega$ only, and $v_r = v_z = 0$
- Gravity and end effects are negligible
- Symmetry in θ, therefore $\frac{\partial}{\partial \theta} = 0$

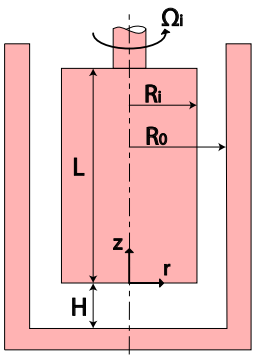

Figure 1.13: Schematic of a concentric cylinder rheometer.

Using these assumptions, we can write:
r-Component

$$-\rho\frac{v_\theta^2}{r} = \frac{1}{r}\frac{\partial}{\partial r}(r\tau_{rr}) - \frac{\tau_{\theta\theta}}{r} \tag{1.55}$$

θ-Component

$$0 = \frac{\partial}{\partial r}(r^2\tau_{r\theta}) \tag{1.56}$$

z-Component

$$0 = -\frac{\partial p}{\partial z} + \rho g_z \tag{1.57}$$

Equations 1.55, 1.56 and 1.57 can be used to determine the normal stress, the shear stress and the hydrostatic pressure in the gap, respectively. According to the geometry described in Figure 1.13, we can define the boundary conditions:

- $v_\theta = \omega_i R_i$ at $r = R_i$
- $v_\theta = 0$ at $r = R_0$ [1]

1.5.1.2 Shear stress

By integration of equation 1.56 over r, we find:

$$\tau_{r\theta} = \frac{c_1}{r^2} \tag{1.58}$$

The integration constant c_1 can be easily determined, using a torque balance on the inner cylinder [2]:

$$\frac{M_i}{R_i} = \tau_{r\theta}(R_i)2\pi R_i L \tag{1.59}$$

where M_i is the torque on the inner cylinder. Thus we have:

$$c_1 = \frac{M_i}{2\pi L}\tau_{r\theta}(R_i) = \frac{M_i}{2\pi R_i^2 L} \tag{1.60}$$

[1] If both cylinders are rotating, we have $v_\theta = \omega_0 R_0$ at $r = R_0$
[2] If the torque is measured on the outer cylinder, we have $\frac{M_0}{R_0} = \tau_{r\theta}(R_0)2\pi R_0 L$

1.5.1.3 Shear strain and shear rate

For narrow gaps ($K = \frac{R_i}{R_0} \geq 0.99$), the curvature of the geometry can be neglected. We can then define the strain as [5]:

$$B_{r\theta} = \gamma = \frac{\Delta x}{\Delta r} = \frac{\theta \bar{R}}{R_0 - R_i} \tag{1.61}$$

Where θ is the angular displacement of the cylinder and $\bar{R}$ is the point between the two cylinders such as:

$$\bar{R} = \frac{R_0 + R_i}{2} \tag{1.62}$$

Similarly, it is possible to assume the velocity gradient is a constant across the gap, and thus the shear rate is the average between the two cylinders:

$$\dot{\gamma}(R_i) = \frac{\Delta v}{\Delta r} = \frac{\Omega_i \bar{R}}{R_0 - R_i} \tag{1.63}$$

For a wider gap, (i.e. when $K \leq 0.99$), we cannot assume that the velocity gradient is constant across the gap. From the components of the rate of deformation tensor in cylindrical coordinates, we can write the shear rate as:

$$|2D_{r\theta}| = \dot{\gamma} = \frac{\partial v_\theta}{\partial r} - \frac{v_\theta}{r} = r\frac{\partial}{\partial r}\frac{v_\theta}{r} = r\frac{\partial \Omega}{\partial r} \tag{1.64}$$

The shear rate is thus not constant across the gap. In principle, to evaluate the derivative of the previous equation, we need actual measurements of the velocity profile. However, such measurements can be very difficult. A way to avoid that is to use the equation 1.58 to make the shear rate a function of the shear stress:

$$\dot{\gamma}(r) = |r\frac{d\Omega}{dr}| = 2\tau_{r\theta}\frac{d\Omega}{d\tau_{r\theta}} = \dot{\gamma}(\tau)_{r\theta} \tag{1.65}$$

Integrating this for a rotating inner cylinder and a stationary outer cylinder[3], we find:

$$\int_0^{\Omega_i} d\Omega = \Omega_i = \int_{\tau_{R_0}}^{\tau_{R_i}} \frac{\dot{\gamma}(\tau)}{2\tau} d\tau \tag{1.66}$$

where $\dot{\gamma}(\tau)$ is a function linked to the type of material tested (Newtonian, power law...).

[3]The use of $\Omega = \Omega_i$ at R_i and $\Omega = 0$ at R_0 is an expression of the no slip condition.

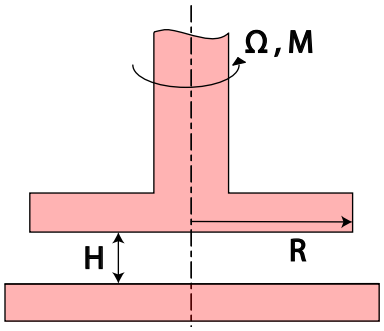

Figure 1.14: Schematic of a parallel plates geometry.

1.5.2 Parallel plates

1.5.2.1 Assumptions and equations of motion

The parallel disk geometry is a commonly used geometry, suggested by Mooney in 1934. This geometry is sketched in Figure 1.14. We now assume:

- Steady, laminar and isothermal flow
- $v_\theta(r, z)$ only, and $v_r = v_z = 0$
- Negligible body force
- Cylindrical edge

The equations of motion can be reduced to:

r-Component

$$\frac{1}{r}\frac{\partial}{\partial r}(r\tau_{rr}) - \frac{\tau_{\theta\theta}}{r} = -\rho\frac{v_\theta^2}{r} \tag{1.67}$$

θ-Component

$$\frac{\partial \tau_{\theta z}}{\partial z} = 0 \tag{1.68}$$

z-Component

$$\frac{\partial \tau_{zz}}{\partial z} = 0 \tag{1.69}$$

1.5.2.2 Velocity, shear rate and shear strain

We consider one disk as stationary, and the other one rotating at Ω. We assume we do not have slip at these surfaces and consider the inertial forces as negligible. In these conditions the velocity can be written:

$$v_\theta(r, z) = \frac{r\Omega z}{h} \tag{1.70}$$

Thus, the shear rate is expressed as follow:

$$\dot{\gamma}(r) = \frac{r\Omega}{h} \tag{1.71}$$

and the strain can be written:

$$\gamma(r) = \frac{r\theta}{h} \tag{1.72}$$

The strain and the shear rate thus vary from zero at the center of the geometry up to their maximum value at the rim of the geometry.

1.5.2.3 Shear stress

The shear rate is not constant through the geometry, as in a wide gap Couette flow. Similarly we must use a derivative to relate the shear stress to the total torque. If we consider the differential torque on an angular ring of thickness dr:

$$dM = (2\pi r dr)\tau r \tag{1.73}$$

Thus, we have:

$$\int_0^M dM = M = 2\pi \int_0^R r^2 \tau(r) dr = \frac{2\pi R^3}{\dot{\gamma}_R^3} \int_0^R \gamma^2 \tau(\gamma) d\gamma \tag{1.74}$$

By rearranging and differentiating using the Leibniz integral rule[4] [5, 6, 7], the stress can be expressed as follow::

$$\tau = \frac{M}{2\pi R^3} \left(3 + \frac{\partial \ln(\frac{M}{2\pi R^3})}{\partial \ln \gamma_R} \right) \tag{1.75}$$

The evaluation of the shear stress for an unknown fluid goes through a necessity of large enough amount of data of $\ln(\frac{M}{2\pi R^3})$ versus $\ln \gamma_R$ to determine the derivative accurately. In practice, this is most of the time not highly difficult. If the test material is Newtonian, the derivative equals 1, so the shear stress becomes:

$$\tau_{app} = \frac{2M}{\pi R^3} \tag{1.76}$$

This shear stress is also called the apparent shear stress and is often used to calculate the apparent viscosity.

[4] Assuming a function F exists, can be differentiated and is defined as $F(y) = \int_{a(y)}^{b(y)} f(y,z)dz$, we have $\frac{dF(y)}{dy} = f(y,b(y))\frac{db(y)}{dy} - f(y,a(y))\frac{da(y)}{dy} + \int_{a(y)}^{b(y)} \frac{\partial}{\partial y} f(y,z)dz$

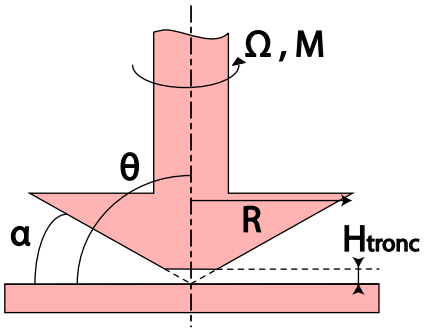

Figure 1.15: Schematic of a cone-and-plate geometry.

1.5.3 Cone and plate

1.5.3.1 Assumptions and equations of motion

The cone-and-plate geometry is widely used because of its constant rate of shear. The proper coordinates for this problem are the spherical ones, see Figure 1.15. The equations of motion in spherical coordinates are reminded in A.2.

We do several assumptions in order to simplify these equations:

- Steady, laminar and isothermal flow
- $v_\phi(r, \theta)$ only, and $v_r = v_\theta = 0$
- $\alpha \leq 0.10$ rad
- Negligible body force
- Spherical liquid boundary

These assumptions allow us to write:

$$r-\text{Component}$$
$$\rho \frac{v_\phi^2}{r} = \frac{1}{r^2}\frac{\partial}{\partial r}(r\tau_{rr}) - \frac{\tau_{\theta\theta} + \tau_{\phi\phi}}{r} \tag{1.77}$$

$$\theta-\text{Component}$$
$$0 = \frac{1}{r\sin\theta}\frac{\partial}{\partial \theta}(\tau_{\theta\theta}\sin\theta) - \frac{\cot\theta\tau_{\theta\theta}}{r} \tag{1.78}$$

$$\phi-\text{Component}$$
$$0 = \frac{1}{r}\frac{\partial \tau_{\theta\phi}}{\partial \theta} + \frac{2}{r}\cot\theta\tau_{\theta\phi} \tag{1.79}$$

We can also specify two boundary conditions:

$$\begin{aligned} v_\phi\left(\frac{\pi}{2}\right) &= 0 \\ v_\phi\left(\frac{\pi}{2}-\alpha\right) &= \Omega r \sin\left(\frac{\pi}{2}-\alpha\right) \approx \Omega r \end{aligned} \tag{1.80}$$

1.5.3.2 Shear stress

The shear stress can be found thanks to 1.79. If we integrate this equation, we find:

$$\tau_{\phi\theta} = \frac{C_1}{\sin^2\theta} \tag{1.81}$$

We then do a torque balance on the plate:

$$M = \int_0^{2\pi}\int_0^R r^2\tau|_{(\pi/2)} dr d\phi = \frac{2\pi R^3}{3}\tau_{\phi\theta}|_{(\pi/2)} \tag{1.82}$$

Using 1.81 in 1.82, we obtain:

$$\tau_{\phi\theta}(\theta) = \frac{3M}{2\pi R^3 sin^2\theta} \tag{1.83}$$

Reminding that $\alpha < 0.1$rad we can consider that $sin^2\theta = sin^2(\pi/2-\alpha) \approx 1$ and that the shear stress is globally constant throughout the material.

$$\tau_{\phi\theta} = \frac{3M}{2\pi R^3} \tag{1.84}$$

1.5.3.3 Shear strain and shear rate

Since the shear stress is nearly constant, the shear strain and the shear rate will also be nearly constant. From **B** in spherical coordinates, we have:

$$B_{\phi\theta} = \gamma = \frac{\phi}{\alpha} \tag{1.85}$$

Similarly from **D** in spherical coordinates

$$|2D_{\phi\theta}| = \dot{\gamma} = |\frac{\sin\theta}{r}\frac{\partial}{\partial\theta}(\frac{v_\phi}{\sin\theta})| = |\frac{1}{r}\frac{\partial v_\phi}{\partial\theta} - \frac{v_\theta}{r}\cot\theta| \tag{1.86}$$

Because $\theta = \pi/2 - \alpha$, we can write:

$$\cot\theta = \cot(\frac{\pi}{2}-\alpha) = \tan\alpha \approx \alpha \tag{1.87}$$

A good approximation of the velocity profile being

$$v_\phi = \Omega r \frac{(\pi/2) - \theta}{\alpha} \tag{1.88}$$

So the shear rate is given by

$$\dot{\gamma} \approx \frac{\Omega}{\alpha} \tag{1.89}$$

1.6 Conclusion

The rheology is the study of the flow properties of materials. This science relies on the different notions defined above. From these theoretical tools, experimental methods (rheometry) were developed. As discussed above, several tools exist, good understanding of the existing rheometry solutions is therefore necessary to choose the best experimental system as possible. This choice is also linked to the type of information required as well as the type of material tested. Analysis of the existing literature is therefore a good way to first understand what can be going on within the material, and second choose the best experimental system. The next chapter thus focuses on the material tested during this project (suspensions).

References

[1] R.B. Bird, R.C. Armstrong, and O. Hassager. *Dynamics of Polymeric Liquids: Volume 1 Fluid Mechanics*. Wiley, 1987.

[2] L. Boltzmann. Zür theorie der elastischen nachwirkung. *Sitzungsber. Kaiserlich Akad. Wiss.*, 70:275–306, 1874.

[3] J.D. Ferry. *Viscoelastic properties of polymers*. Wiley, 1980.

[4] R.G. Larson. *The structure and Rheology of complex fluids*. Oxford University Press, New York, 1999.

[5] C.W. Macosko. *Rheology: principles, measurements and applications*. Wiley-VCH, New York, 1994.

[6] P.R. Soskey and H.H. Winter. Large step shear strain experiments with parallel-disk rotational rheometers. *J. Rheol.*, 28:625 – 645, 1984.

[7] A. Yoshimura and R.K. Prud'Homme. Wall slip corrections for couette and parallel disk viscometers. *J. Rheol.*, 32:53–67, 1988.

Chapter 2

Suspension Rheology

Contents

Résumé du Chapitre

Dans ce chapitre, nous introduisons les principaux résultats connus sur la rhéologie des suspensions. Nous nous concentrons en premier lieu sur les suspensions de sphères dures, base de l'étude des suspensions.

Nous nous intéressons ensuite à l'influence de la forme des particules, pour ensuite résumer les principaux résultats liés à l'étude des suspensions de sphères déformables, qu'elles soient liquides, comme dans le cas des émulsions, ou élastiques.

Nous passons ensuite en revu les principales énergies d'interactions dans les systèmes colloïdaux, des interactions de Van der Walls à la déplétion, en passant par les interactions hydrophiles.

Nous terminons ce chapitre avec une revue des principaux résultats présents dans la littérature sur les suspensions agrégées, créant des réseaux pouvant être étonnement solides.

2.1 Introduction

A suspension consists of discrete solid particles randomly distributed in a fluid medium. The rheology of suspensions in a Newtonian fluid has been widely studied in the last decades. Many materials in use today are disperse systems where particles are dispersed in another phase, therefore any new insights in the rheology of these systems can be of great practical importance, from biological materials such as milk or blood, to paint, ink, ceramics, etc [52].

The addition of rigid spheres into a liquid medium induces a hydrodynamic disturbance. This disturbance, first calculated by Einstein has a small effect on viscosity. However, if the spheres are small enough (generally below a micron), colloidal forces between particles can become important, resulting in an increase in viscosity that can be more of an order of magnitude, even at low concentration. Adding particles does not only change the magnitude of the viscosity as displayed in Figure 2.1. The addition of particles can introduce non-Newtonian behaviours such as shear thinning, shear thickening, yield stress behaviour, but also time-dependent behaviour such as thixotropy.

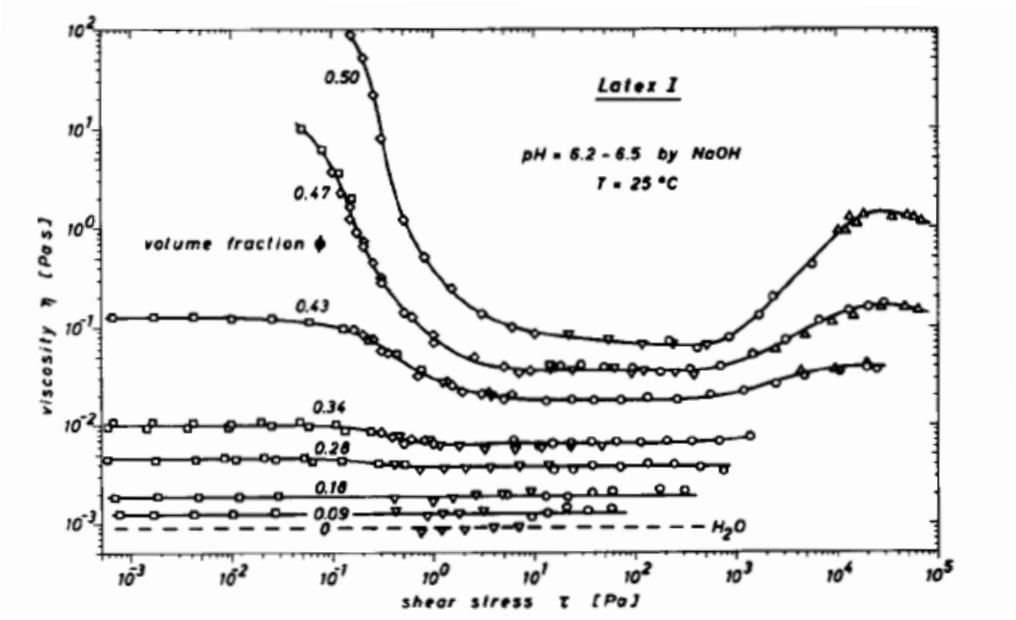

Figure 2.1: Viscosity as a function of shear stress for a polystyrene ethyl-acrylate latex at different volume fractions, from [49].

The physical properties of the dispersed particles, such as the average particle size, the size distribution, the type and the magnitude of the energy of

interaction between the particles or the shape of the particles influence the overall materials properties [73].

In this chapter, the main known parameters that influence the flow behaviour of suspensions are reviewed, starting with hard spheres, then hard non-spherical particles, followed by deformable particles, up to particles having electrostatic interactions and aggregating systems.

2.2 Hard spheres suspensions

Hard spheres suspensions have been extensively studied, uncovering several important parameters when one wants to characterize the rheology of such materials.

2.2.1 Dimensional analysis

The first dimensional analysis of this kind of problem was done by Krieger [46]. He focused on the simplest case: a suspensions of rigid monodisperse spheres suspended in a Newtonian fluid. Assuming that the only interactions existing between the particles were hydrodynamic, Krieger showed that parameters of interest are the suspending fluid viscosity η_f, its density ρ_f, the radius of the particles a, their concentration or number density N, their density ρ_p and when Brownian motion is significant a thermal energy variable kT, with T the absolute temperature and K the Boltzmann constant. The main variables being the shear (whether it is the shear rate $\dot{\gamma}$ or the shear stress σ) and the duration of the experiment t_{Ex}, the equation of state can thus be written as

$$\eta = \eta(\dot{\gamma}, t_{Ex}, \eta_f, \rho_f, a, N, \rho_p, kT) \tag{2.1}$$

Six dimensionless groups are necessary to describe such a system. A convenient set is the relative viscosity $\eta_r = \eta/\eta_f$, the volume fraction $\varphi = \frac{4\pi}{3} N a^3$, a relative density $\rho_r = \rho_p/\rho_f$, an internal Reynolds number $Re_i = a^2\dot{\gamma}\rho_f/\eta_f$, the Deborah number $De = t_{Br}/t_{Ex}$ and the Péclet number $Pe = t_{Br}\dot{\gamma}$. Therefore the reduced equation of state form is

$$\eta_r = \frac{\eta}{\eta_f} = \eta_r(\varphi, \rho_r, Re_i, Pe, De) \tag{2.2}$$

The last two dimensionless quantities introduced depend on the Brownian diffusion time of particles in a suspending fluid

$$t_{Br} = \frac{a^2}{D_T} = \frac{6\pi\eta_f a^3}{KT} \tag{2.3}$$

Under steady conditions, a constant shear is applied on the material until an equilibrium is reached, therefore under this condition, $De \to 0$, in the case of neutrally buoyant particles, $\rho_r \to 1$, and if the experiments are conducted under

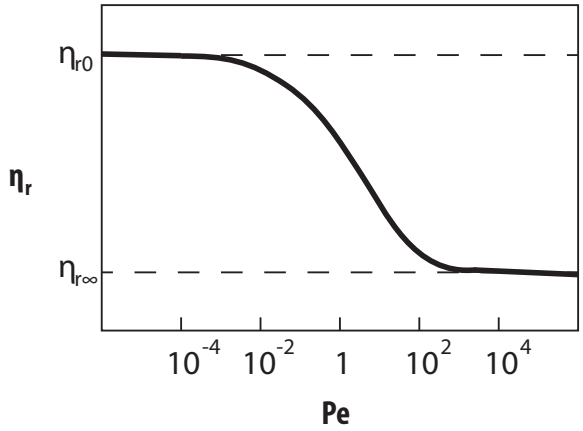

Figure 2.2: Relative viscosity as a function of the Peclet number: representation of the master curve from dimensional analysis.

laminar flow conditions, $Re_i \to 0$. Under all these conditions, equation 2.2 is reduced to $\eta_r = \eta_r(\varphi, Pe)$. In the case of $\varphi = cst$, a master curve $\eta_r = \eta_r(Pe)$ can be represented which general shape is as display in Figure 2.2.

2.2.2 Influence of the average particle size

In the case where a constant volume fraction is required, the use of smaller particles implies that more particles are present in the sample, as depicted in Figure 2.3. Because of this increase in the number of particles, the amount of particle-particle interactions increases which induces an increase in the relative viscosity [46], see Figure 2.4.

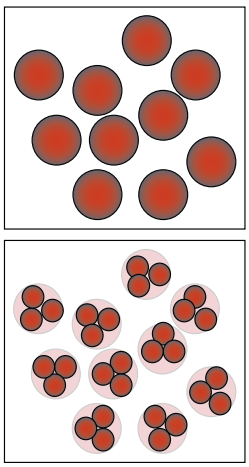

Figure 2.3: Schematic showing the need for more smaller particle in order to have a volume fraction constant.

2.2.3 Influence of the size distribution

Mixing monodisperse spheres with strongly different diameters results in a substantial increase in maximum packing which leads to a substantial decrease in viscosity [17, 27]. This decrease in viscosity is sensitive to the volume fraction and to the ratio of size between the large and the small particles. For very large ratio, the small particles can fill the interstices between the large ones up to their maximum packing, increasing the maximum packing fraction for

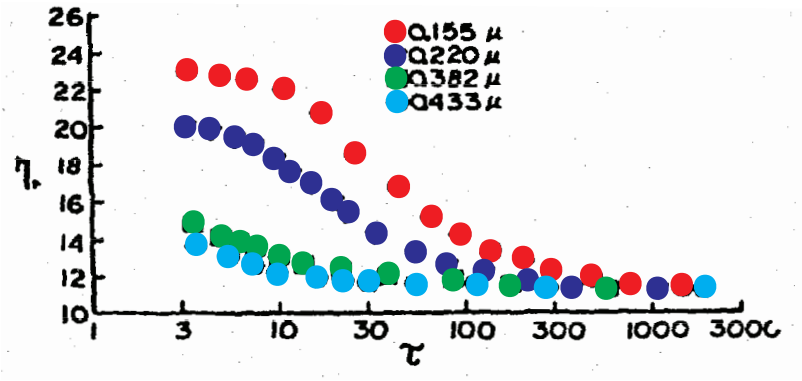

Figure 2.4: Relative viscosity as a function of the shear stress for 50% monodispersions in benzyl alcohol of four different particle sizes of cross-linked polystyrene spheres, from [46].

a monodisperse system φ_m to a maximum packing fraction for a bimodal system $\varphi_{m,m}$ [54]:

$$\varphi_{m,m} = \varphi_m + (1 - \varphi_m)\varphi_m \tag{2.4}$$

If the ratio of size is below 10, the small particles do not fit well in the interstices, which lead to an a decrease of the maximum packing, and so an increase of the viscosity, as shown in Figure 2.5.

Further reduction in viscosity is possible if trimodal or higher multimodal systems are used, even though it becomes quickly difficult to produce particles small enough in the case of highly multimodal systems. The use of multimodal size distributions also delay the onset of shear thickening [54].

2.2.4 Influence of Brownian motion

When the particles in the suspension are small enough and/or the temperature of the material is high enough, thermal motion of the particles within the suspending fluid can not be ignored anymore. We place ourselves in the case where only the hydrodynamic and thermal forces are not negligible. The Péclet number is thus the relevant parameters to study the flow behaviour of the system. General viscosity curves are shown in Figure 2.1. Two Newtonian regions can be observed, with a shear thinning region between them. At very high concentrations, shear thickening can appear if the shear applied is high enough, indicating complex structural changes [5, 50].

2.2.4.1 Péclet number in concentrated systems

The Péclet number defined earlier is based on Stokes' law for the hydrodynamic effect, therefore on the diffusivity of an isolated sphere. In concentrated suspensions, this does not hold, as the viscous resistance encounters by a particle will be

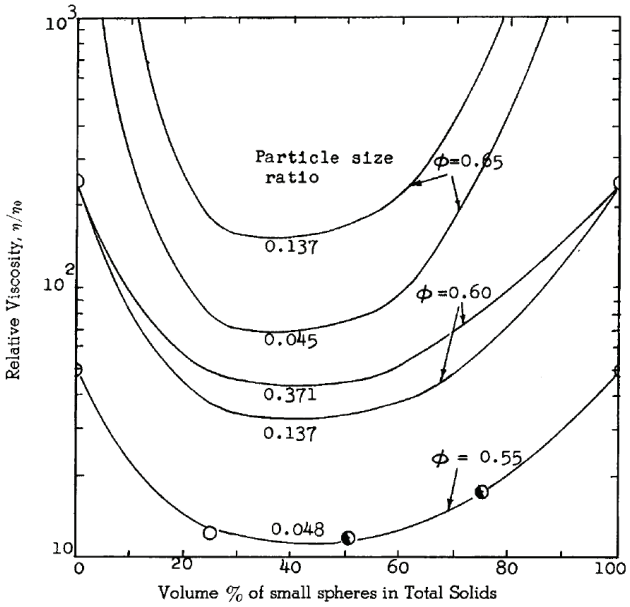

Figure 2.5: Relative viscosity as a function of the volume % of small spheres in total solid for various particle size ratio, from [17].

the sum of all the hydrodynamic interactions with all the neighbouring particles. The resistance will therefore be significantly higher than what is predicted by Stokes' law. Krieger suggested that this resistance should be comparable with the global viscosity of the suspension, therefore to substitute the medium viscosity in the Péclet expression with the suspension viscosity. Such an expression of the Péclet number can be seen as a reduced shear stress σ_r:

$$Pe = \frac{6\pi\eta a^3}{KT}\dot{\gamma} = \frac{6\pi a^3}{KT}\sigma = \frac{\sigma}{\sigma_c} = \sigma_r \tag{2.5}$$

The curves of the evolution of the viscosity of the suspension as a function of the reduced shear stress can be well described by the semi-empirical relation [46]:

$$\frac{\eta - \eta_\infty}{\eta_0 - \eta_\infty} = \frac{1}{1 + \sigma_r} \tag{2.6}$$

where $\eta_0 = \lim_{\sigma\to 0}$ is the zero-shear or low shear viscosity and $\eta_\infty = \lim_{\sigma\to\infty}$ is the high shear viscosity. An example of this is shown in Figure 2.6. For the three smallest particle sizes, superposition is excellent, however, it is not for the larger particles. Krieger considered this as an independent evidence from sedimentation behaviour that large particles form long-lived aggregates, due to the secondary minimum in the interparticle potential curve [46].

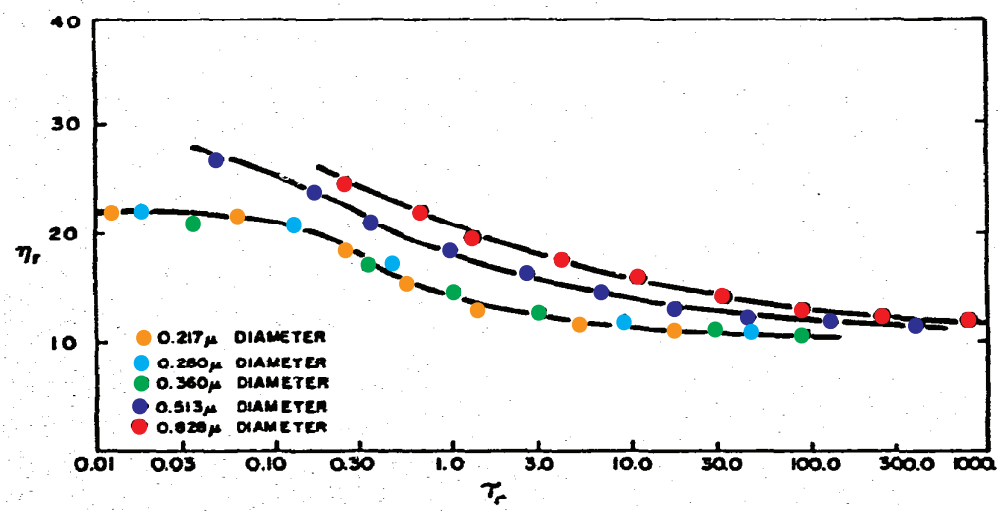

Figure 2.6: Relative viscosity as a function of the relative shear stress for aqueous monodisperse latices at a volume fraction of 50% for various particle sizes, from [46].

2.2.4.2 Evolution of the viscosity with the volume fraction

The linear term in the concentration law for the viscosity was first derived from the viscous dissipation produced by the flow around a single sphere [24, 25]:

$$\eta_r = 1 + 2.5\varphi + \mathcal{O}(\varphi^2) \tag{2.7}$$

Thus the intrinsic viscosity, defined as $[\eta] = \lim_{\varphi \to 0}(\eta_r - 1)/\varphi$ is exactly 5/2, regardless of the size or the size distribution of the spheres. This equation is valid only for very disperse spheres ($\varphi \leqslant 0.03$), as such to avoid interaction with each other and thus to make sure they are not influenced by the presence of neighbouring particles. When the volume fraction is higher, the hydrodynamic interactions can not be neglected anymore. Computing the effect of two body interactions on the viscosity, the quadratic term was calculated and published by Batchelor [8]:

$$\eta_r = 1 + 2.5\varphi + 6.2\varphi^2 + \mathcal{O}(\varphi^3) \tag{2.8}$$

This formula holds for $\varphi \leqslant 0.10$. Three body hydrodynamic interactions would produce a term proportional to φ^3, and so on, however because higher order expansions are applicable over increasingly small concentration regions, such an approach was dismissed for studying more concentrated systems [52].

Another kind of approach was thus followed. In the two Newtonian regions, the relative viscosities should be universal for monodisperse hard spheres, as no length of time scales are left in the scaling. Therefore, these two viscosities should be independent of the shear, the medium viscosity, the temperature or even the particle size. In between these two regions, the Péclet number can be used to scale the shear. On the low shear Newtonian plateau, Brownian motion dominates the structure of the material, and hence its viscosity, meaning that the

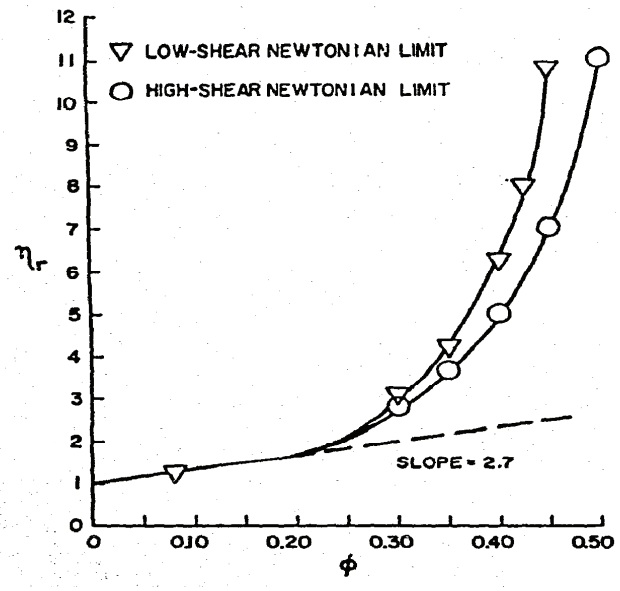

Figure 2.7: Test of Krieger-Dougherty equation for concentrated dependence of high and low-shear limiting viscosities, from [46].

positions of the particles at low enough shear is close to the one at rest. However, when the shear increases, the hydrodynamic forces start to compete with the thermal forces, until another equilibrium is found (i.e. the second Newtonian plateau). The Krieger-Dougherty relation [46] describes well the concentration dependence of the viscosity for these two Newtonian plateaus, as shown in Figure 2.7:

$$\eta_{rx} = \left(1 - \frac{\varphi}{\varphi_{mx}}\right)^{-2.5\varphi_{mx}} \tag{2.9}$$

where when $x = 0$ (low shear plateau), $\varphi_{m0} = 0.63$ (maximum packing volume ffraction at low shear) and when $x = \infty$ (high shear plateau), $\varphi_{m\infty} = 0.71$ (maximum packing volume fraction at high shear). The values of the different φ_{mx} however can be function of other parameters, such as the shape, the deformability or the size distribution of the particles.

An expression of the same type was later obtained by Quemada from a minimum principle applied to the energy dissipated by viscous effects [60]:

$$\eta_r = \left(1 - \frac{\varphi}{\varphi_m}\right)^{-2} \tag{2.10}$$

where φ_m is the maximum packing volume fraction. The difference between these two equations is the exponent, equals to the opposite of the product between the intrinsic viscosity and the maximum packing volume fraction for the Krieger-Dougherty equation, and equals to -2 for Quemada. Quemada argued that even if the condition $\lim_{\varphi\to 0} = 2.5$ is not maintained, it seems rather unjustified to require the existence of a relation between the exponent in these equation,

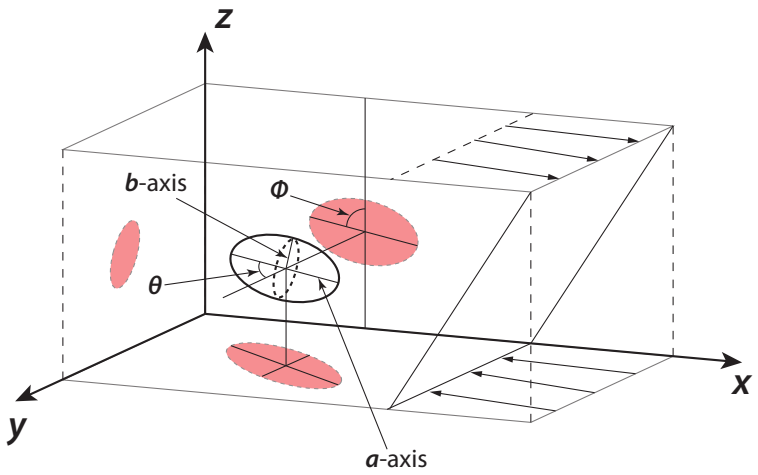

Figure 2.8: Prolate spheroid ($r_e > 1$) in simple shear flow. The a-axis is the axis of rotational symmetry of the particle. The angle ϕ is the angle between the projection of the a-axis on the xz plan and the z-axis, and the angle θ is the one between the projection of the a-axis on the xy plan and the y-axis, as displayed more in details on Figure 2.9.

φ_m, which mainly depends on lubrication interactions between close particles, and therefore commands the viscosity when the system is close to the maximum packing fraction, and $[\eta]$, which quantifies the long range hydrodynamic perturbation due to the presence of an isolated particle in the suspending fluid [61].

The divergent behaviour of the zero-shear viscosity was studied theoretically from a scaling analysis of the Brownian stress [13]. It was shown that if the range of the interparticle forces was comparable to the particle size, the hydrodynamic contribution to the stress scales as the Brownian stress, resulting with the zero-shear viscosity following Quemada's equation with a maximum packing volume fraction close to the random close packing volume fraction φ_{RCP} ($\varphi_{RCP} = 0.637$) [61].

2.3 Influence of the shape of the particles

The behaviour of non-spherical particles in shearing flow has been well studied for particles that have an axis of rotational symmetry and thus are symmetric along that axis (spheroids, cylinders, etc.) [56]. Such particles can be characterized by the particle aspect ratio $r_p = l_a/l_b$ where l_a is the length of the particle along the axis of symmetry and l_b is the maximum diameter perpendicular to the axis of symmetry. It has been shown that such particles can be considered as equivalent spheroid with aspect ration $r_e = a/b$ where a is the length of the semi-axis of symmetry and b is the length of the orthogonal semi-axis [14]. The relationship between r_p and r_e is usually determined experimentally.

Particles suspended in a viscous fluid rotate and get oriented by the shear along the flow's vorticity vector. From the motion of a spherical particle

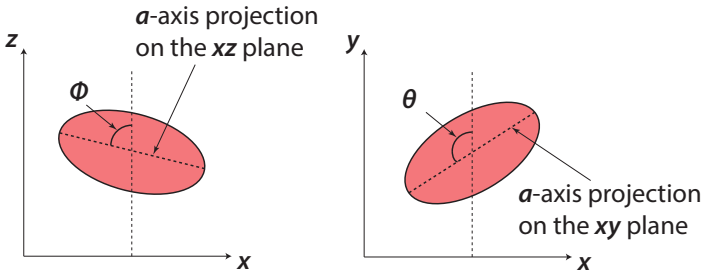

Figure 2.9: Projection of the particle profile in the xz and the xy plans to identify ϕ and θ. The angle ϕ is the angle between the projection of the a-axis on the xz plan and the z-axis, and the angle θ is the one between the projection of the a-axis on the xy plan and the y-axis.

in a dilute suspension undergoing shear, it is possible to define the tumbling rate [41, 56]

$$\dot{\phi} = \dot{\gamma}\frac{1}{1+{r_e}^2}({r_e}^2\cos^2(\phi)+\sin^2(\phi)) \tag{2.11}$$

where ϕ is the the angle between the plane containing the a-axis (axis of rotational symmetry) and the x-axis and the plane containing the x-axis and the y-axis, see Figure 2.8 and Figure 2.9 for the projections. The integration of this equation gives the period of rotation of the particle about the vorticity vector

$$T = \frac{2\pi}{\dot{\gamma}}\left(r_e + \frac{1}{r_e}\right) \tag{2.12}$$

The tumbling rate and period are independent of the angle between the a-axis and the vorticity vector (θ), defined as:

$$\tan(\theta) = \frac{Cr_e}{({r_e}^2\cos^2(\phi)+\sin^2(\phi))^{1/2}} \tag{2.13}$$

where C is an orbit constant, determined thanks to the previous equation only if θ and ϕ are known at any point. Even though they are tumbling, the particles spend more of the rotational period aligned with the flow than they do across the flow [56]. This effect increases as the aspect ratio deviates from unity. Jeffrey's equations have been validated numerically [43, 45] and experimentally [2, 32, 76].

The rate of work or power that is required to shear a volume of material V is related to the apparent viscosity of the material [34]

$$\dot{W} = \eta\dot{\gamma}^2 V \tag{2.14}$$

In the case of very dilute suspensions, it is possible to consider the material as if there was only one particle suspended in the fluid. Under this condition,

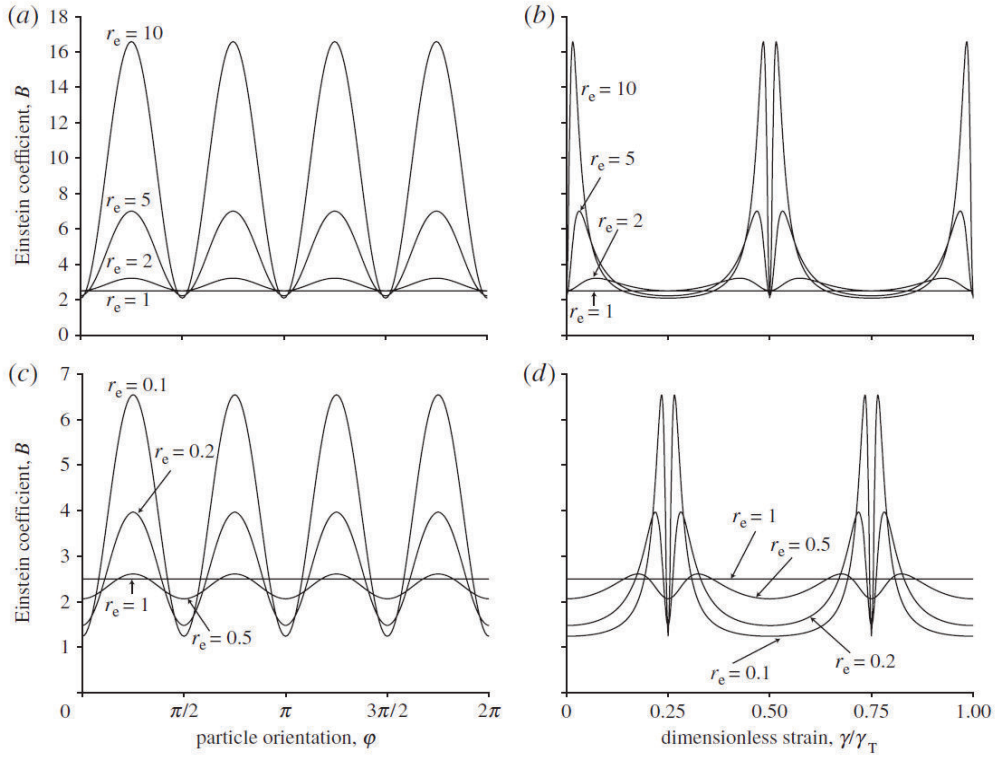

Figure 2.10: Einstein coefficient as a function of particle orientation (a,c) and dimensionless strain (b,d) for various equivalent spheroid aspect ratio, from [56].

the total rate of work is the sum of the rate of work that must be done to shear the fluid ($\dot{W}_f$) and of the work owing to the presence of the particle ($\dot{W}_p$). The apparent viscosity of the material can therefore be written as

$$\eta = \frac{\dot{W}_f}{\dot{\gamma}^2 V} + \frac{\dot{W}_p}{\dot{\gamma}^2 V} \tag{2.15}$$

Considering a Newtonian suspending fluid, we directly have $\eta_f = \dot{W}_f/\dot{\gamma}^2 V$, therefore the previous equation can be written again as

$$\eta_r = 1 + \frac{\dot{W}_p}{\eta_f \dot{\gamma}^2 V_p}\varphi \tag{2.16}$$

where V_p is the volume of the particles and φ is the volume fraction. The analogy with Einstein's equation (2.7) allows the determination of the Einstein's coefficient (the intrinsic viscosity in the case of spherical particles).

For orbits $C = 0$, the axis of symmetry of the particle is aligned with the vorticity vector, therefore the particle rolls along in the flow with steady motion, thus the contribution of the particle to the viscosity of the suspension is constant with shear. For every other values of C, and therefore for any other orbits, the contribution of the particle to the viscosity of the material is dependent on the angle ϕ. Figure 2.10 shows the evolution of Einstein's coefficient, and therefore of

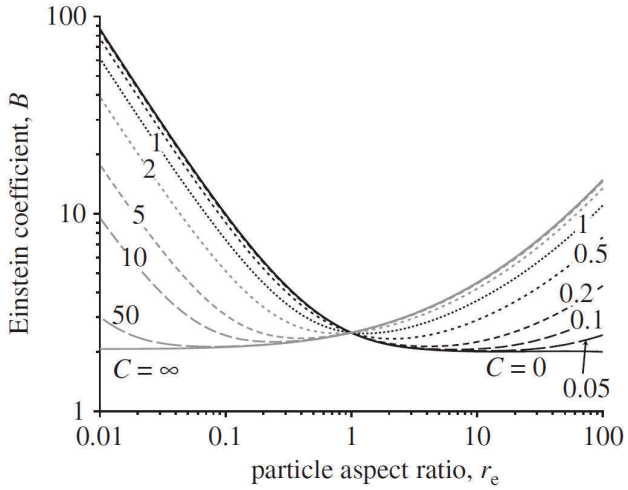

Figure 2.11: Einstein coefficient as a function of particle aspect ratio for different particle orientations, from [56].

the particle's contribution to the viscosity, for $C = \infty$. Under this condition, the particle is tumbling in the flow with its axis of symmetry perpendicular to the vorticity vector [41, 56]. It can be seen in Figure 2.10 that according to particle's orientation and the strain, the Einstein's coefficient can be lower or higher than 2.5, meaning a lower or a higher viscosity than in the case of spherical particles, respectively. Figure 2.11 shows the influence of the particle aspect ratio on the Einstein viscosity for various orbit constants.

2.4 Deformable spheres suspensions

A large range of particles can get deformed by the flow. It is therefore central to take these deformations into account as they can induce specific behaviours. There are two different cases that can be considered: first, the case of emulsions, where the particles are seen as fluid droplets of viscosity η_d, then the case of elastic particles of elastic modulus G_d.

2.4.1 Emulsions

An emulsion consists of droplets of a liquid of viscosity η_d dispersed in another of viscosity η_f. Many materials of practical importance consist of such systems, such as paint, soaps, cosmetics, creams, milk, etc. In emulsion, a useful dimensionless parameter is the ratio of the viscosity of the droplet liquid to that of the suspending fluid $\eta_{dr} = \eta_d/\eta_f$. If the viscosity ratio is very high, the behaviour of the suspension is close to the hard sphere case, however, if it is not, deviations can be witnessed.

A first deviation is linked to the shape of the particles. For small deformations, the drop assumes an elliptical form [75, 52], where the difference between major and minor axes, $2a$ and $2b$ respectively, depends on

$$D = \frac{a-b}{a+b} = 2\lambda_d II_{2D}^{1/2} \left(\frac{1 + 19\eta_{dr}/16}{1+\eta_{dr}} \right) \tag{2.17}$$

where II_{2D} is the second invariant of the rate of deformation, see equation 1.18 and λ_d is the relaxation time of the droplet, given by

$$\lambda_d = \frac{a\eta_d}{\Gamma} \tag{2.18}$$

where Γ is the interfacial tension. The interfacial tension tends to pull the drop back to a spherical shape, while the viscosity of the suspending fluid slows down the motion [52].

A second deviation is due to the break up of the drops in the flow. Indeed, a drop is always under balance between the interfacial forces that keep it together and the hydrodynamic forces that will deform and ultimately break it up [33]. The drop breakup depends on both the flow type and the viscosity ratio η_{dr}. If the viscosity ratio is very large, interfacial tension will have a negligible effect in shear flows. At high deformation rates, the drop will then align with the flow and assume a limiting shape [33]

$$\lim_{\dot{\gamma}\to 0} D = \frac{5}{2(2\eta_{dr}+3)} \tag{2.19}$$

For lower viscosity ratio, breakup can occur if the hydrodynamic forces exceeds the interfacial tension or $D > 1/2$ [1, 75]. For small deformations, the velocity field around the drop can be solved, however, in contrast with the hard spheres case, the fluid circulation inside the drop has to be considered [1, 68]. The constitutive relation for the particle stress is of the form [1, 52]

$$\boldsymbol{\sigma} = 2\eta_f \mathbf{D} \left[1 + \left(\frac{1 + \frac{5}{2}\eta_{dr}}{1+\eta_{dr}} \right) \varphi + F \right] \tag{2.20}$$

where F is function of η_{dr}, λ_d, and of the history of deformation. For steady shear, this equation can be reduced, and the steady shear viscosity can be written:

$$\eta = \eta_f \left[1 + \left(\frac{1 + \frac{5}{2}\eta_{dr}}{1+\eta_{dr}} \right) \varphi \right] \tag{2.21}$$

Once again, if the viscosity ratio η_{dr} is very large, the drop becomes rigid, and the coefficient of φ tends to 5/2, the Einstein's result. It is worthwhile to notice that for steady shear, equation 2.20 implies the existence of a positive first normal stress coefficient and of a negative second normal stress coefficient.

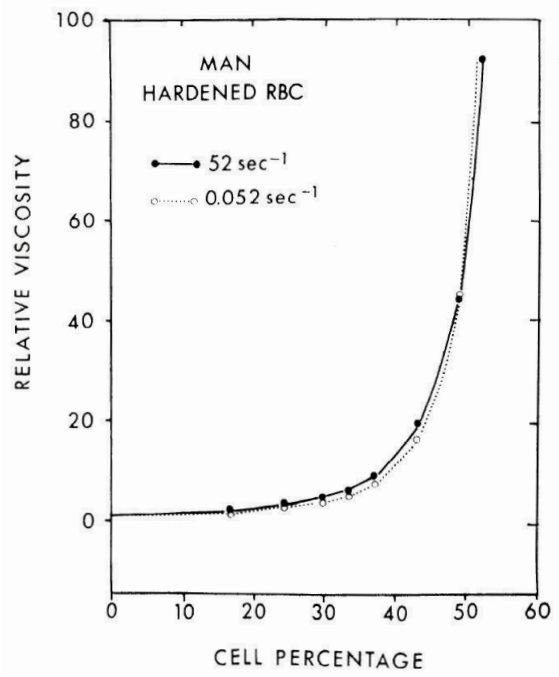

Figure 2.12: Relative viscosity as a function of the cell percentage at two different shear rates for hardened red blood cells, from [16].

2.4.2 Elastic particles

Another approach is to consider the particles as elastic spheres [31, 64]. In this case, the non-Newtonian effects come from the modulus G of the particle rather than from the interfacial tension. The previous equations can still be used with $\lambda_d = \eta_s/G$.

A good example of elastic particles suspension is blood. Red blood cells consist of a thin elastic membrane filled with a Newtonian fluid with a viscosity of $6 - 7$ mPas [70]. Studies have been made studying the flow of red blood cells suspension and of hardened red blood cells suspension [15, 16]. As shown in Figure 2.12, the relative viscosity of hardened red blood cells suspensions is globally independent of the shear applied. Red blood cells being too big to be influenced by Brownian motion at physiological temperature, the only parameter left is the volume fraction. In non-hardened red blood cells suspensions however, the shear is an important parameter. Figure 2.13 shows the effect of shear on the suspension: an increase in applied shear lowers the viscosity of the suspension. At very low shear, the viscosity of the suspension with normal deformability is close to the viscosity of the rigid cells suspensions, see Figure 2.14, and as the shear increases, shear thinning appears.

At high concentrations, the deformability of the particles can also have an impact on the packing of the particles. Indeed, at high concentrations, deformable particles can accommodate each other at rest and squeeze past each other during the flow, increasing φ_m and thus lowering the viscosity [6].

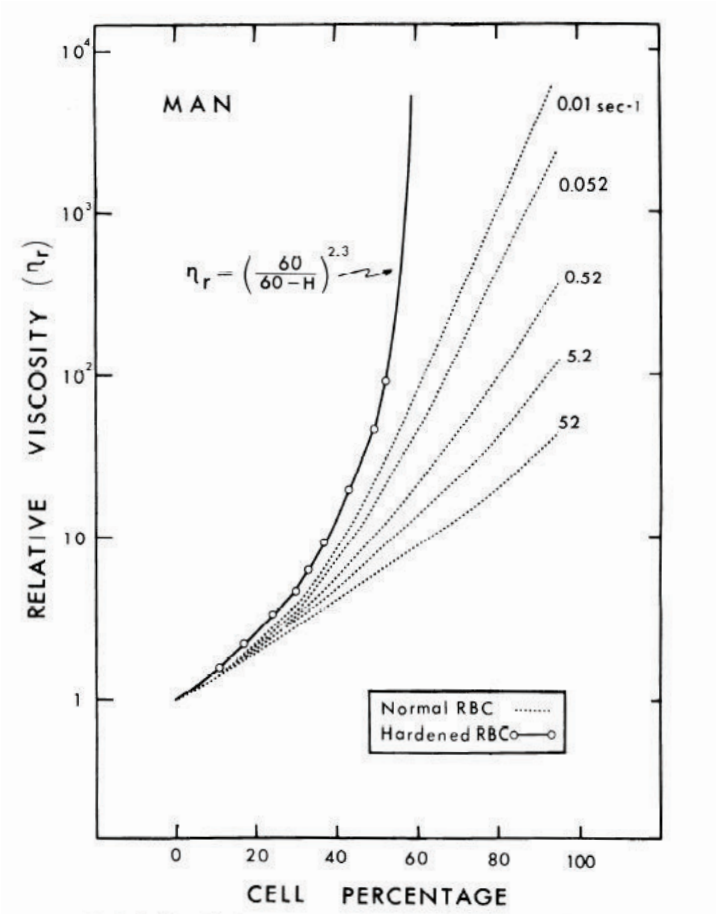

Figure 2.13: Relative viscosity as a function of the cell percentage at different shear rates for normal and hardened red blood cells, from [16].

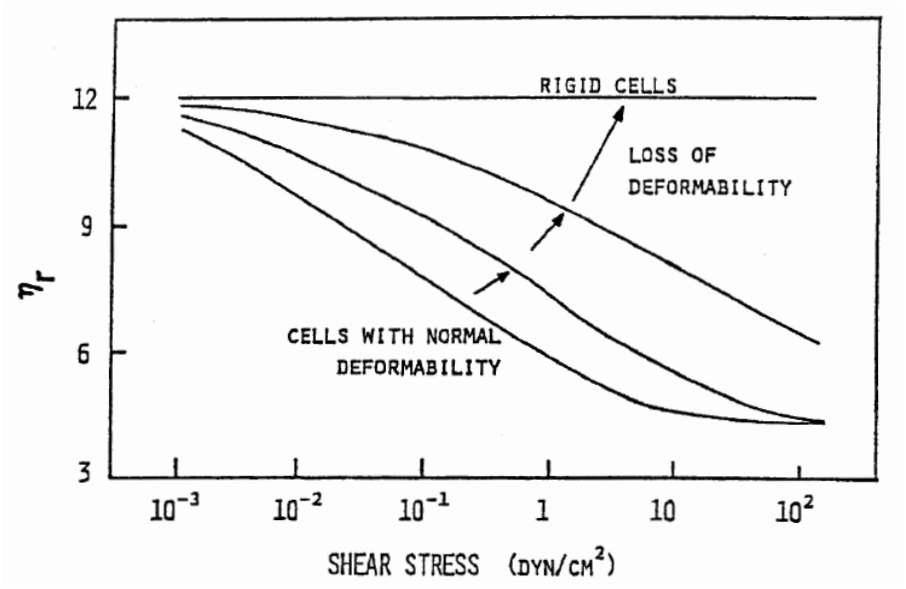

Figure 2.14: Relative viscosity as a function of the shear stress as the red blood cells lose deformability, from [15].

2.5 Pair interaction energy in colloidal systems

Interparticle forces govern the microstructure of suspension-type materials. Thus, it is essential to understand both their nature and their impact. Most of the studies on the interparticle forces have been done on colloids. So far, several kind of interparticle forces have been identified, the main ones being reviewed below.

2.5.1 Van der Waals interaction

In colloid systems, one of the first interaction to be identified was the van der Waals interaction. This force always exists because of interactions between induced dipoles in the molecules of neighbouring particles [53]. Integration of the interactions between all induced dipoles in two bodies results in an expression of the total force. Assuming spherical particles, the interaction can be expressed as [37, 62, 67]:

$$U_A = -\frac{A_{pmp}}{6}\left[\frac{2a^2}{R^2-4a^2} + \frac{2a^2}{R^2} + \ln\left(\frac{R^2-4a^2}{R^2}\right)\right] \tag{2.22}$$

where R is the center-to-center distance, a is the radius of the particles and A_{pmp} is the Hamaker constant for two particles acting across the medium. A_{pmp} being always positive for two identical particles [38], the interaction U_A is therefore always attractive. Two ways to estimate the Hamaker constant for two particles in a given medium exist: one can use $A_{pmp}^{1/2} = A_{pp}^{1/2} - A_{mm}^{1/2}$, where A_{pp} and A_{mm} are the Hamaker constants of the particle and the medium, respectively [38, 62] or use $A_{pmp} = (A_{pp}^2 - A_{mm}^2)^{1/2}$ [52]. Because of retardation effects, equation 2.22 is inaccurate if the particles are too far apart ($R >> a$). However, because of the rapid decrease of the value of this interaction with R, it can be neglected at large distances. A way to suppress the van der Waals interactions is to match the optical indices of the particles and the solvent [38, 67]. It is worthwhile to note that in the case of surfaces with absorbed layers, Equation 2.22 can be written in terms of the different Hamaker constants into play (core particle, polymer layer and solvent medium) [39].

2.5.2 Electric double layer interaction

The screening double layer is a double layer made of counterions and electrolyte ions that surrounds electrically charged particles in aqueous media. The counterions, which have sign opposed to that of the particle charge are drawn toward the particle and a monolayer made of such ions develops immediately near the surface. This monolayer is also called the Stern layer [52]. Outside this layer, the concentration of counterions gradually decreases toward the bulk concentration of the aqueous phase. As two particles approach each other, the overlapping double layers induces long-range repulsive forces due to entropic effects [39]. For two

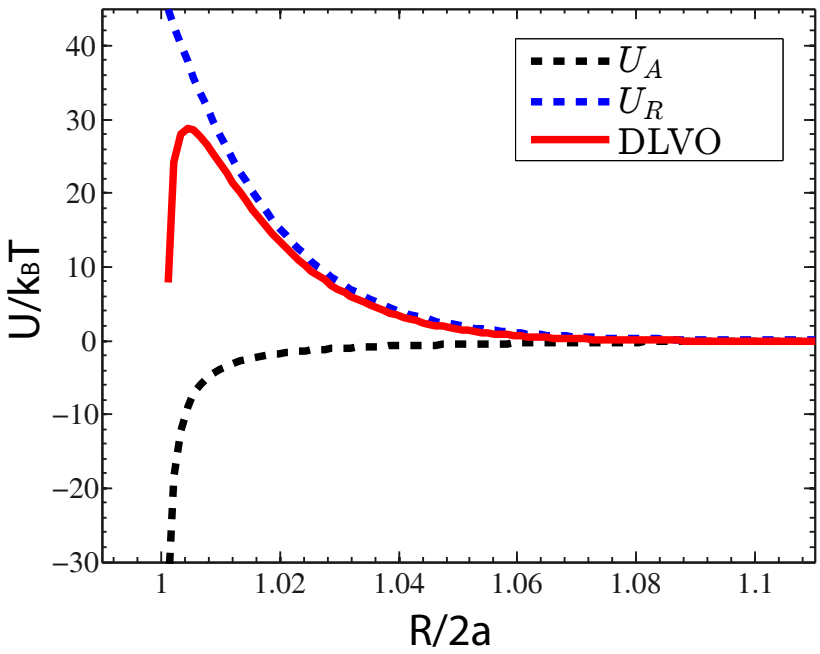

Figure 2.15: Interaction potential for Van der Waals interactions (U_A) and electric double layer interaction (U_R). DLVO is the sum of U_A and U_R. Data for numerical calculations are: Eq (2.22), $A_{pmp} = 4 \times 10^{-21}$ J; Eq (2.23b), $a = 100$ nm, $\Phi_0 = 25$ mV, $\kappa a = 35$, $\epsilon = 7.08 \times 10^{-10}$ C^2/Nm^2, $T = 293$ K.

identical particles with surface potential Φ_0, the repulsive interaction can be put in the form [37]:

$$\begin{aligned} U_R &= 2\pi\epsilon\Phi_0^2 a(2a/R)\exp[-\kappa(R-2a)]; \qquad \kappa a < 5 \\ U_R &= 2\pi\epsilon\Phi_0^2 a \ln\{1+\exp[-\kappa(R-2a)]\}; \qquad \kappa a > 5 \end{aligned} \tag{2.23}$$

where ϵ is the permittivity of the medium and κ is the Debye-Huckel constant, given by

$$\kappa = \left(\frac{e^2 \sum_i n_{oi} z_i^2}{\epsilon k_B T} \right)^{1/2} \tag{2.24}$$

where e is the charge of an electron, n_{oi} is the concentration of ions of type i in the bulk, z_i is the valence of ions of type i, k_B is the Boltzmann constant and T is the absolute temperature. The factor κ has a dimension of 1/length. Its inverse measures the thickness of the double layer, which is determined by the concentration of ions in the aqueous phase. It is therefore often called the Debye screening length [62]. For concentrated systems, it is also required to take into account the charge of counterions that balance the surface charge of the colloidal particles. The inverse of an effective screening length can be written as [67]:

$$\kappa_{eff} = \kappa \left(1 - \frac{3Z\varphi}{8\pi a^3 z(1-\varphi)n_s} \right)^{1/2} \tag{2.25}$$

where n_s is referred to the solvent volume (usually, series suspensions are prepared by diluting a concentrated suspension with the solution used as dialyzate [36, 62]). The second term between brackets represents the contribution of counterions, where Z is the mean number of charges per particle and the factor $(1 - \varphi)$ accounts for the reduced volume available to electrolyte because of the presence of particles. It has to be noticed that the surface potential can be expressed in terms of the surface charge, i.e. $\Phi_0 = Ze/4\pi\epsilon a(1 + \kappa a)$. Thus, the mean number of charge Z is usually taken as an adjustable parameter to fit experimental results [3, 51, 65]. The combination of Equation 2.22 and Equations 2.23 constitutes the DLVO theory for the interaction in charged colloids (see Figure 2.15).

2.5.3 Hydrophilic interaction

In aqueous media, another kind of interaction is the hydration repulsive forces, also called structural forces [40, 62, 78]. This interaction arises from highly hydrophilic surfaces that cause molecular order in the adjacent and neighboring water molecules. This superficial hydration leads to a repulsive force between surfaces [62], with a characteristic length $\lambda \approx 1\,\text{nm}$ [38, 77]. Using the Derjaguin approximation, the interaction energy for spherical particles can be written [37, 38]:

$$U_s = \Delta G_{pwp} \pi a \lambda \exp[-(R - 2a)/\lambda] \tag{2.26}$$

where ΔG_{pwp} is the free energy on interaction between two particles in water. A combination of DLVO and hydration forces (see Figure 2.16) have been used in the literature to interpret measurements of the forces between protein-covered oil droplets [22] and rheology of protein [9, 10] and clay suspensions [23].

2.5.4 Depletion interaction

When macromolecules are added to a colloid suspension, several behaviors can be observed, depending on the net interaction between the particles, the macromolecules and the solvent [37, 38, 62, 67]. If the particles are fully covered by the absorbed polymer, the interaction is mainly repulsive. This will be covered in the next session. In the case of attractive interactions, two mechanisms have been identified: bridging and depletion. If the polymer chains are able to be absorbed onto the particle surfaces, and if there are some free binding sites on the opposite surface, the bridging attraction can occur [38]. This interaction is exponentially decreasing with a characteristic distance of the order of the segment polymer length [44]. If the polymer can not be absorbed, it will be excluded from the surface of the particles. Assuming the particles are large compared with the polymer, attractive particle-particle forces can arise through a mechanism of depletion [37, 38, 67].

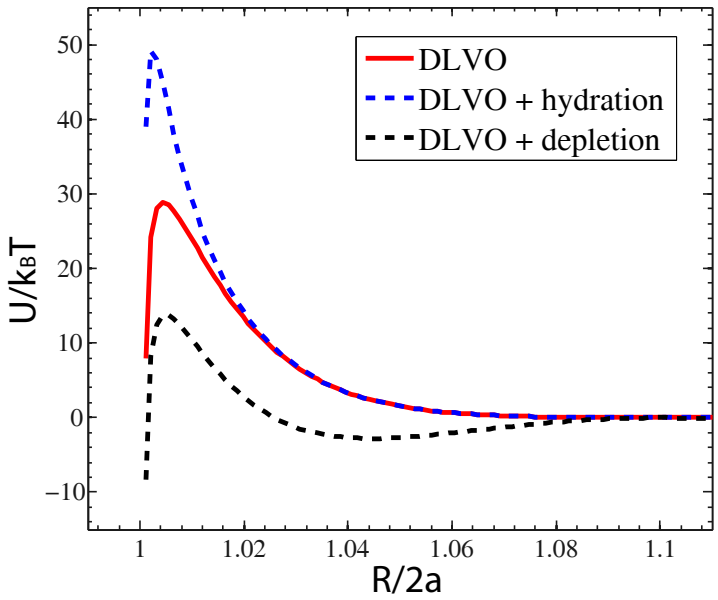

Figure 2.16: Interaction potential for DLVO, hydration and depletion interactions. Data for numerical calculations are: Eq (2.22), $A_{pmp} = 4 \times 10^{-21}$ J; Eq (2.23b), $a =$ 100 nm, $\Phi_0 = 25$ mV, $\kappa a = 35$, $\epsilon = 7.08 \times 10^{-10}$ C^2/Nm^2, $T = 293$ K; Eq (2.26), $\Delta G_{pwp} = 0.5$mJ.m^2, $\lambda = 1$nm; Eq. (2.27), $\Pi = 10^3$Pa, $\delta/a = 0.1$.

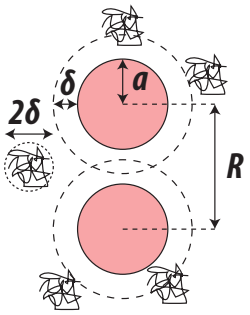

Figure 2.17: Schematic of a pair particles of radius a and with an exclusion radius of δ.

Several approaches have been proposed to explain depletion interaction [42, 62], however one that have been proven useful for different systems is the exclusion volume theory [4]. In this theory, the depleting species are assumed to have an equivalent hard sphere radius δ, and therefore, to be excluded from the gap between particles if $R < 2(a + \delta a)$ as schematically displayed on Figure 2.17. Thus the equivalent hard sphere radius can also be seen as the thickness of a depletion layer surrounding the particles. The resulting difference in osmotic pressures between the depleted zones and the bulk solution leads to an attractive interaction between the particles [62, 71], and can be written as [42, 65]:

$$U_D = \begin{cases} -\frac{4\pi}{3}(a+\delta)^3 \left(1 - \frac{3R}{4(a+\delta)} + \frac{R^3}{16(a+\delta)^3}\right) \Pi; & R < 2(a+\delta) \\ 0; & R \geq 2(a+\delta) \end{cases} \tag{2.27}$$

where Π is the osmotic pressure. The osmotic pressure of the bulk can be expressed as:

$$\Pi = \rho k_B T(1 + 2nM/\rho_m N_A) \tag{2.28}$$

where ρ is the number density of macromolecules, N_A is the Avogadro number, M is the mean molecular weight of polymer and ρ_m its mass density. The first term on the left hand side of this equation is the expression of the osmotic pressure in the case of ideal solutions. The second term arises from the assumption that the depleting species are spherical, so that the second virial coefficient is four times the volume of the macromolecule [35, 71]. It is also suggested that the depletion potential varies with salt concentration when the depleting species are electrostatically charged [12, 55]. Because of the ionic strength dependence of the exclusion thickness, it was suggested to use an effective exclusion radius to take this effect into account [11]:

$$\delta \approx r_g + b\kappa^{-1} \tag{2.29}$$

where r_g is the average gyration radius of the polymer and b is a constant.

2.5.5 Polymer-polymer interaction

When a polymer layer is present on the surface of the particles, independently if it is chemically grafted or absorbed, a repulsive force can be created when the layers of two neighboring particles overlap. If the thickness of the layer is large enough, the van der Waals attraction between the cores is negligible with respect to the Brownian thermal energy. The suspension is thus said to be sterically stabilized [57, 79]. The origin of this interaction is believed to be due to the fact that the overlap of the polymer layers reduces the volume available to each single each, increasing the free energy and hence producing a repulsive force. The affinity between the solvent and the polymer chains governs this kind of interaction [29, 57]. Indeed, the free energy is proportional to $1/2 - \chi$, where χ is the Flory-Huggins parameter. In good solvent, $\chi < 1/2$, meaning the interaction is repulsive, whereas $\chi > 1/2$ in poor solvent, meaning the interaction is attractive. The particle aggregation is then controlled through the value of χ, which varies with the solvent [63], the pH [28] and the temperature [19].

Using the derivation from de Gennes [20], it is possible to have an expression for the interaction energy between polymer-covered flat surfaces which accounts for the osmotic repulsion between polymer layers and the elastic energy of the chains. The interaction decays rapidly with distance, therefore, using the Derjaguin approximation, the interaction potential between spherical particles can be expressed as [11, 81]:

$$U_P = \frac{64\pi a L^2 k_B T}{s^3}\left[\frac{1}{5}\left(\frac{h}{2L}\right)^{-1/4} - \frac{1}{77}\left(\frac{h}{2L}\right)^{11/4} + \frac{3}{35}\left(\frac{h}{2L}\right) - \frac{3}{11}\right] \tag{2.30}$$

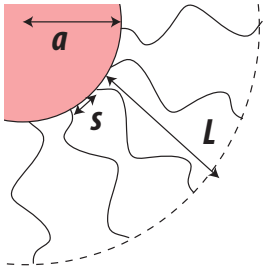

Figure 2.18: Schematic of a particle of radius a with grafted polymer on its surface.

where s is the mean distance between the chain attachment points at the core surface, L is the polymer layer thickness and h is the surface to surface distance between cores, see Figure 2.18. For practical purpose, it has been suggested to use a simplified version of the previous equation, considering that the interaction potential is roughly exponential [38]:

$$U_P = \frac{100aL^2k_BT}{\pi s^3}\exp(-\pi h/L) \tag{2.31}$$

This simplification is valid within the limits corresponding to the very low and very high polymer layer overlapping.

2.6 Aggregated suspensions

It possible in colloidal systems to be in presence of a net attractive potential between particles, leading to particle aggregation [6, 62]. As summed up by Genovese [30], the IUPAC [26] defines the terminology that have to be used when describing an aggregated suspension: a) an aggregate is a group of particles held together in any way, and more specifically, the structure formed by the cohesion of colloidal particles; b) when a sol is colloidally unstable (i.e. the rate of aggregation is not negligible) the formation of aggregates is called flocculation or coagulation; c) these terms are often used interchangeably, but flocculation is preferred for the formation of a loose or open network (called floc) which may or may not separate macroscopically, and coagulation is preferred for the formation of compact aggregates, leading to a macroscopic separation of a coagulum; d) the rate of aggregation is in general determined by the frequency of collisions and the probability of cohesion during collision; e) if the collisions are caused by Brownian motion, the process is called perikinetic aggregation; if it is caused by hydrodynamic motion, the process is called orthokinetic aggregation.

The probability of adhesion is given by the interparticule potential during collision. The combination of attractive and repulsive forces present in many systems produces complex behaviors, where the probability of adhesion, as well as its strength depends on where the particle is situated compared to the different potential wells of the particle's energy profile [30].

In the case of colloidal particles, aggregation typically leads to the formation of highly branched fractal flocs, called clusters. At low particle volume fraction, the clusters are not interconnected, and the suspension remains liquid-like or weakly elastic with no yield stress. In this case, the rheological behaviour is governed by the discrete aggregates. Above the percolation threshold volume

fraction (φ_G) [82], the clusters can be interconnected into a network and the system becomes more solid-like, with a yield stress and an elastic modulus that increase with the volume fraction. Gelation in aggregating colloids occurs when the clusters become crowded [62]. If the adhesion strength is very strong, the fractal type aggregates can join together to produce a large interconnected network. The gelation is then called irreversible. If the adhesion forces are weaker though, the network created can be transient, and will behave more like a weak gel-like solid, thus having viscoelastic properties [21]. The gelation is then called reversible. In practice, many systems fall somewhere between these two situations [30]. Clusters can be seen as fractal objects because of their self similarity and their invariance under a change of scale [48]. The average number of elementary particles in a fractal cluster, N, is related to its average radius, R, and the radius of the monodispersed spherical particles, a, through the equation

$$N \approx \left(\frac{R}{a}\right)^{D_f} \tag{2.32}$$

where D_f if the fractal dimension of the cluster [6, 30, 47, 48, 59, 66, 69]. The fractal dimension reflects the internal structure of the flocs, is proportional to the density of the flocs and depends on the mode of aggregation [66]. In three dimensions, the maximum value D_f can take is 3 (for a system packed like a crystal lattice), and is lower than 3 for more open structures. Known typical values are 1.8 for diffusion limited cluster aggregation (DLCA) and 2.1 for reaction limited cluster aggregation (RLCA) [47, 48]. It has been shown to take even higher values (between 2.1 and 2.7) in the case of orthokinetic aggregation, according to the volume fraction, the aggregate size, the shear experienced and the shear history [7, 58, 72].

Clusters are supposed to behave like spherical objects composed of both the particles and trapped fluid [69]. The aggregation process thus results in an increase in the volume fraction of the discrete phase, compared to its non-aggregated value [48]. To take into account this effect, it is possible to define an effective volume fraction φ_{eff} which links the volume fraction of the non-aggregated particles φ and a packing factor φ^* [59, 69, 80]

$$\varphi_{eff} \approx \varphi\varphi^* \approx \varphi N^{\frac{3}{D_f}-1} \approx \varphi \left(\frac{R}{a}\right)^{3-D_f} \tag{2.33}$$

The viscosity of the aggregated suspension may then be obtained by introducing the effective volume fraction instead of the regular volume fraction. Because the aggregates are bigger than the particles, the effective volume fraction is bigger than the volume fraction of the non-aggregated suspension and thus the viscosity of the aggregated suspension is much higher than the hard-sphere suspension.

The shape and the size of aggregates are closely related to the balance between all the different forces in the system. As discussed earlier, there can be attractive as well as repulsive forces. With shear, aggregates or flocs are broken

down and can be restored under quiescent conditions [30] due to the attractive force field [6, 59, 62, 66, 74]. The structure recovers to a reproducible rest state in a certain amount of time after being sheared, which can allow to control the shear history dependence [66]. Under a given shear condition, the steady state is reached once a balance between breakdown and reformation of the aggregates is established [69]. The aggregates can then reach a maximum stable size, which can be predicted either from the balance between aggregate cohesion and flow related stresses, or from the competition between aggregation and fragmentation dynamics [18]. This steady state size reduces when the shear is increased [69], until the flocs are reduced to single particle again [6]. The viscosity thus decreases for a high zero-shear viscosity to an low infinite-shear viscosity [47, 48, 62, 69].

Several models have been proposed to describe this dependence of the aggregate size with the shear [30]. Wessel and Ball [80] proposed that when the energy of the bending moment applied by shear on the aggregates is more important than the binding energy between the particles, the maximum stable cluster size can be related to the shear stress of the solvent (σ_f), then to the shear rate and the solvent viscosity through

$$R \approx \sigma_f^{-1/3} \approx (\eta_f \dot{\gamma})^{-1/3} \tag{2.34}$$

where η_f is the solvent viscosity. Another approach, found to be more effective, is to consider that the aggregates are surrounded by an effective medium with a viscosity equal to that of the suspension [48, 59, 69]. In this case, the viscosity of the solvent is replaced by the viscosity of the overall suspension. Snabre and Mills [69] then developed a model for fractal aggregates in the case when hydrodynamic effects dominate over Brownian motion

$$R \approx 1 + \left(\frac{\sigma_c}{\sigma}\right)^m \tag{2.35}$$

where σ is the shear stress in the suspension and σ_c is the characteristic stress for the breakup of the aggregates, related to the strength of the particle-particle interactions. It may also be related to the surface adhesive energy per unit contact area (E_a) or to the adhesion force (F_a), defined as the force required to separate the particles [18, 69]

$$\sigma_c \approx \frac{E_a}{a} \approx \frac{F_a}{a^2} \tag{2.36}$$

The exponent m in Equation 2.35 depends on the structure of the aggregates, their mechanism of deformation and breakup under shear as well as the reversibility of the breakup and the aggregation [18, 69]. A weak bounding energy between particles gives rise to soft clusters ($m = 1/2$) which are unable to transmit elastic stresses and thus will be deformed irreversibly and eroded. On the other hand, rigid clusters ($m = 1/3$) can transmit small elastic stresses, which preserves the structure of the rigidly connected particles.

2.7 Conclusion

Rheology of suspension is not a trivial branch of rheology. Many parameters have to be considered, and much is yet to be understood. On the top of the parameters discussed above, more can be added in several types of materials, such as suspensions of biological nature. When ones considers the suspension of living animal cells for example, a part of variability has to be taken into account which is inherent with the biological nature of cells. Moreover, cells are dynamic particles that can bound and therefore communicate with one another. The next chapter therefore quickly describes the basic mechanism of cells, why and how they interact with their surroundings and why understanding the flow behaviour of cell suspensions is required in the development of certain types of processes.

References

[1] A. Acrivos and T.S. Lo. Deformation and breakup of a single slender drop in an extensional flow. *J. Fluid Mech.*, 86:641–672, 1978.

[2] E. Anczurowski and S.G. Mason. The kinetics of flowing dispersions: Iii. equilibrium orientations of rods and discs (experimental). *J. Colloid Interface Sci.*, 23:533–546, 1967.

[3] A.K. Arora and B.V.R. Tata. Interaction, structural order and phase transition in colloidal dispersions. *Adv. Colloid Interface Sci.*, 78:49–97, 1998.

[4] S. Asakura and F. Oosawa. Interaction between particles suspended in solutions of macromolecules. *J. Polym. Sci.*, 33:183–192, 1958.

[5] H.A. Barnes. Shear-thickening (dilatancy) in suspensions of nonaggregating solid particles dispersed in newtonian liquids. *J. Rheol.*, 33:329–366, 1989.

[6] H.A. Barnes. *A handbook of elementary rheology*, chapter 15. the University of Wales Institute of Non-Newtonian Fluid Mechanics, 2000.

[7] G. Barthelmes, S.E. Pratsinis, and H. Buggisch. Particle size distributions and viscosity of suspensions undergoing shear-induced coagulation and fragmentation. *Chem. Eng. Sci.*, 58:2893–2902, 2003.

[8] G.K. Batchelor. The effect of brownian motion on the bulk stress in a suspension of spherical particles. *J. Fluid Mech.*, 83:97–117, 1977.

[9] C.L.A. Berli, J.A. Deiber, and M.C. Anón. Connection between rheological parameters and colloidal interactions of a soy protein suspension. *Food Hydrocolloids*, 13:507–515, 1999.

[10] C.L.A. Berli, J.A. Deiber, and M.C. Anón. Heat-induced phenomena in soy protein suspensions. rheometric data theoretical interpretation. *J. Agric. Food Chem.*, 47:893–900, 1999.

[11] C.L.A. Berli, D. Quemada, and A. Parker. Modemodel the viscosity of depletion flocculated emulsions. *Colloids Surf., A*, 203:11–20, 2002.

[12] J. Bibette, D. Roux, and B. Pouligny. Creaming of emulsions: the role of depletion forces induced by surfactant. *Journal de Physique II*, 2:401–424, 1992.

[13] J.F. Brady. The rheological behavior of concentrated colloidal dispersions. *J. Chem. Phys.*, 99:567–581, 1993.

[14] H. Brenner. Rheology of a dilute suspension of axisymmetric brownian particles. *Int. J. Multiphase Flow*, 1:195–341, 1974.

[15] S. Chien. *Red Cell Rheology*, chapter Principles and Techniques for Assessing Erythrocyte Deformability, pages 71–99. Springer Berlin Heidelberg, 1978.

[16] S. Chien, S. Usami, R.J. Dellenback, and M.I. Gregersen. Shear-dependent deformation of erythrocytes in rheology of human blood. *Am. J. Physiol.*, 219:1, 1970.

[17] J.S. Chong, E.B. Christiansen, and A.D. Baer. Rheology of concentrated suspensions. *J. Appl. Polym. Sci.*, 15:2007–2021, 1971.

[18] A. Chougnet, T. Palermo, A. Audibert, and M. Moan. Rheological behaviour of cement and silica suspensions: Particle aggregation modelling. *Cem. Concr. Res.*, 38:1297–1301, 2008.

[19] M.D. Croucher and T.H. Milkie. Temperature dependence of the shear viscosity of sterically stabilised polymer colloids. *Faraday Discuss. Chem. Soc.*, 76:261–276, 1983.

[20] P.G. de Gennes. Polymers at an interface; a simplified view. *Adv. Colloid Interface Sci.*, 27:189–209, 1987.

[21] E. Dickinson. Structure and rheology of simulated gels formed from aggregated colloidal particles. *J. Colloid Interface Sci.*, 225:2–15, 2000.

[22] T.D. Dimitrova and F. Leal-Calderon. Forces between emulsion droplets stabilized with tween 20 and proteins. *Langmuir*, 15:8813–8821, 1999.

[23] J.D.G. Durán, M.M. Ramos-Tejada, F.J. Arroyo, and F. González-Caballero. Rheological and electrokinetic properties of sodium montmorillonite suspensions. *J. Colloid Interface Sci.*, 229:107–117, 2000.

[24] A. Einstein. On a new determination of molecular dimensions. *Ann. Phys.*, 19:289–306, 1906.

[25] A. Einstein. Correction of my work: a new determination of molecular dimensions. *Ann. Phys.*, 34:591–592, 1911.

[26] D.H. Everett. Manual of symbols and terminology for physicochemical quantities and units. *Pure Appl. Chem.*, 31:577–638, 1972.

[27] R.J. Farris. Prediction of the viscosity of multimodal suspensions from unimodal viscosity data. *Trans. Soc. Rheol.*, 12:281 – 301, 1968.

[28] A. Fernández-Nieves, A. Fernández-Barbero, B. Vincent, and F.J. de las Nieves. Reversible aggregation of soft particles. *Langmuir*, 17:1841–1846, 2001.

[29] P.J. Flory. *Principles of polymer chemistry.* Cornell University Press, 1953.

[30] D.B. Genovese. Shear rheology of hard-sphere, dispersed, and aggregated suspensions, and filler-matrix composites. *Adv. Colloid Interface Sci.*, 172:1–16, 2012.

[31] J.D. Goddard and C. Miller. Nonlinear effects in the rheology of dilute suspensions. *J. Fluid Mech.*, 28:657–673, 1967.

[32] H.L. Goldsmith and S.G. Mason. Particle motions in sheared suspensions xiii. the spin and rotation of disks. *J. Fluid Mech.*, 12:88–96, 1962.

[33] H.L. Goldsmith and S.G. Mason. *Rheology, Volume 4*, chapter Microrheology of Dispersions, page 85. Pergamon: New York, 1967.

[34] J. Happel. Viscosity of suspensions of uniform spheres. *J. Appl. Phys.*, 28:1288–1292, 1957.

[35] P.C. Heimenz. *Principles of colloid and surface chemistry.* Marcel Dekker, Inc, New York, 1986.

[36] F.M. Horn, W. Richtering, J. Bergenholtz, N. Willenbacher, and N.J. Wagner. Hydrodynamic and colloidal interaction in concentrated charge-stabilized polymer dispersion. *J. Colloid Interface Sci.*, 225:166–178, 2000.

[37] R. Hunter. *Foundations of Colloid Science, I.* Clarendon Press, Oxford, 1992.

[38] J. Israelachvili. *Intermolecular and Surface Forces.* Academic Press, London, 1997.

[39] J.N. Israelachvili. The valculation of van der waals dispersion forces between macroscopic bodies. *Proc. R. Soc. Lond. A*, 331:39–55, 1972.

[40] J.N. Israelachvili and H. Wennerström. Role of hydratation and water structure in biological and colloidal interactions. *Nature*, 379:219–225, 1996.

[41] G.B. Jeffrey. The motion of ellipsoidal particles immersed in a viscous fluid. *Proc. R. Soc. Lond. A*, 102:161–179, 1922.

[42] P. Jenkins and M. Snowden. Depletion flocculation in colloidal dispersions. *Adv. Colloid Interface Sci.*, 68:57–96, 1996.

[43] J. Jezek, S. Saic, K. Segeth, and K. Schulmann. Three-dimensional hydrodynamical modelling of viscous flow around a rotating ellipsoidal inclusion. *Comput. Geosci.*, 25:547–558, 1999.

[44] H. Ji, D. Hone, P.A. Pincus, and G. Rossi. Polymer bridging between two parallel plates. *Macromolecules*, 23:698–707, 1990.

[45] D. Jiang. Numerical modeling of the motion of rigid ellipsoidal objects in slow viscous flows: A new approach. *J. Struct. Geol.*, 29:189–200, 2007.

[46] I.M. Krieger. Rheology of monodisperse lattices. *Adv. Colloid Interface Sci.*, 3:111–136, 1972.

[47] I.Y. Ladyzhinskya and N.B. Uriev. Whether or not two types of layer coexist in colloidal gels under shear. *Colloids Surf., A*, 108:13–25, 1996.

[48] R. Lapasin, M. Grassi, and S. Pricl. Rheological modeling of fractal and dense suspensions. *Chem. Eng. J.*, 64:99–106, 1996.

[49] H.M. Laun. Rheological properties of aqueous polymer dispersions. *Angew. Makromol. Chem.*, 123:335–359, 1984.

[50] H.M. Laun, R. Bung, and F. Schmidt. Rheology of extremely shear thickening polymer dispersions (passively viscosity switching fluids). *J. Rheol.*, 35:999–1034, 1991.

[51] H.M. Lindsay and P.M. Chaikin. Elastic properties of colloidal crystals and glasses. *J. Chem. Phys.*, 76:3774–3781, 1982.

[52] C.W. Macosko. *Rheology: principles, measurements and applications*. Wiley-VCH, New York, 1994.

[53] J. Mahanty and B.W. Ninham. *Dispersion Forces*. Academic Press: London, 1976.

[54] J. Mewis. Flow behavior of concentrated suspensions: predictions and measurements. *Int. J. Miner. Process.*, 44-45:17–27, 1996.

[55] O. Mondain-Monval, F. Leal-Calderon, and J. Bibette. Forces between emulsion droplets: Role of surface charges and excess surfactant. *Journal de Physique II*, 6:1313, 1996.

[56] S. Mueller, E.W. Llewellin, and H.M. Mader. The rheology of suspensions of solid particles. *Proc. R. Soc. Lond. A*, 466:1201–1228, 2010.

[57] D.H. Napper. Steric stabilization. *J. Colloid Interface Sci.*, 58:390–407, 1977.

[58] V. Oles. Shear-induced aggregation and breakup of polystyrene latex particles. *J. Colloid Interface Sci.*, 154(2):351–358, 1992.

[59] A.A. Potanin, R. De Rooij, D. Van den Ende, and J. Mellema. Microrheological modeling of weakly aggregated dispersions. *J. Chem. Phys.*, 102:5845–5853, 1995.

[60] D. Quemada. Rheology of concentrated disperse systems and minimum energy dissipation principle - i - viscosity-concentration relationship. *Rheol. Acta*, 16:82–94, 1977.

[61] D. Quemada. Rheological modelling of complex fluids. - i - the concept of effective volume fraction revisited. *Eur. Phys. J. AP*, 1:119–127, 1998.

[62] D. Quemada and C. Berli. Energy of interaction in colloids and its implications in rheological modeling. *Adv. Colloid Interface Sci.*, 98:51–85, 2002.

[63] S.R. Raghavan, J. Hou, G.L. Baker, and S.A. Khan. Colloidal interactions between particles with tethered nonpolar chains dispersed in polar media: direct correlation between dynamic rheology and interaction parameters. *Langmuir*, 16:1066–1077, 2000.

[64] R. Roscoe. On the rheology of a suspension of viscoelastic spheres in a viscous liquid. *J. Fluid Mech.*, 28:273–293, 1967.

[65] W.B. Russel. *The Dynamics of Colloidal Systems*. The University of Wisconsin Press, 1987.

[66] W.B. Russel, D.A. Saville, and W.R. Schowalter. *Colloidal Dispersions*, chapter 14. Cambridge University Press, 1989.

[67] W.B. Russel, D.A. Saville, and W.R. Schowalter. *Colloidal Dispersions, 2nd ed.* Cambridge University Press, 1991.

[68] W.R. Schowalter. *Mechanics of Non-Newtonian Fluids*. Pergamon: Oxford, 1978.

[69] P. Snabre and P. Mills. Rheology of weakly flocculated suspension of rigid particles. *J. Phys. III*, 6:1811–1834, 1996.

[70] P. Snabre and P. Mills. Rheology of concentrated suspensions of viscoelastic particles. *Colloids Surf., A*, 152:79–88, 1999.

[71] P.R. Sperry. A simple quantitative model for the volume restriction flocculation of latex by water-soluble polymers. *J. Colloid Interface Sci.*, 87:375–384, 1982.

[72] P.T. Spicer, S.E. Pratsinis, and M.D. Trennepohl. Coagulation and fragmentation: The variation of shear rate and the time lag for attainment of steady state. *Ind. Eng. Chem. Res.*, 35:3075–3080, 1996.

[73] J.J. Stickel and R.L. Powell. Fluid mechanics and rheology of dense suspensions. *Annu. Rev. Fluid Mech.*, 37:129–149, 2005.

[74] T. Tadros. Application of rheology for assessment and prediction of the long-term physical stability of emulsions. *Adv. Colloid Interface Sci.*, 108-109:227–258, 2004.

[75] G.I. Taylor. The viscosity of a fluid containing small drop of another fluid. *Proc. R. Soc. Lond. A*, 138:41–48, 1932.

[76] B.J. Trevelyan and S.G. Mason. Particle motions in sheared suspensions. i. rotations. *J. Colloid Sci.*, 6:354–367, 1951.

[77] C.J. van Oss. *Interfacial forces in aqueous media*. Marcel Dekker, Inc, New York, 1994.

[78] C.J. van Oss. Hydrophobicity and hydrophilicity of biosurfaces. *Curr. Opin. Colloid Interface Sci.*, 2:503–512, 1997.

[79] B. Vincent. The effect of adsorbed polymers on dispersion stability. *Adv. Colloid Interface Sci.*, 4:193–277, 1974.

[80] R. Wessel and R.C. Ball. Fractal aggregates and gels in shear flow. *Phys. Rev. A*, 46:R3008 – R3011, 1992.

[81] L.R. White. On the deryaguin approximation for the interaction of macrobodies. *J. Colloid Interface Sci.*, 95:286–288, 1983.

[82] Z. Zhou, P.J. Scales, and D.V. Boger. Chemical and physical control of the rheology of concentrated metal oxide suspensions. *Chem. Eng. Sci.*, 56:2901–2920, 2001.

Chapter 3

Cell and tissue engineering

Contents

Résumé du Chapitre

Dans ce chapitre, nous nous focalisons sur la partie biologique de ce projet. Nous revoyons en premier lieu les interactions entre cellules, ainsi que les interactions entre les cellules et la matrice extracellulaire.

La matrice extracellulaire est un composant important de tout tissu. Sa composition est variable en fonction du tissu étudié, de sa fonction et des cellules présentes. Ceci est exploré plus en détail dans la deuxième partie de ce chapitre.

Dans la troisième partie de ce chapitre, nous nous attachons à rapprocher les notions biologiques définies précédemment avec la rhéologie des suspensions. Pour finir, le projet de thèse est situé dans le contexte global applicatif à la production d'anticorps et à l'ingénierie tissulaire.

3.1 Introduction

Cells are the bricks that make up our body. Each organ is composed of a multitude of cells, with different purposes and functions. The development of multicellular organisms as well as their functions require spatial and functional organisation. In order to do that, cells need to be able to communicate with both the surrounding cells and their surroundings. In this chapter, the very basics of cell-cell and cell-matrix interactions are reviewed in order to understand both the difficulties and limits of cell processes and why it is relevant to overcome them.

3.2 Cell-cell and cell-matrix adhesion

One of the key in the development of complex multicellular organisms such as plants and animals are the interactions between two cells as well as the interactions between a cell and the extracellular matrix (ECM). These molecular interactions at the cellular level direct the assembly of distinct tissues and their organization into organs. This complex behaviour would not be possible without the temporally and spatially regulated expression of a wide array of adhesive molecules. Cells in tissues can adhere either directly to one another through specialized membrane proteins called cell-cell adhesion molecules (CAMs) that often cluster into specialized cell junctions, or indirectly through the binding of adhesion receptors in plasma membrane to components of the surrounding ECM, a complex mesh-work of proteins and polysaccharides secreted by cells into spaces between them [18, 25]. These interactions allow the aggregation of cells into tissues, as well as the bilateral transfer of information between the outside and the inside of the cell [11, 16, 17]. This information transfer plays a central role in cell survival, proliferation, migration and differentiation.

3.2.1 Cell-cell adhesion

The main part of CAMs fall into four major families, as depicted in Figure 3.1: the cadherins, immunoglobulin (Ig) superfamily, integrins and selectins [11, 18]. However, other membrane proteins, whose structures do not belong to any of the major families of CAMs also participate in cell-cell adhesion in various tissues. Many CAMs and other adhesion molecules are made of multiple distinct domains, many of which can be found in more than one kind of protein. Some of these domains are responsible for the binding specificity that characterize adhesion molecules.

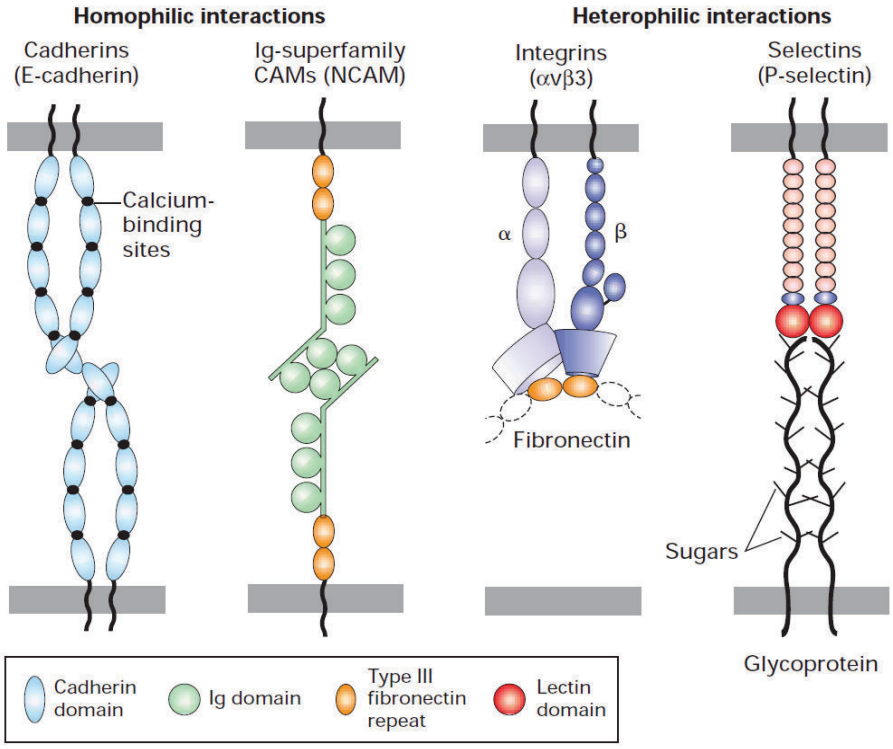

Figure 3.1: The four major families of cell-adhesion molecules and adhesion receptors. From [25].

Two types of adhesion can be identified: interactions between cells of the same type (homotypic adhesion) and interaction between cells of different types (heterotypic adhesion). Two kind of binding can also be identified: the homophilic binding, which describes the binding of a CAM on one cell with the same kind of CAM on an adjacent cell, and the heterophilic binding, which describes the binding of two different class of CAM. CAMs can be broadly distributed along the regions of plasma membranes that connect cells with other cells or clustered in discrete patches called cell junctions. Cell-cell adhesion can be tight and long lasting or relatively weak and transient. Even though it is a stable process, it is not a static one: indeed, the assembly and disassembly of intercellular junctions (during morphogenesis for example) are generally accompanied by dramatic cycloskeletal rearrangements that promotes changes in cell shape and mobility [17].

CAMs are used for information transfer thanks to sets of multifunctional adapter proteins located in the intracellular domain.[11, 18]. These adapters directly or indirectly link the extracellular part of CAMs to elements of the cytoskeleton [18]. They can also recruit intracellular molecules that function as signalling pathways to control protein activity and gene expression. Thus, because cell-cell adhesions are associated with the cytoskeleton and signalling pathways, a cell's surrounding will affect the functional properties and the shape of the cell itself (outside-in effect), as well as cellular function and shape will affect a cell's surrounding (inside-out effect)[15, 37]. Thus connectivity and communication are intimately related properties of cells in tissues, governing cell size, cell shape,

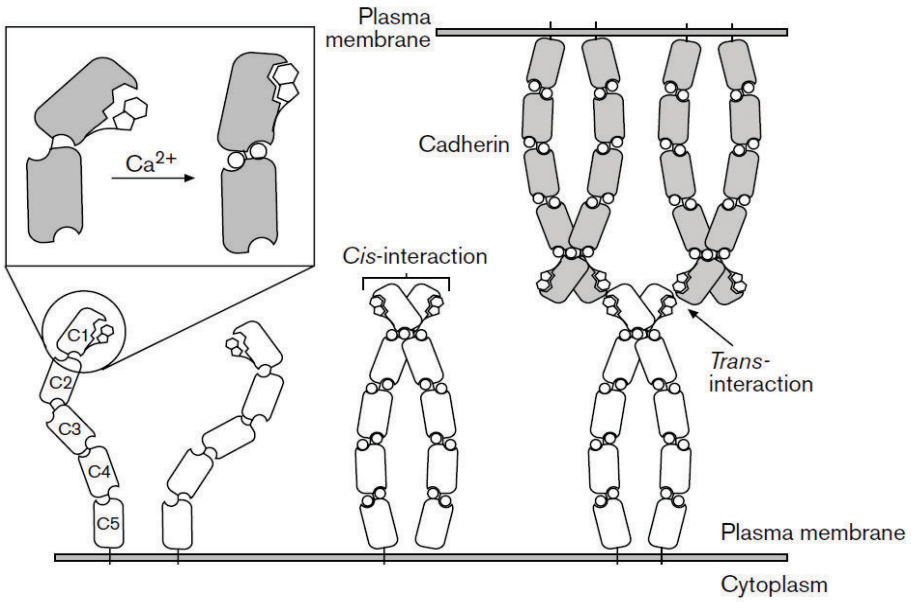

Figure 3.2: Lateral interactions between cell-adhesion molecules within the plasma membrane of a cell form dimers and larger oligomers. Trans interactions between distal domains of cell-adhesion molecules on adjacent cells generate a zipper-like strong adhesion between the cells. From [42].

motility and so on [11, 16].

Two different kind of molecular interactions can be identified when studying the formation of cell-cell adhesions. First, CAMs on one cell associate laterally through their extracellular domains into homodimers or higher-order oligomers in plane with the cell's plasma membrane (intracellular, lateral or cis interactions). Second, CAM oligomers on one cell bind to the same or different CAMs on an adjacent cell (intercellular or trans interactions) [42]. The two cases are schematically shown in Figure 3.2. Adhesive interactions between cells can vary considerably, according to the type and the number of CAMs participating and the tissue. Thanks to this process, very tight adhesions can be generated by combining many weak interactions. Thus the more CAMs are concentrated in small areas, such as cellular junction, the stronger the adhesion force. The intermolecular interactions of CAMs can also be modified by the association of intracellular molecules with the cytosolic domains of CAMS, promoting their cis association. Many properties determine the nature of adhesion between two cells. Among them are thermodynamic properties (binding affinity of the interacting molecules), kinetic properties (overall "on" and "off" rates of association or dissociation for each interacting molecules), ensemble properties (density and spatial distribution of adhesion molecules), biochemical properties (active versus inactive states of CAMs) and mechanical properties (external forces such as stretching and pulling in muscles or laminar and turbulent flow in circulatory systems) [25].

3.2.2 Extracellular matrix role in adhesion

ECM can be seen as a reservoir with components such as proteoglycans, a unique type of glycoprotein; collagens, a protein that often forms fibers; soluble multi-adhesive matrix proteins; and others [11]. Thus components of the ECM can bind both to one another and to certain adhesion receptors located on the cell surface. Through these adhesions, ECM plays an important role in indirect cell adhesion, and so communication [11, 16, 17]. Multi-adhesive matrix proteins such as the proteins fibronectin and laminin are long and flexible molecules that contain multiple domains responsible for binding various types of collagen, other matrix proteins, polysaccharides, cell's surface adhesion receptors and extracellular signalling molecules. These proteins are essential to organize the other components of the ECM, and thus regulate cell-matrix adhesion, and so cell migration and shape [16]. The relative volume of cells versus matrix varies greatly among different tissues. Some connective tissues are mostly matrix, whereas many organs are composed of very densely packed cells with relatively little matrix. On the same basis, the density of packing of the molecules within the ECM itself can vary greatly.

According to the tissue studied, the ECM can have different purposes, such as strengthening in a bone or a tendon or cushioning in cartilage. These different functionalities are tailored by different combination of the extracellular matrix components. The composition of the ECM, which can greatly vary depending on the anatomical site and physiological status of a tissue can provide environmental cues, letting a cell know where it is, and what it should do. Thus, changes in ECM components, which are constantly being remodelled, degraded and re-synthesized locally, can modulate the interactions of a cell with its environment [16]. Once again, the ECM serves as a reservoir for many extracellular signalling molecules that control cell growth and differentiation. In addition, the matrix provides a lattice through or on which cells can move, particularly in the early stages of tissue assembly [16]. Morphogenesis, the stage of embryonic development in which tissues, organs, and body parts are formed thanks to cell movements and rearrangements, is also dependent on cell-matrix adhesion as well as cell-cell adhesion [17]. Disruptions in adhesion are characteristic of various diseases, such as metastatic cancer, in which cancerous cells leave their normal locations and spread throughout the body [25].

3.3 The extracellular matrix

The extracellular matrix helps to organize cells into tissues, and coordinates their cellular functions by activating intracellular pathways that control cell growth, proliferation and gene expression [11, 16, 19, 35]. This can be done thanks to the direct binding of transmembrane adhesion receptors with ECM components. Through adapter proteins, the ECM components then interact with the cytoskeleton of the cells. Several types of molecules function as adhesion receptors, such as integrins.

Adhesion receptors bind to three types of molecules abundant in the extracellular matrix of all tissues. First, the proteoglycans, a group of glycoproteins, cushion cells and bind a wide variety of extracellular molecules [8]. Then are the collagen fibers, which provide structural integrity and mechanical strength and resilience. Finally come several soluble multi-adhesive matrix proteins, such as laminin and fibronectin, which bind to and cross-link cell surface adhesion receptors and other ECM components. [11, 26]

3.3.1 The basal lamina

The basal lamina is the specialized extracellular matrix sheet that plays a major role in determining the overall architecture and function of epithelial tissue. Most organized groups of cells in tissues are underlain or surrounded by the basal lamina, a mesh-work of ECM components usually no more than $60 - 120$ nm thick. According to the studied tissue, the basal lamina is structured in a different way. In epithelial cells, it is a mesh on which only one surface of the cells are resting. In other tissues like muscle or fat, the basal lamina surrounds each cell. Basal lamina also plays an important role in regeneration after tissue damage and in embryonic development, not only for organizing cells into tissues but also for tissue repair and for guiding migrating cells [11]. In the development of the nervous system for example, neurons migrate along ECM pathways that contain basal lamina components. Two distinct basal laminae are employed to form a tight barrier that limits diffusion of molecules between the blood and the brain (blood-brain barrier) [25], and in kidney, where a specialized basal lamina serves as a selective permeability blood filter [2].

Most of the basal lamina components are synthesized by the cells that rest on it. Four protein components are found in basal laminae [13, 26]. First, the type IV collagen, trimeric molecules with both rod-like and globular domains, form a two dimensional network, see Figure 3.3. Then are laminins, a family of multi-adhesive cross-shaped proteins or multi-domain molecules, that form a fibrous two dimensional network with type IV collagen and also bind to integrins and other adhesion receptors. The perlecan, a large domain proteoglycan, binds to and cross-links many ECM components and cell surface molecules. More specifically, proteoglycans consist of membrane-associated or secreted core proteins covalently linked to one or more glycosaminoglycan (GAG) chains, which are linear polymers of sulfated disaccharides [8, 31]. Finally, the nidogen, also called entactin, is a rod-like molecule that cross-links type IV collagen, perlecan and laminin and helps the incorporation of other components in the ECM. Other molecules are also incorporated to the basal lamina depending on the tissue and functional requirements of the basal lamina. Cells directly anchor to basal lamina through cell-surface adhesion receptors, such as integrin, to the mesh-like scaffold. The other side of the basal lamina is anchored to the adjacent connective tissue by a layer of fibers of collagen embedded in a proteoglycan-rich matrix. This anchor layer is called the reticular lamina and is mainly produced by fibroblasts [11]. In the case of skin, for example, this linkage is mediated by anchoring fibrils of type

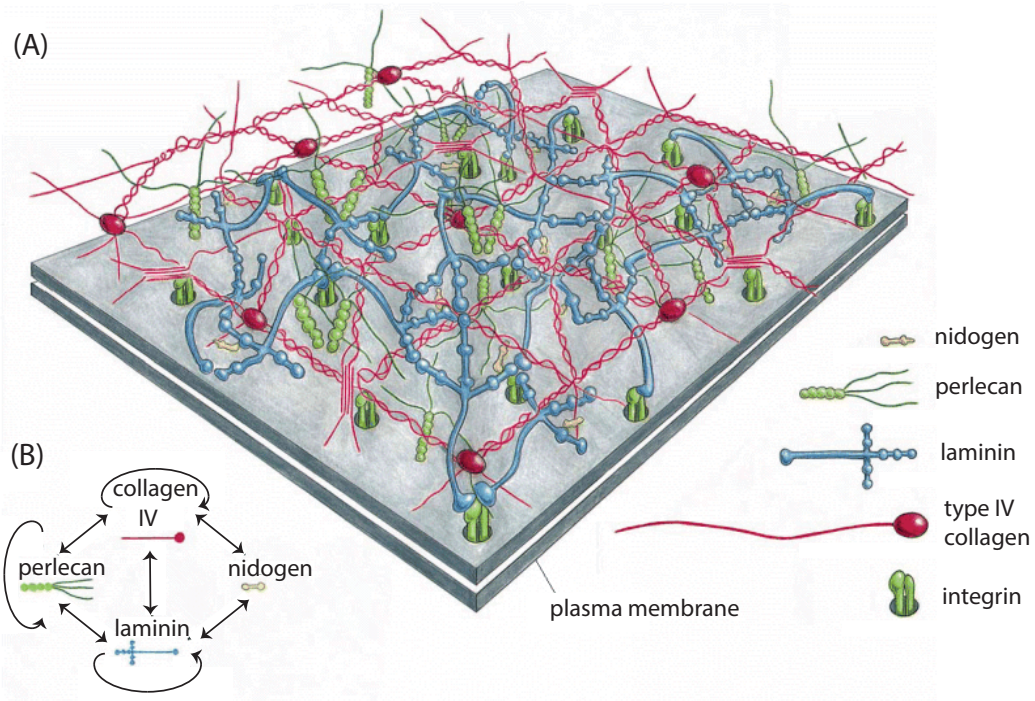

Figure 3.3: (A) Schematic of the two dimensional network formed by the basal lamina through specific interactions (B) between the proteins type IV collagen, laminin, nidogen and the proteoglycan perlcan. Arrows in (B) show molecules that can bind directly to each other. From [1].

VII collagen. The basal lamina and the reticular lamina form the structure called the basement membrane [11].

3.3.2 Non-epithelial tissues

The same or similar molecules mediate and control cell-cell and cell-matrix interactions in nonepithelial tissues (connective, muscle and neural tissues and between blood cells and the surrounding vessels).

Connective tissue, such as tendon and cartilage, differs from other solid tissues in that most of its volume is made up of ECM rather than cells. This matrix is mainly made of insoluble protein fibers and contains proteoglycans, various multi-adhesive proteins and hyaluronate, a very large nonsulfated GAG. The main fibrous protein in connective tissue is collagen. In deformable sites, such as skin, tendons or heart, elastin fibers can be found, which can be stretched and relaxed. A family of multi-adhesive matrix proteins, the fibronectines, form their own distinct fibrils in the ECM of some connective tissues. Several types of cells can be found in connective tissues, however, the various ECM components are largely produced by cells called fibroblasts.

3.3.2.1 Role of collagen

The very large part of the collagen in the body (over 80%) are types I, II and III collagens [38]. They are fibrillar collagens and are mainly located in connective tissues. The type I collagen was the first one to be characterized and consists of a 300 nm long, 1.5 nm thin triple helix made of two α1(I) chains and one α2(I) chain [10, 32, 34]. These molecules then associate into high-order polymer (collagen fibrils), which in turn can aggregate into large bundles (collagen fibers). The other minor classes of collagens include fibril-associated collagens (which link the fibrillar collagens to one another or to other ECM molecules), sheet-forming and anchoring collagens (such as the type IV and VII collagens discussed in the previous section), transmembrane collagens and host defence collagens.

The various collagens are thus distinguished by the ability of their helical and non-helical regions to associate into fibrils, to form sheets or to cross-link other collagen types and therefore to form networks. In tendons, for example, long type I collagen fibrils form thick collagen fibers which can withstand enormous forces. Type I collagen fibers have a great tensile strength, which allows tendons to be stretched without being broken. Indeed, gram for gram, type I collagen is stronger than steel. The addition of other fibrillar collagens regulates the structures and properties of the fibers. Incorporating type V collagen for example results in fibers of smaller diameter.

The fibrils of type II collagen are mainly present in cartilage. They are smaller in diameter than type I fibrils and are oriented randomly in a viscous proteoglycan matrix. The rigid collagen fibrils gives strength and compressibility to the matrix, allowing it to resist large deformations in shape, allowing joints to absorb shocks.

3.3.2.2 Role of hyaluronic acid

Hyaluronan, also called hyaluronic acid (HA) or hyaluronate, is a nonsulfated GAG formed as a disaccharide repeat composed of glucoronic acid and *N*- acetyl-glucosamine by a plasma-membrane-bound enzyme (HA synthase) and is directly secreted into the extracellular space. This means that HA is the structurally most simple GAG, but is not an authentic proteoglycan as it is not covalently associated with protein [31]. It surrounds migrating and proliferating cells, particularly in embryonic tissues [43]. As well as being a major component of the ECM, HA forms the backbone of complex proteoglycan aggregates. These aggregates are found in various ECM, but more particularly in cartilage [43]. HA molecules have remarkable physical properties such as stiffness, resilience or lubricating qualities which made it an important component of connective tissues such as joints. HA covers a wide range of length according to the number of disaccharide repeats (from a few to around $25,000$). In elbow joints for example, typical HA has $10,000$ repeats for a total mass of 4 MDa. This leads to a length of roughly 10 µm. Individual segments of a HA molecule fold into a rodlike conformation. Mutual repulsion between negatively charged carboxylate groups contributes to

these local rigid structure. However, overall, HA is not a long and rigid rod as is fibrillar collagen. Indeed, it is very flexible, bending and twisting into many conformations when in solution, forming a random coil.

HA has a large number of anionic residues on its surface, binding a large amount of water and therefore behaves like a large hydrated sphere with a diameter of roughly 500 nm. At low concentrations, HA can form a hydrated gel. As the concentration increases, the long HA molecules start to entangle, forming a viscous gel. When placed in a confined environment, such as between two cells, the long HA molecules tend to push outward, creating a swelling within the extracellular space. The $COOH^-$ groups on the surface of HA can bind to cations, increasing the concentration of ions and thus the osmotic pressure in the gel. The large amount of water taken up into the matrix contributes to the swelling. These swelling forces give connective tissues their ability to resist compression forces, in contact with collagen fibres, which are able to resist stretching forces.

Several adhesion receptors contain HA-binding domains (such as CD44 or CD168) [43]. These adhesion receptors are present on the surface of many migrating cells and play an important role in cell migration. The loose, hydrated and porous nature of the HA coat on cells keeps them apart from one another, giving them freedom to move about and proliferate. The cessation of cell movement and the initiation of cell-cell attachments are frequently correlated with a decrease in binding between cell and HA, whereas it is because of a decrease in HA, a decrease in HA-binding cell surface molecules or an increase in the extracellular enzyme hyaluronidase (which degrades the HA in the matrix). These functions of HA are important during the many cell migrations that take place in the body, for wound healing, differentiation and the release of a mammalian egg cell (oocyte) from its surrounding cells after ovulation or embryonic development [43].

3.3.2.3 Association of HA and proteoglycans

Proteoglycans can form complex structures. In cartilage for example, the predominant proteoglycan, the aggrecan, assembles with HA into very large aggregates. The aggregate is made from a long molecule of HA to which multiple aggecan molecules are bound tightly but not covalently, see Figure 3.4. A single aggrecan aggregate can be more than 4 µm long, and a volume larger than of a bacterial cell. Thanks to these aggregates, cartilage have unique gel-like properties and can resist to deformations which is essential for distributing the load in weight-bearing joints.

3.4 Link with the rheology of suspensions

As described in Chapter 2, suspensions of particles are complex non-Newtonian fluids. As for any kind of non-Newtonaian fluids, the development of methodologies and processes requires knowledge and understanding of the rheology, to

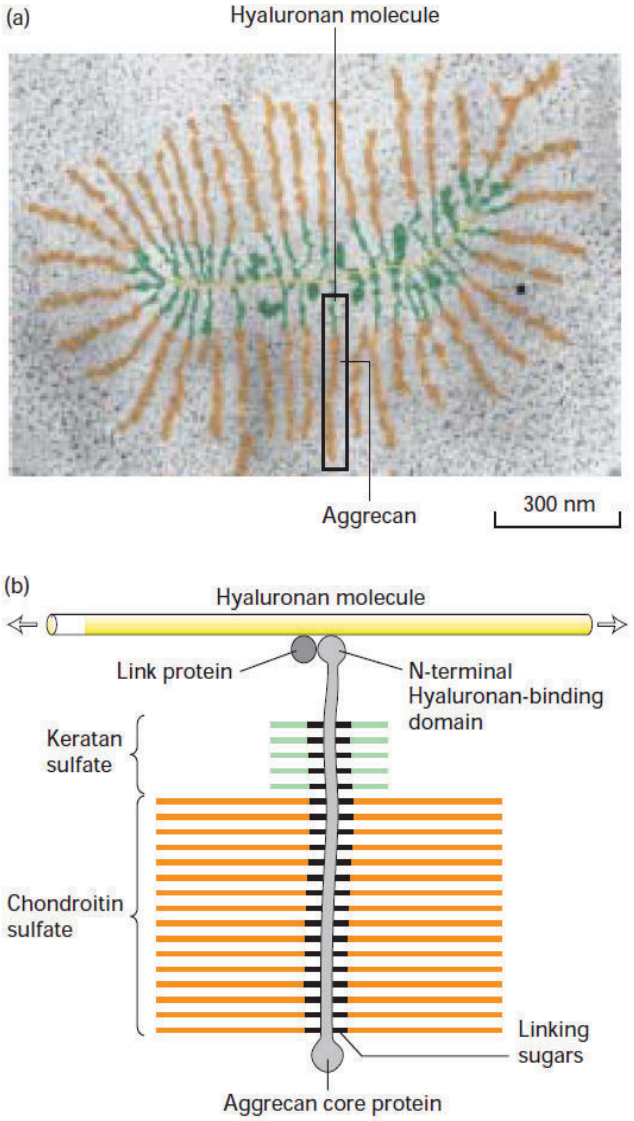

Figure 3.4: (a) Electron micrograph of an aggrecan aggregate from fetal bovine epiphyseal cartilage. (b) Schematic of an aggrecan monomer bound to HA. Image from [25]with the part (a) from [3].

identify the difficulties and eventually, overcome them. This challenge has become of prime importance to bioengineering, bioprocessing and cellular therapies.

3.4.1 Antibody production

Monoclonal antibodies (mAbs) are required for many types of experiments or medical applications [21]. Mammalian cells are used for expression of all commercial therapeutic mAbs, and grown in suspension culture in large bioreactors, ranging from 5000 to 25000 L. Typical production processes run for 7 to 14 days with periodic feeds when nutrients are added to the bioreactor. These fed-batch processes accumulate mAb titers of 1 to 5 g/L, with some companies reporting 10 to 13 g/L for extended culture durations [21]. The antibody purification process is initiated by harvesting the bioreactors using industrial continuous disc stack centrifuges. This is then followed by clarification using depth and membrane filters [21]. Several chromatography steps are then used to capture and purify the mAb [9]. Filtration processes are then used to provide additional viral safety, and then formulate and concentrate the product [39]. The product is then stored frozen or as a liquid, before being shipped to the drug product manufacturing site.

Several steps of mAbs production are linked with fluid processes, and therefore flow has to be controlled. One of these step is the one involving the culture of cells. According to Li et al. [22], having 20 millions cells per mL is seen as an improvement, even though it represents a volume fraction of roughly 8.37% (assuming the cells used have an average radius of 10 µm). This volume fraction is quite small, and might be linked to the difficulties to process non-Newtonian fluids. Moreover, mammalian cells processes are generally considered difficult to scale up due to their sensitivity to physico-chemical conditions. During bioreactor operating condition scale up, agitation and aeration are two important conditions to be scaled up properly to achieve comparable process performance across different scales. Agitation is adjusted to provide sufficient mixing and oxygen mass transfer and is generally scaled using equal specific energy dissipation rate, whereas aeration is modulated for appropriate supply of oxygen and removal of excess CO_2. [22, 44]. In large-scale bioreactors, these parameters need to be selected carefully as agitation-related shear forces, e.g., impeller tip speed and aeration related CO_2 accumulation may increase with scale [22].

Therefore, the knowledge of viscosity, as well as a good understanding of culture performance at different scales, are essential to engineer the different phases in mAb production [20]. Difficulties to establish consistent flow fields within bioreactors and high viscosities of concentrated cell suspensions represent a major limitation to throughput and quality products in mAb production [20].

Better understanding of the flow properties of cell suspensions would allow to improve the process of antibody production. More importantly, the ability to tailor the mechanical properties of such material could drastically improve the flow conditions, the mixing and thus the productivity.

3.4.2 Tissue engineering

Cell biology is a field that have evolved widely in the past few decades, with the appearance of regenerative medicine and tissue engineering. The primary aim of tissue engineering is to restore, maintain, or improve tissue or organ function by implementing a combination of cells, engineering and material methods, together with suitable biochemical and physio-chemical factors. It therefore requires deep understanding of the mechanisms through which cells are able not only to survive, but also proliferate and specialized, whether it is on their own (in vitro) or within an organism (in vivo). However, as most engineering fields, it is necessary to gather different areas of science in order to develop new technologies. The fast development of tissue engineering research is not an exception, as biologists, chemists, bioengineers as well as physicists put their efforts in common to understand and overcome the different existing limitations, and, ultimately, develop new methods, techniques and processes. The use of cells in suspension in tissue engineering implies a need for the understanding and the tailoring of the flow properties of such materials.

3.4.2.1 Example of cell injection challenge: the case of cardiac tissue engineering

The first evidence that cell injection may be a viable therapeutic approach for myocardial infarctions came from the animal studies with injection of fetal or neonatal cardiac myocytes [4]. Cardiac myocytes injection improved left ventricular function and ventricle thickness, thus attenuating pathological remodeling upon myocardial infarctions [14, 23, 27, 33]. Injected cardiac myocytes were demonstrated to integrate through gap junctions and intercalated discs with the host cardiac myocytes [41]. Yet the enthusiasm generated by these studies was hampered when massive death of injected myocytes was demonstrated [28, 45]. Zhang *et al.* [45] intent was to quantify the optimal number of cardiomyocytes to graft into injured heart. They focused on four doses, ranging from 6×10^6 to 25×10^6 cells. Measuring the size of the graft after one week they reached two conclusions. First, the size of the graft is terribly small, ranging from 0.4 to 2.7 % of the ventricle. Second, increasing cell number did not increase the graft size. Even though no quantification of cell survival was not done directly after injection, it indicates that massive cell death occurred. The two conclusions reached by Zhang *et al.* suggest that injection may be a part of the problem. In Muller-Ehmsen *et al.* [28], cell survival was quantify through the DNA ratio between the male DNA and the DNA in the reference samples. Cell survival at 0h and 1h after transplant was $57 \pm 17\%$ and $58 \pm 10\%$. This suggest that most of the cells were already dead when reaching the transplantation site, indicating the injection technique and/or the delivery process may be the issue. To date, optimization of cell delivery has not been systematically examined. Indeed, as mentioned by Muller-Ehmsen *et al.*, the needle diameter, the velocity of injection and the viscosity of cell suspension will affect the forces acting upon the cell membranes. Knowledge of the mechanical properties of such suspension would

therefore allow to design cell injection in order to prevent, or at least reduce cell death.

3.4.2.2 Injectable systems

Another field widely studied in tissue engineering is the design of scaffolds. These scaffolds are used to give cells a three dimensional support and mimic the ECM environment. Introducing the proper cues, they are meant to promote healing and regeneration. In the case of injectable systems, the material is in a liquid form, with the cells suspended in it, and then injected. The material can then be crosslinked in order to provide defined mechanical properties, like in the case of hydrogels (water-swollen polymer network). These scaffolds can be made of natural (animal (e.g. protein) or plant (e.g. polysaccharides) derived) or synthetic polymers.

Injectable systems are used in various areas of tissue engineering, from cardiac to cartilage, or retinal applications. A major advantage of injectable systems is the minimally invasive, catheter-based treatment required to implant them, lowering morbidity and the hospitalization period [7, 24].

The base material of injectable systems is thus cells suspended within a solution of one or several molecules. This cocktail of molecules can be different according to the aimed tissue, the mechanical properties desired... The flow properties of cell suspensions on their own is therefore not sufficient to engineer the process. Indeed, as discussed above, cells are able to sense their environment through a set of surface receptors. It is thus essential to know the flow properties of the material used according to its composition. Moreover, the use of some molecules or some polymers could help to tailor the same flow properties that are usually problematic.

As mentioned above, the scaffolds (and therefore the molecules making up the material) can be either natural or synthetic. A commonly used natural molecule to build hydrogels is hyaluronic acid (HA). As discussed in the previous part, HA is widely present in the body and is one of the most used biopolymer, and also play an important role in wound healing, through inflammation and cell migration regulation [5]. It is thus important to understand how HA, through its interactions with the cells surface receptors, will modify the flow properties of cell suspensions. Even though natural polymers have for some time been highly favored scaffold candidates, as the body, in most cases, does not treat them as foreign materials, synthetic polymers have emerged as alternative candidates for scaffolding materials. This is mainly linked with the high cost, the limited availability as well as poor mechanical properties and batch to batch variations of natural materials [12].

The most commonly used synthetic hydrogel is polyethylene glycol (PEG), which is nontoxic and non-immunogenic [4]. Synthetic hydrogels have the advantage of precisely defined compositions and mechanical properties that are generally easier to tailor. The major drawback coming with very diverse chemistries

and compositions is that biodegradation products may be cytotoxic, depending on a specific hydrogel [30]. Synthetic hydrogels can be blended or covalently modified with natural materials such as proteins and peptides to induce bioactivity [29]. PEG hydrogels are used for a wide range of tissue engineered scaffolds, from cartilage to cardiac applications or even tendons and ligaments [4].

3.5 Conclusion

When we concern ourselves with suspensions of a biological nature, few studies exist, with the published studies being mainly focused on red blood cells, Chinese hamster ovary cells (epithelial in origin) and rat aorta smooth muscle cells [6, 36, 40, 46]. Even though studying the flow behavior of living mesenchymal cell suspensions at semi-dilute and concentrated regimes presents several significant experimental challenges, it has recently become of prime importance to bioengineering, bioprocessing and cellular therapies. The effects of adding macromolecules in the suspensions also have to be studied as most of the applications rely on a combination of both cells and macromolecules. This is essential in removing current processing limits in terms of maximum cell volume fraction in bioreactor-based expansion methodologies and in the development of new encapsulation methods and systems for the culture and the expansion of mesenchymal cells for a multitude of regenerative medicine and cellular therapy applications.

References

[1] B. Alberts, A. Johnson, J. Lewis, M. Raff, K. Roberts, and P. Walter. *Molecular biology of the cell*. New York : Garland Science, 2002.

[2] A. Boutaud, D.B. Borza, O. Bondar, S. Gunwar, K.O.Netze, N. Singh, Y. Ninomiya, Y. Sado, M.E. Noelken, and B.G. Hudson. Type iv collagen of the glomerular basement membrane. *J. Biol. Chem.*, 275:30716–30724, 2000.

[3] J.A. Buckwalter and L. Rosenberg. Structural changes during development in bovine fetal epiphyseal cartilage. *Coll. Relat. Res.*, 3(6):489–504, 1983.

[4] J.A. Burdick and R.L. Mauck, editors. *Biomaterials for Tissue Engineering Applications*. Springer Wien New-York, 2011.

[5] W.Y.J. Chen and G. Abatangelo. Functions of hyaluronan in wound repair. *Wound Repair Regen.*, 7(2):79–89, 1999.

[6] S. Chien, S. Usami, R.J. Dellenback, and M.I. Gregersen. Shear-dependent deformation of erythrocytes in rheology of human blood. *Am. J. Physiol.*, 219:1, 1970.

[7] J. Clouet, C. Vinatier, C. Merceron, M. Pot-vaucel, Y. Maugars, P. Weiss, G. Grimandi, and J. Guicheux. From osteoarthritis treatments to future regenerative therapies for cartilage. *Drug Discovery Today*, 14(19-20):913–925, 2009.

[8] J.D. Esko and U. Lindahl. Molecular diversity of heparan sulfate. *J. Clin. Invest.*, 108:169–173, 2001.

[9] R.L. Fahrner, H.L. Knudsen, C.D. Basey, W. Galan, D. Feuerhelm, and M. Vanderlaan Mand G.S. Blank. Industrial purification of pharmaceutical antibodies: development, operation, and validation of chromatography processes. *Biotechnol. Genet. Eng. Rev.*, 18:301–327, 2001.

[10] R.D.B. Fraser, T.P. MacRae, and E. Suzuki. Chain conformation in the collagen molecule. *J. Mol. Biol.*, 129(3):463 – 481, 1979.

[11] B.M. Gumbiner. Cell adhesion: The molecular basis of tissue architecture and morphogenesis. *Cell*, 84(3):345 – 357, 1996.

[12] H.I. Hadisaputra. *Manufacture and characterization of alginate-PEG hydrogels for tissue engineering applications*. PhD thesis, Department of Chemical Engineering, The University of Queensland, 2007.

[13] E. Hohenester and J. Engel. Domain structure and organisation in extracellular matrix proteins. *Matrix Biol.*, 21(2):115–128, 2002.

[14] H. Huwer, J. Winning, B. Vollmar, C. Welter, C. Löhbach, M.D. Menger, and H.J. Schäfers. Long-term cell survival and hemodynamic improvements after neonatal cardiomyocyte and satellite cell transplantation into healed myocardial cryoinfarcted lesions in rats. *Cell Transplant.*, 12:757–767, 2003.

[15] R.O. Hynes. Integrins: versality, modulation and sigsignal in cell adhesion. *Cell*, 69:11–25, 1992.

[16] R.O. Hynes. Cell adhesion: old and new questions. *Trends Biochem. Sci.*, 24(12):M33 – M37, 1999.

[17] C. Jamora and C. Fuchs. Intercellular adhesion, signalling and the cytoskeleton. *Nat. Cell Biol.*, 4:E101–E108, 2002.

[18] R.L. Juliano. Signal transduction by cell adhesion receptors and the cytoskeleton: Functions of integrins, cadherins, selectins, and immunoglobulin-superfamily members. *Annu. Rev. Pharmacol. Toxicol.*, 42:283–323, 2002.

[19] R.L. Juliano and S. Haskill. Signal transduction from the extracellular matrix. *J. Cell Biol.*, 120:577–585, 1993.

[20] B. Kelley. Very large scale monoclonal antibody purification: the case for conventional unit operations. *Biotechnol. Prog.*, 23:995–1008, 2007.

[21] B. Kelley. Industrialization of mab production technology: The bioprocessing industry at a crossroads. *MAbs.*, 1:443–452, 2009.

[22] F. Li, N. Vijayasankaran, A. Shen, R. Kiss, and A. Amanullah. Cell culture processes for monoclonal antibody production. *MAbs.*, 2:466–477, 2010.

[23] R. Li, Z. Jia, R.D. Weisel, D.A.G. Mickle, J. Zhang, M.K. Mohabeer, V. Rao, and J. Ivanov. Cardiomyocyte transplantation improves heart function. *The Annals of Thoracic Surgery*, 62(3):654 – 661, 1996.

[24] Y. Liu, R. Wang, T.I. Zarembinski, N. Doty, C. Jiang, C. Regatieri, X. Zhang., and J. Young. The application of hyaluronic acid hydrogels to retinal progenitor cell transplantation. *Tissue Eng. Part A*, 19:135–142, 2013.

[25] H. Lodish, A. Berk, P. Matsudaira, C.A. Kaiser, M. Kreiger, M.P. Scott, S.L. Zipursky, and J. Darnell. *Molecular Cell biology.* Scientific American Press N.Y., 2004.

[26] D.F. Mosher, J. Sottile, C. Wu, and J.A. McDonald. Assembly of extracellular matrix. *Curr. Opin. Cell Biol.*, 4(5):810–818, 1992.

[27] J. Müller-Ehmsen, K.L. Peterson, L. Kedes, P. Whittaker J.S. Dow, T.I. Long, P.W. Laird, and R.A. Kloner. Rebuilding a damaged heart: Long-term survival of transplanted neonatal rat cardiomyocytes after myocardial infarction and effect on cardiac function. *Circulation*, 105:1720–1726, 2002.

[28] J. Müller-Ehmsen, P. Whittaker, R.A. Kloner, J.S. Dow, T. Sakoda, T.I. Long, P.W. Laird, and L. Kedes. Survival and development of neonatal rat cardiomyocytes transplanted into adult myocardium. *J. Mol. Cell. Cardiol.*, 34(2):107–116, 2002.

[29] G.D. Nicodemus and S.J. Bryant. Cell encapsulation in biodegradable hydrogels for tissue engineering applications. *Tissue Eng. Part B*, 14:149–165, 2008.

[30] N. Peppas, J. Hilt ., A. Khademhosseini, and R. Langer. Hydrogels in biology and medicine: From molecular principles to bionanotechnology. *Advanced Materials*, 18(11):1345–1360, 2006.

[31] N. Perrimon and M. Bernfield. Cellular functions of proteoglycans - an overview. *Sem. Cell Dev. Biol.*, 12(2):65 – 67, 2001.

[32] G.N. Ramachandran and G. Kartha. Structure of collagen. *Nature*, 174:269–270, 1954.

[33] H. Reinecke, M. Zhang, T. Bartosek, and C.E. Murry. Survival, integration, and differentiation of cardiomyocyte grafts: A study in normal and injured rat hearts. *Circulation*, 100:193–202, 1999.

[34] A. Rich and F.H.C. Crick. The molecular structure of collagen. *J. Mol. Biol.*, 3(5):483 – IN4, 1961.

[35] E. Ruoslahti and J.C. Reed. Anchorage dependence, integrins, and apoptosis. *Cell*, 77(4):477 – 478, 1994.

[36] H. Schmid-Schonbein, R. Wells, and J. Goldstone. Influence of deformability of human red cells upon blood viscosity. *Circ. Res.*, 25:131–143, 1969.

[37] M.A. Schwartz, M.D. Schaller, and M.H. Ginsberg. Integrins: emerging paradigms of signal transduction. *Annu. Rev. Cell Dev. Biol.*, 11:549–599, 1995.

[38] L.M. Shaw and B.R. Olsen. Facit collagens: diverse molecular bridges in extracellular matrices. *Trends Biochem. Sci.*, 16(0):191–194, 1991.

[39] A.A. Shukla, B. Hubbard, T. Tressel, S. Guhan, and D. Lowz. Downstream processing of monoclonal antibodies application of platform approaches. *Journal of Chromatography B*, 848(1):28 – 39, 2007.

[40] P. Snabre and P. Mills. Rheology of weakly flocculated suspension of rigid particles. *J. Phys. III*, 6:1811–1834, 1996.

[41] M.K. Soonpaa, G.Y. Koh, M.G. Klug ., and L.J. Field. Formation of nascent intercalated disks between grafted fetal cardiomyocytes and host myocardium. *Science*, 264(5155):pp. 98–101, 1994.

[42] M.S. Steinberg and P.M. McNutt. Cadherins and their connections: adhesion junctions have broader functions. *Curr. Opin. Cell Biol.*, 11(5):554–560, 1999.

[43] B.P. Toole. Hyaluronan in morphogenesis. *J. Intern. Med.*, 242(1):35–40, 1997.

[44] Z. Xing, B.M. Kenty, Z.J. Li, and S.S. Lee. Scale-up analysis for a cho cell culture process in large-scale bioreactors. *Biotechnol. Bioeng.*, 103(4):733–746, 2009.

[45] M. Zhang, D. Methot, V. Poppa, Ya. Fujio, K. Walsh, and C.E. Murry. Cardiomyocyte grafting for cardiac repair: Graft cell death and anti-death strategies. *J. Mol. Cell. Cardiol.*, 33(5):907–921, 2001.

[46] B.J.H. Zoro, S. Owen, R.A.L. Drake, C. Mason, and M. Hoare. Regenerative medicine bioprocessing: Concentration and behavior of adherent cell suspensions and pastes. *Biotechnology and Bioengineering*, 103(6):1236–1247, 2009.

Chapter 4

Materials and Methods

Contents

Résumé du Chapitre

Dans ce quatrième chapitre, nous nous intéressons aux méthodes expérimentales utilisées dans cette étude pour caractériser la rhéologie de nos suspensions de cellules.

La culture de cellules est une partie importante de ce projet. Elle est décrite en détail dans la première partie de ce chapitre, avec le protocole utilisé pour mesurer la fraction volumique, ainsi que la viabilité des cellules.

La deuxième partie traite des tests rhéométriques effectués pendant ce projet. Le protocole expérimental est détaillé, et comprends notamment une étude des principales causes d'erreur.

Le reste du chapitre est axé sur les techniques utilisées pour caractériser les cellules ainsi que pour imager les systèmes étudiés. L'attention est tout d'abord porté sur le protocole de cytométrie de flux utilisé, puis sur l'imagerie confocal. Enfin la méthode de microscopie bi-photonique ainsi que la méthode de détermination de la dimension fractale des matériaux sont présentées.

4.1 Introduction

In order to carry out this PhD project, several experimental techniques from different science areas had to be used. This comes mainly because of the biological nature of the material studied. In a first part, the different materials and techniques used to grow the cells and prepare the samples are described. Then the protocol used for the rheological characterisation is reviewed, and the main issues linked with it are investigated. The two following sections are focused on the characterisation of the cells surface receptors of interest for this project, through fluorescent active cell sorting (FACS) first, and through confocal imaging next. Last is the characterisation of the structure of the cell suspension at rest, through two-photon microscopy.

4.2 Cell suspension preparation

4.2.1 Cell culture

Adherent NIH-3T3 cells were grown in culture media (Dulbecco's Modified Eagle's Medium (DMEM) high glucose, containing 10% of Fetal Bovine Serum (FBS) (Invitrogen, USA) and 1% of Penicillin/Streptomycin (P/S)), in standard T175 flasks (see Figure4.1).

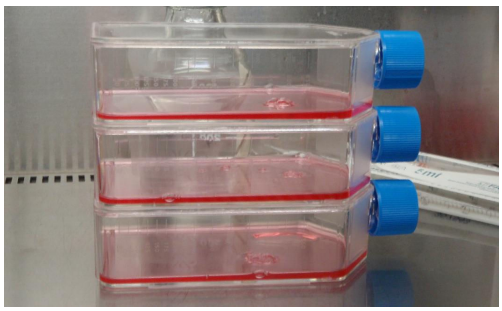

Figure 4.1: T175 flasks.

Once confluency was reached, the cells were passaged. To do so, the media was removed and the attached cells were then washed twice with sterile Phosphate Buffered Saline (PBS) (Amresco, USA). Once the PBS was removed, TrypLE was added. The flask was then incubated for nearly 5 minutes at 37 °C. Once the cells were detached, media was added in order to deactivate the TrypLE solution. The mixture containing cells was then transferred to a 15 mL tube, and centrifuged for 3 minutes at 1400rpm. Two phases were then distinguishable, as shown in Figure 4.2. The top phase is the mix of media and TrypLE, the bottom phase is the cell mixture. The top phase was gently removed, and the cells were re-suspended in fresh media. A fraction of this sample was then transferred in a new flask, with some more media, and

then placed into the 37 °C incubator with 95% air and 5% CO2.

Figure 4.2: 15 mL tube after being centrifuged. The bottom phase is the cell aggregate, the top one is the mixture of media and TrypLE.

4.2.2 Volume fraction measurements

The fraction of the cells and media mixture that was not used for cell passaging was centrifuged again in order to split the cells and the media into two layered phases. The top phase (the supernatant) was removed and the cells were washed twice with PBS, in order to get rid of any trace of FBS. A known quantity of media V_{minit} was then added to re-suspend the cells.

Once the suspension was homogeneous, a hematocrit capillary was plunged into the suspension. The tube was sealed using a piece of PDMS and was centrifuged at 1400rpm for 3 minutes. The cell aggregate height H_c and the total height H_t were then measured thanks to a Vernier calipers (see Figure 4.3). The height of media H_m present in the hematocrit capillary was then calculated, as well as the volume of cells V_{cinit} initially present in the whole suspension.

$$\begin{aligned} H_m &= H_t - H_c \\ V_{cinit} &= V_{minit} \times \frac{H_c}{H_m} \end{aligned} \tag{4.1}$$

In these capillaries, a height of 1 mm equals a volume of 1 µL. Based on the volume of cells left in the suspension after the hematocrit test V_{cfinal}, the correct volume of media needed in the suspension V_{mfinal} according to the required volume fraction φ was then calculated, as well as the volume of media which had to be removed ΔV in order to reach the desired volume fraction φ.

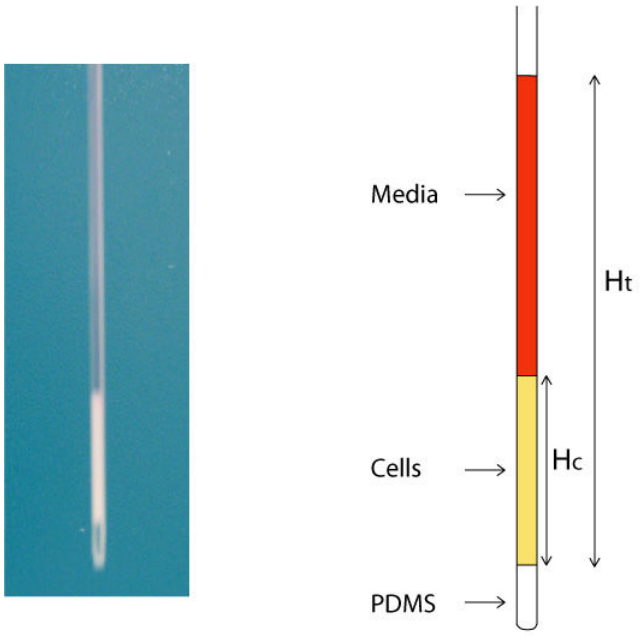

Figure 4.3: Hematocrit capillary after being centrifuged.

$$\begin{aligned} V_{cfinal} &= V_{cinit} - V_c \\ V_{mfinal} &= \frac{V_{cfinal} - \varphi \times V_{cfinal}}{\varphi} \\ \Delta V &= V_{minit} - V_m - V_{mfinal} \end{aligned} \tag{4.2}$$

The suspension was then centrifuged again, in order to remove the volume ΔV of media before being re-suspended.

4.2.3 Cell viability

The rheological experiments performed throughout this study were conducted in different suspending medium, including:

- DMEM high glucose,
- DMEM high glucose with 250 $\mu g \cdot mL^{-1}$ of hyaluronic acid (HA)(Lifecore, Biomedical, USA) of high molecular weight (1.7 MDa),
- DMEM high glucose with 750 $\mu g \cdot mL^{-1}$ of hyaluronic acid (HA) of high molecular weight (1.7 MDa),
- DMEM high glucose with 30 $\mu g \cdot mL^{-1}$ of hyaluronic acid (HA) of low molecular weight (66.3 kDa),
- DMEM high glucose with 750 $\mu g \cdot mL^{-1}$ of hyaluronic acid (HA) of low molecular weight (66.3 kDa),

- DMEM high glucose with 40 $mg \cdot mL^{-1}$ of 8-arms polyethyleneglycole (Jenkem Technology, USA) (40 kDa),
- DMEM high glucose with 40 $mg \cdot mL^{-1}$ of 8-arms polyethyleneglycole-COOH (Jenkem Technology, USA) (40 kDa),
- DMEM high glucose with 40 $mg \cdot mL^{-1}$ of 8-arms polyethyleneglycole-NH2 (Jenkem Technology, USA) (40 kDa).

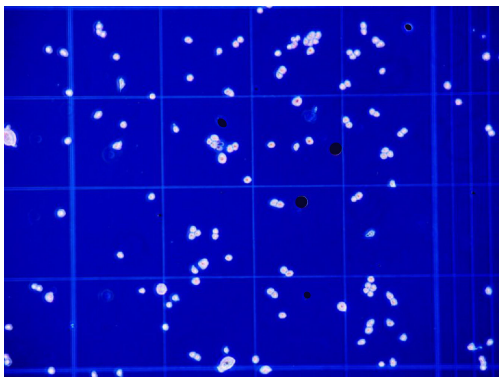

Figure 4.4: Hemocytometer, white dots are live cells and blue dots are dead cells.

We first checked if the cells were able to survive long enough in suspension in these different mediums, at 20 °C to conduct the experiments. The cells viability was measured using a hemocytometer (see Figure 4.4). Living cells and dead cells were counted at different time, up to nearly 3 hours.

The relative total cell number was defined as the ratio between the total number of cells (living and dead) when the count was done and the total number of cells from the first count (at t = 10 minutes). The cell viability was defined as the ratio between the number of living cells and the total number of cells. The results of these counts are shown in the Figures 4.5 and 4.6, confirming that the cells survived in the different suspending fluids long enough to run our experiments.

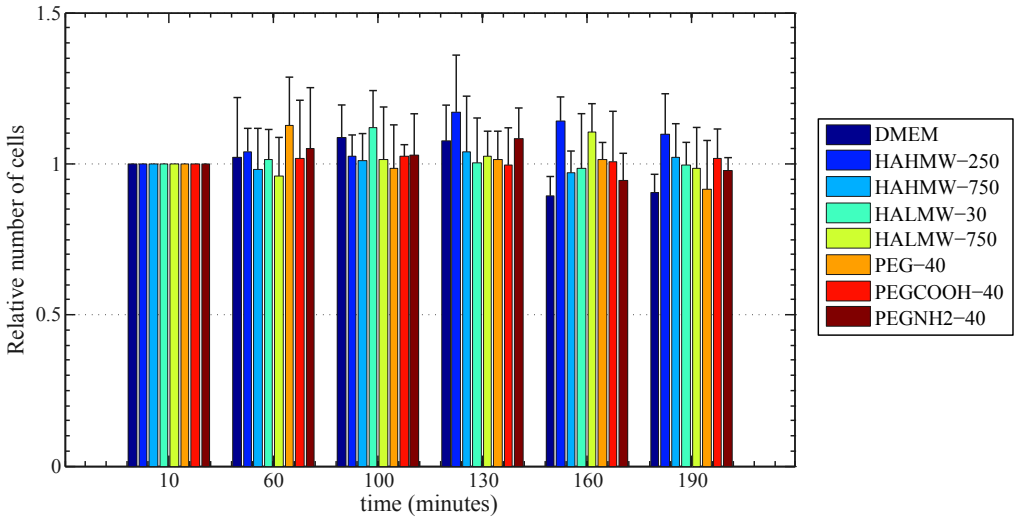

Figure 4.5: Relative total cell number at different time points.

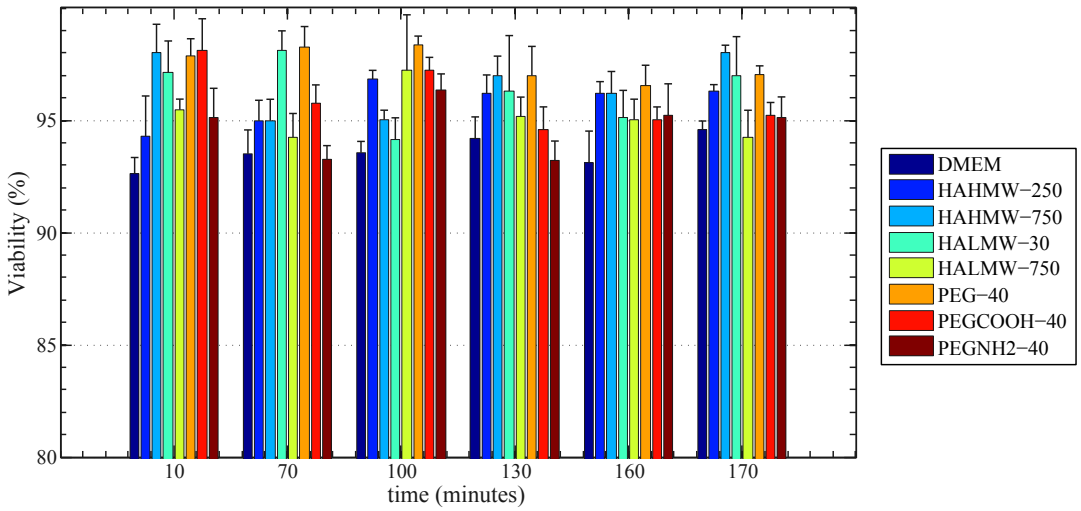

Figure 4.6: Cell viability at different time points.

4.3 Rheology of cell suspensions

4.3.1 Main protocols

The rheological experiments were conducted with a conventional AR-G2 rheometer (TA instruments, USA). Steady shear experiments were controlled in shear stress and conducted at 20 °C. The suspending fluid was tested using a cone-and-plate geometry 60 mm, 1°, however, because of the small volume of material available, the suspension was tested with a plate-plate geometry (20 mm) with small gaps. Issues such as evaporation, sedimentation and slip can arise in such experiments, so several precautions were taken. Due to the suspending fluids being mainly aqueous fluids, a solvent trap was used to prevent evaporation. Cells are not neutrally buoyant particles as there density is approximately 10% higher than the DMEM. Settling of the cells is therefore a phenomenon that has to be taken into consideration. This settling process can be partially counteract thanks to shear induced diffusion which re-suspended the cells [1, 3, 6, 11]. For these reasons, all the shear stresses tested were above 10^{-2}Pa. More over, the time of the experiments was kept small enough in order to ensure that settling was not an issue.

4.3.2 Correcting the gap error

One of the main sources of error when using parallel plates is the gap error, mainly caused by the non-parallelism of the plates. The protocol from Kramer et al. [10] is widely used, and was chosen for our experiments to determine our gap error. The true gap is defined as

$$h = \delta + \epsilon \tag{4.3}$$

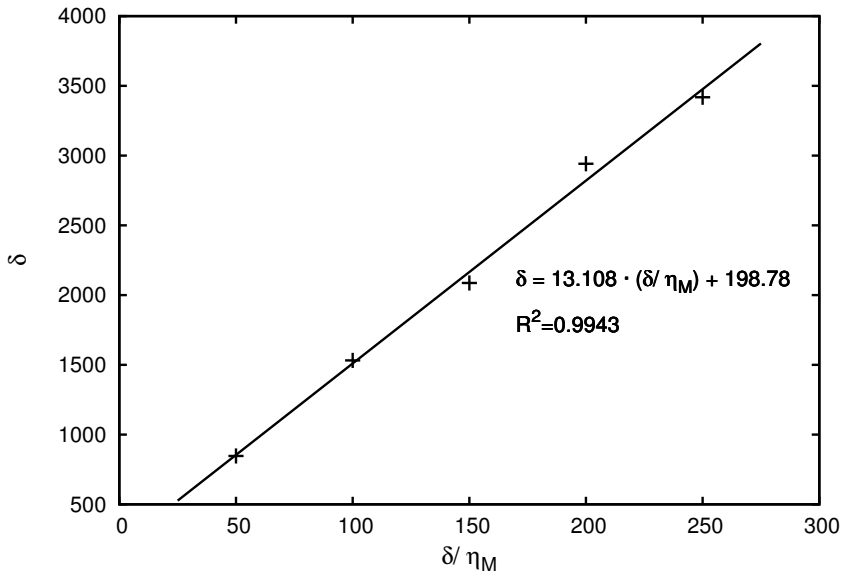

Figure 4.7: Ratio between the commanded gap and the measured viscosity as a function of the measured gap.

where δ is the set (or command) gap and ϵ is the gap error. The actual shear stress is then defined as

$$\sigma = \eta \cdot \dot{\gamma}_R = \eta \frac{\Omega R}{\delta + \epsilon} = \eta \cdot \dot{\gamma_M} \frac{\delta}{\delta + \epsilon} \tag{4.4}$$

By rearranging this expression, it can be found that

$$\frac{\delta}{\eta_M} = \frac{1}{\eta} \times \delta + \frac{\epsilon}{\eta} \tag{4.5}$$

From equation 4.5, it is then possible to deduce the gap error. To do so, the viscosity of a Newtonian fluid (in this case a glycerol solution) is measured at five different gaps. We then plot $\frac{\delta}{\eta_M}$ as a function of the commanded gap.

In the case displayed in Figure 4.7, the gap error was found to be $\epsilon = \frac{198.78}{13.108} = 15$ µm. From there, we can then calculate the corrected viscosity values, as

$$\eta = \eta_M \frac{\delta + \epsilon}{\delta} \tag{4.6}$$

The effect of taking the gap error into account is obvious, as shown in the Figure 4.8: the measured of the viscosity is clearly underestimated at very small gaps. The gap error gap was thus measured before each use of the rheometer with the parallel plate geometry.

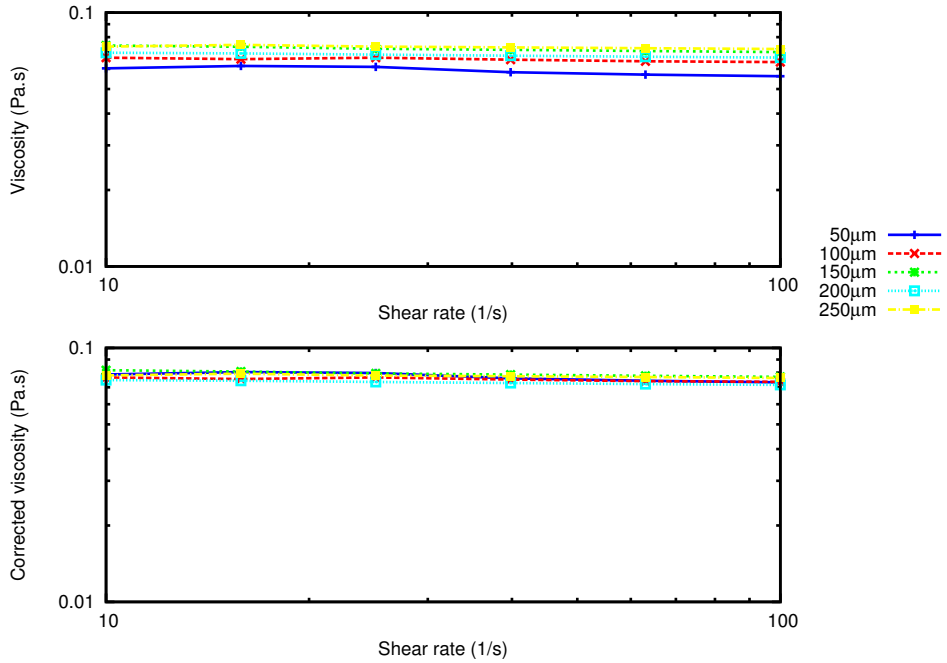

Figure 4.8: Effect of the gap error correction on the measurements of the viscosity as a function of the shear rate for glycerol 80%.

4.3.3 Investigating slippage

In all the equations derived to extract the physical parameters like the shear stress or the shear rate for the different kind of geometry, a major assumption is made: the no-slip condition. This means that the material at the immediate contact of the geometry, whatever the geometry in use, has a velocity equal to that of the plate. In the case of the parallel plate for example, the no-slip condition is verified if the material in contact with the bottom plate has a null velocity and if the part of the fluid in contact with the upper plate has the same velocity as the upper plate, as diplayed schematically by the broken line in Figure 4.9. If not taken into account, the shear rate is thus not estimated properly, nor is the viscosity value.

Yoshimura and Prud'Homme [15] proposed a method to estimate and correct the error linked to slip, assuming the slip velocity is function of the shear stress only. As displayed in Figure 4.9, the velocity of the top disk is $\Omega \cdot r$, and so

$$\Omega \cdot r = H\dot{\gamma}(\sigma_{z\theta}) + 2U_S(\sigma_{z\theta}) \tag{4.7}$$

where $\dot{\gamma}$ is the shear rate experienced by the fluid. Defining the apparent shear rate $\dot{\gamma}_a$ as the velocity of the upper plate divided by the gap height

$$\dot{\gamma}_a = \frac{\Omega \cdot r}{H} \tag{4.8}$$

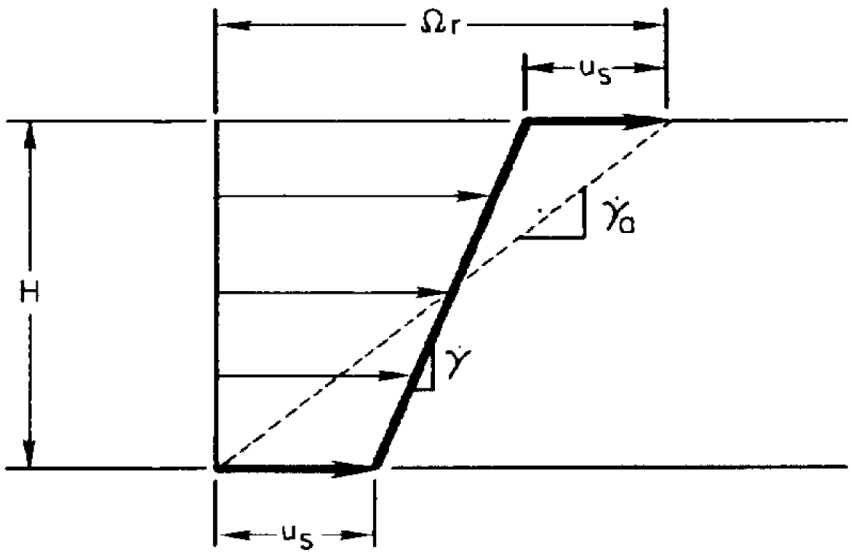

Figure 4.9: Parallel disk velocity field at any particular radius r. The wall slip velocity U_S is the same at each wall. Also shown are the actual shear rate in the fluid $\dot{\gamma}$ and the apparent shear rate $\dot{\gamma}_0$. From [15].

Equation 4.7 can then be rewritten as

$$\dot{\gamma}_a = \dot{\gamma}(\sigma_{z\theta}) + \frac{2U_S(\sigma_{z\theta})}{H} \tag{4.9}$$

In order to verify the no-slip assumption, and if there is slippage, to quantify it, tests had to be carried out at a given shear stress σ_R at two different gap heights H_1 and H_2. The two apparent shear rates at the rim of the upper plate are defined as

$$\begin{aligned} \dot{\gamma}_{aR1} &= \dot{\gamma}_{aR1}(\sigma_R) \\ \dot{\gamma}_{aR2} &= \dot{\gamma}_{aR2}(\sigma_R) \end{aligned} \tag{4.10}$$

Using equation 4.9, it can be written that

$$\begin{aligned} \dot{\gamma}_{aR1}(\sigma_R) &= \dot{\gamma}_R(\sigma_R) + \frac{2U_S(\sigma_R)}{H_1} \\ \dot{\gamma}_{aR2}(\sigma_R) &= \dot{\gamma}_R(\sigma_R) + \frac{2U_S(\sigma_R)}{H_2} \end{aligned} \tag{4.11}$$

Since the slip velocity was assumed to be a function of the shear stress only, $U_S(\sigma_R)$ is the same for each gap height at a given σ_R, thus

$$\dot{\gamma}_{aR1}(\sigma_R) = \frac{H_1\dot{\gamma}_{aR1}(\sigma_R) - H_2\dot{\gamma}_{aR2}(\sigma_R)}{H_1 - H_2} \tag{4.12}$$

Once the corrected shear rate calculated, it is possible to calculate the corrected viscosity value

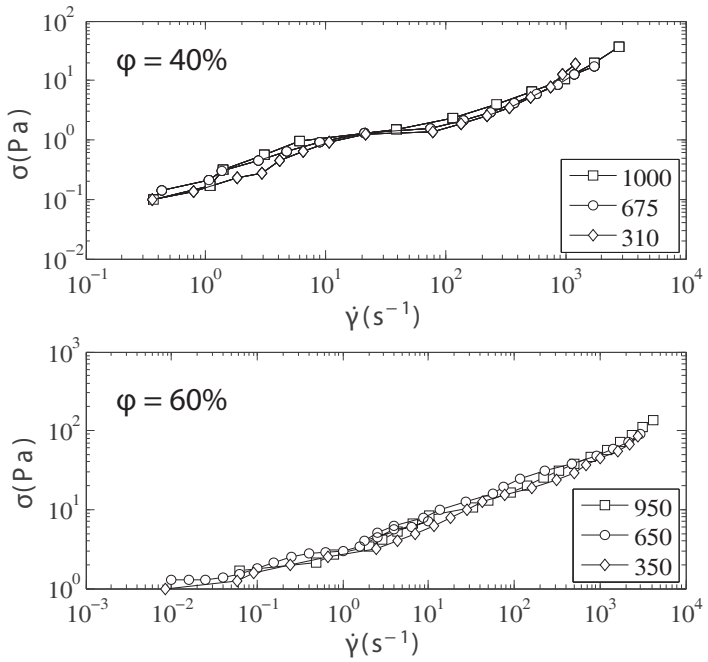

Figure 4.10: Shear stress as a function of shear rate for three different gap heights (in μm) at two volume fractions φ in DMEM. No slip was measured using this method.

$$\eta(\dot{\gamma}_R) = \frac{\sigma_R}{\dot{\gamma}_R} = \frac{\sigma_R(H_1 - H_2)}{H_1\dot{\gamma}_{aR1}(\sigma_R) - H_2\dot{\gamma}_{aR2}(\sigma_R)} \tag{4.13}$$

The slip velocity can also be determined:

$$U_S(\sigma_R) = \frac{\dot{\gamma}_{aR1}(\sigma_R) - \dot{\gamma}_{aR2}(\sigma_R)}{2\left(\frac{1}{H_1} - \frac{1}{H_2}\right)} \tag{4.14}$$

For our system, two volume fractions were tested at three different gap heights. No slip was measured as displayed by the superposition of the different curves in Figure 4.10.

4.3.4 Investigating the influence of the air-liquid interface

The interface between the fluid and the air at the rim of the parallel plate system can influence the measurements. This is also called the edge effect. Edge effects can have two very different origins. The first one is linked to the loading technique. If too much sample is loaded between the parallel plates, the excess sample has to be removed as it can produce a torque offset [9]. If not enough sample is loaded, on the other hand, it is as if a plate or a cone of a smaller diameter was used, resulting in errors when estimating the shear rate and the shear stress. The only way to prevent this is to ensure that the sample is loaded properly and that the gap used is consistent with the volume in use. The second one is

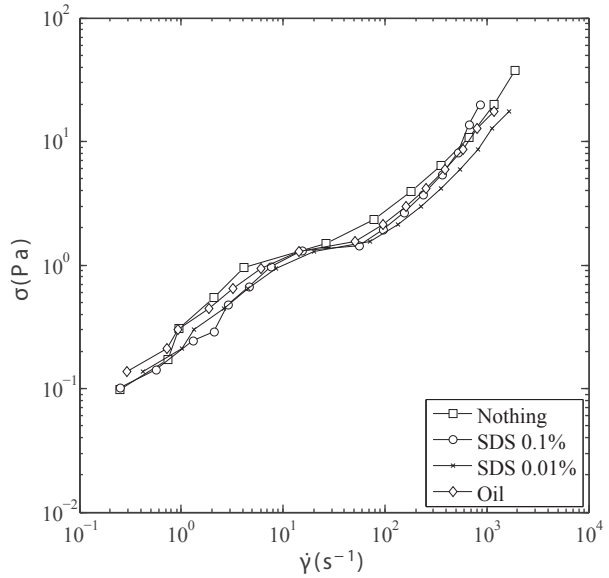

Figure 4.11: Shear stress as a function of shear rate for different rim treatment, at a volume fraction of 40%.

linked with the surface tension of the material. In some materials, like saliva, interfacial elasticity can arise from the absorption of proteins to the air-liquid interface [14]. This elasticity can then influence the measurement of the bulk material properties. A common way to prevent this is to apply a very dilute solution of sodium dodecyl sulfate (SDS), typically at 0.1%, at the rim of the plates. The molecules from this surfactant solution preferentially absorb to the interface in place of proteins, thus lowering the surface tension and the surface elasticity, without impacting on the bulk rheology [14].

SDS is known to be toxic for the cells at high concentrations [7], so two solutions of PBS were prepared, with 0.1% and 0.01% of SDS, respectively. Four tests were then performed, following the protocol described earlier (see 4.3.1): one without anything at the rim of the plates, one with each of the SDS solutions and one with some low viscosity silicone oil.

As can be seen in Figure 4.11, the different edge treatments do not seem to influence the measurements further than the variability inherent to systems of biological nature. This also confirms that the procedure used for the loading is reproducible, without under- or over-loading.

4.3.5 Oscillatory tests

Various oscillatory tests were carried out on the suspension. However, due to the lack of repeatability of the results, the data are not shown in this thesis. Several reasons can be thought of to explain this lack of reproducibility, and despite the time and effort we put into it, we were not able to fix the measurements. First could be the lack of control of the initial state of the suspension: the suspension

was pipetted in order to be homogenized before testing, and even if this procedure was as standardized as possible, it was difficult to ensure the exact same deformation history between all the tests. This was prevented during the flow experiments through the imposition of a constant stress until the steady state was reached. Second, and related, is the sensitivity of the aggregates to the shear. The network created between the cells seem to be quite fragile, so to be probed properly, low amplitude oscillation should have been used, and because of the small geometry used, the measured signal was very noisy. Last, sedimentation could also have played an important role. Indeed, without the imposition of a constant stress high enough to ensure shear induced resuspension, the cells most probably were settling.

4.4 Fluorescence activated cell sorting: FACS

Immunocytochemical staining is accomplished with antibodies that recognize a targeted protein. Since monoclonal antibodies are highly specific, the antibody only binds to the protein of interest. The binding is then visualized using fluorescence detection, in which a fluorochrome is conjugated to the antibody and can be visualized using fluorescence microscopy.

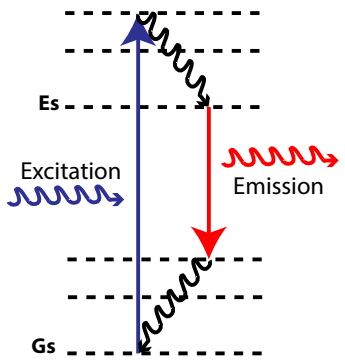

Figure 4.12: Energy level diagram of the excitation of a single dye.

Fluorochromes have unique and characteristic spectra of absorption (excitation) and emission. A single dye, conjugated to the antibody of interest, is excited at a particular wavelength thanks to a light source (mercury lamp for standard immunocytochemical staining or laser for fluorescence activated cell sorting (FACS)). The lamp provides electromagnetic energy to an electron in that molecule, which moves to an excitation state at the next energy level E_s. The energy is then released in the form of a photon, causing fluorescence, and the electron moves back down to the lower energy level G_s (see Figure 4.12). In this case, two sets of antibodies were used: the first set binds to the desired receptor (CD44 and CD168), while the second set, conjugated with a fluorescent dye, binds to the first antibody.

The cells were labelled using rat anti-mouse CD44 (Sigma-Aldrich, USA) and rabbit anti-mouse CD168 (Abcam, UK) primary antibodies and anti-rat Alexa Fluor 488 and anti-rabbit Alexa Fluor 647 (Invitrogen, USA) secondary antibodies.

Flow cytometry is a widely used method for analyzing expression of cell surface and intracellular molecules, characterizing and defining cell types in heterogeneous cell populations, assessing the purity of isolated subpopulations, and

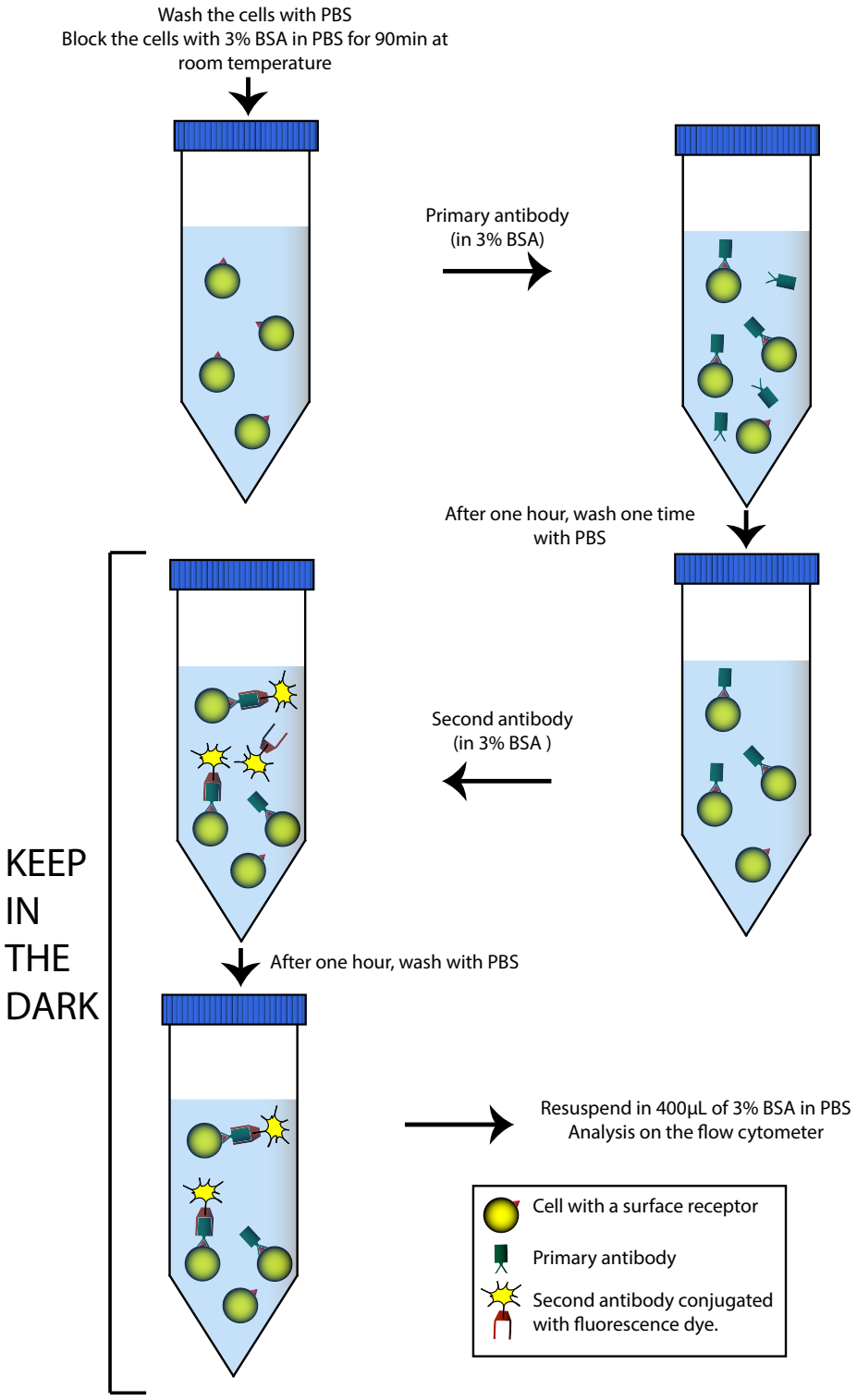

Figure 4.13: FACS protocol, using αCD44 as primary antibody and αmouse IgG-488 as secondary antibody.

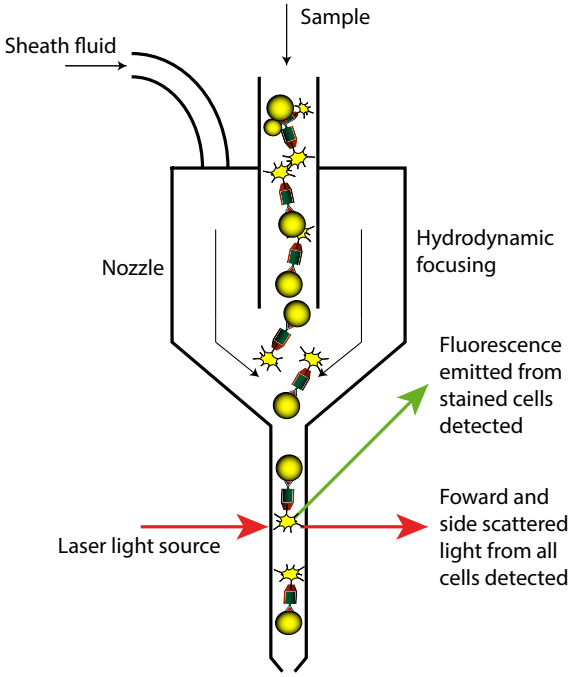

Figure 4.14: Schematic of a flow cytometer.

analyzing cell size and volume. It allows simultaneous multi parameter analysis of single cells. It is predominantly used to measure fluorescence intensity produced by fluorescently labelled antibodies. The staining involves making a single cell suspension from cell culture sample, see Figure 4.13.

When the stained cell sample in suspension buffer is run through the cytometer, it is hydrodynamically focused through a very small nozzle (Figure 4.14). The tiny stream of fluid takes the cells past the laser light one cell at the time. There are a several detectors to detect the light scattered from the cells as they go through the beam. There is one in front of the light stream (Forward Scatter or FSC) and a number on the side (Side Scatter or SSC). Fluorescent detectors are used for the detection of fluorochromes themselves.

4.5 Confocal imaging

4.5.1 Labelling HA

An amount of HA was firstly labelled with a fluorescent dye in order to visualize and to confirm the binding of the HA with the surface of the cells. A known quantity of HA was dissolved in 0.1M 2-(N-morpholino)ethanesulfonic acid (MES) buffer. 1-Ethyl-3-[3-dimethylaminopropyl]carbodiimide hydrochloride (EDC) and N-hydroxysulfosuccinimide (Sulfo-NHS) were also dissolved in a similar buffer in a stochastic ratio of 1:1:1 with the acid groups of HA. EDC is a zero-length crosslinking agent used to couple carboxyl groups to primary amines, which, in

the presence of Sulfo-NHS can be used to convert carboxyl groups to amine-reactive Sulfo-NHS esters. The two solutions were mixed together and stirred for several minutes. Amino FluoProbes® 547H (FluoProbes®, Interchim, France) was then dissolved in a similar buffer and then added to the mixture. The pH was measured after each step. The reaction was left overnight, protected from the light. The sample was then dialysed for 48h in water. The product after dialysis was freeze-dried, before behind dissolved in DMEM at the desired HA concentrations.

4.5.2 Imaging

The labelled HA was then used according to the protocol defined in 4.2. The suspension was let to react at 37 °C for 20 minutes. A washing step was then added in order to remove any trace of labelled HA that was not bound to the cells. High resolution images were obtained using an LSR710 confocal microscope (Zeiss).

4.6 Two-photon microscopy

Two-photon microscopy was invented by Denk *et al.* [4] and revolutionized three dimensional *in vivo* imaging of cells and tissues.

4.6.1 Description of two-photon microscopy

In order to visualise the structure of the cell suspension at rest, a two-photon microscope was used. Regular fluorescence based techniques use a photon to excite a fluorescent molecule (fluorophore) that will emit another photon of different wavelength. Two-photon microscopy is different in the way that the dye has to be hit simultaneously by two exciting photons in order to reach the next electronic excited state, see Figure 4.15.

The probability of two-photon absorption by a fluorescent molecule is a quadratic function of the excitation radiance. The excitation therefore has to be intense in order for the event to happen. This can induce photodamage in the sample and photobleaching of the imaged area. These considerations in mind, two-photon microscopy has several advantages, and the one of interest to us is linked to the very nature of our material. Indeed, concentrated suspensions are highly dispersive, and therefore it is quite a challenge to image them, with a large enough depth to have relevant information. Two-photon microscopy allows us to image such systems because of the low probability of two photons being absorb far from the focal volume (see Figure 4.16). Thus, only the focal volume is emitting light, not the entire depth. This allows to image within opaque materials such as concentrated cell suspensions.

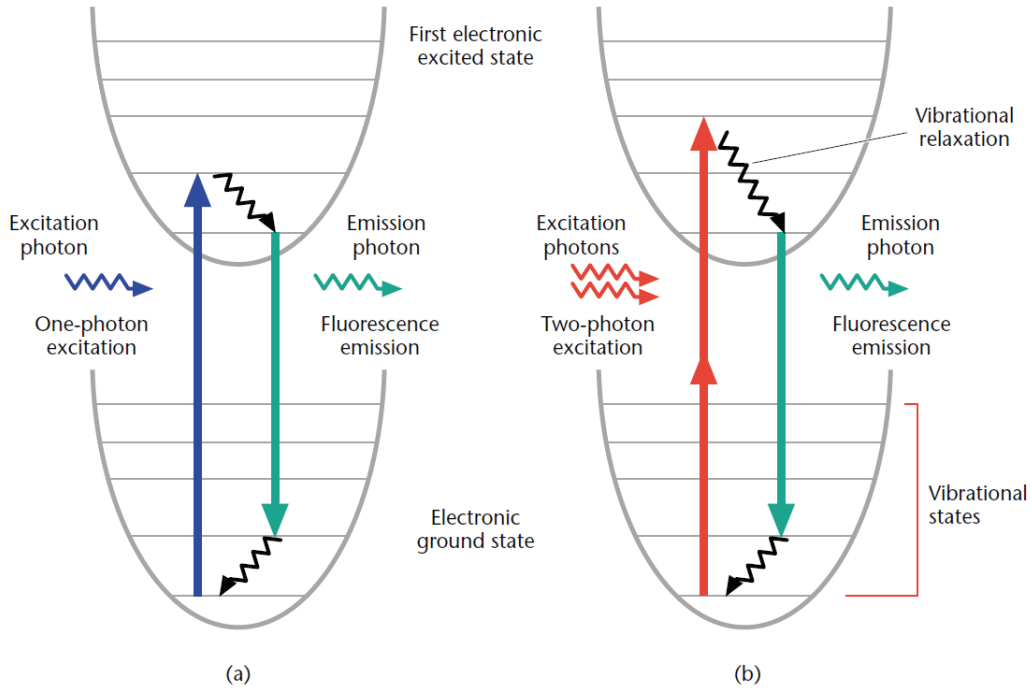

Figure 4.15: Jablonski diagram of one-photon (a) and two-photon (b) excitation. From [13].

Figure 4.16: An experiment to illustrate the difference between ordinary (single-photon) excitation and two-photon excitation (see arrow). From [12], image credit: Brad Amos/Science Photo Library, London.

4.6.2 Sample preparation

After washing with PBS, the cells were re-suspended in a known volume of PBS with 1:1000 Hoechst (Invitrogen), and left in the incubator, at 37 °C for 30 minutes. Hoechst stains are part of a family of blue fluorescent dyes used to stain DNA, and therefore are used to detect the nucleus of the cells. The cells were then centrifuged and the volume fraction was determined and corrected as explained in 4.2.2. A certain amount of supernatant was then removed and a solution of 8 mM of SulfoRhodamine B (SRB) added to a final concentration of 800 µM, while maintaining the volume fraction. SRB or kiton red ($C_27H_30N_2O_7S_2$) is a fluorescent, red, solid, water-soluble dye used for the laser-induced fluorescence quantification of cellular proteins of cultured cells. Cells are impermeable to SRB, and thus allowed us to neatly detect the cells in the suspension. A two-photon microscope was then used in order to take pictures of the suspension at several heights in order to have a 3D representation of the suspension.

4.6.3 Image acquisition protocol

A small volume of the cell suspension was then gently pipetted between two glass slide, with 200 µm spacers on each side. Images were taken immediately after. The laser's wavelength was set to 940 nm, as it seemed to be the best compromise to detect both the SRB and the Hoescht staining.

4.6.4 Image treatment

At least five pictures were taken at every height at the exact same spot for each acquisition channel (one for the SRB and one for the Hoescht staining). Using ImageJ software[1], these images were averaged in order to gain contrast and clarity (see Figures 4.17 and 4.18).

A pseudo flat-field filter (using a Gaussian blur) was then used to gain clarity at the edge of the image (see Figure 4.19).

The minimum and the maximum of the brightness and contrast were then set according to the histogram of the filtered image see Figure 4.20, before converting it to binary, see Figure 4.21. Each image was then checked thoroughly to ensure the absence of artefact as well as the fidelity of the conversion.

The ImageJ's plugin "3D viewer" can also be used to create 3D representation of our material, see Figure 4.22.

[1]Rasband, WS. ImageJ. U.S. National Institutes of Health; Bethesda, Maryland, USA: 2009. Available: http://rsb.info.nih.gov/ij/

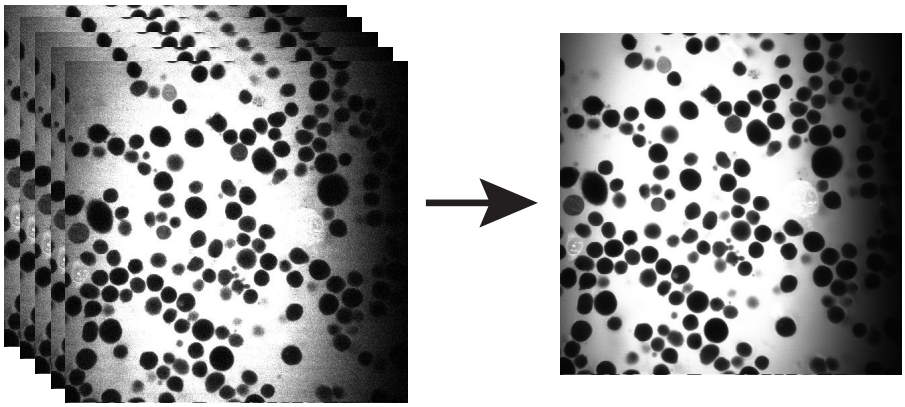

Figure 4.17: At least five images taken at the exact same spot and at the exact same height were averaged for the SRB channel.

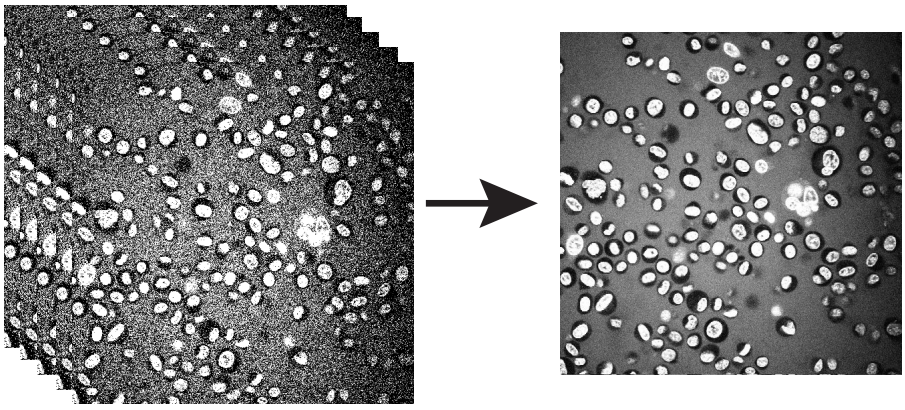

Figure 4.18: At least five images taken at the exact same spot and at the exact same height were averaged for the Hoescht channel.

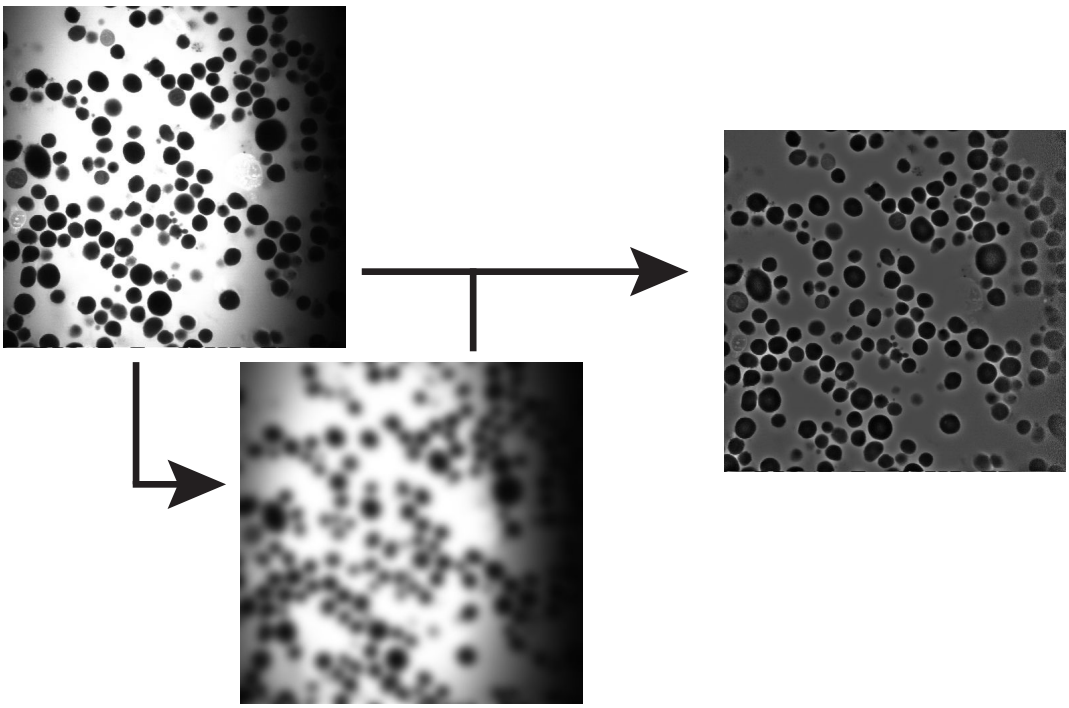

Figure 4.19: A pseudo flat-field filter (using a Gaussian blur) was used to gain clarity at the edge of the image

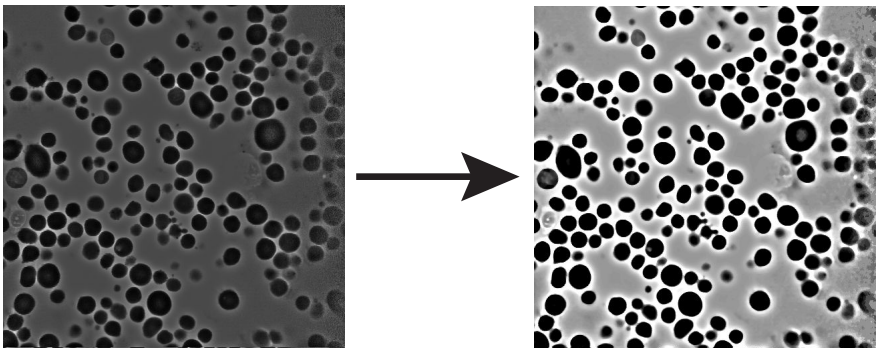

Figure 4.20: The minimum and the maximum of the brightness and contrast were then setted according to the histogram of the filtered image.

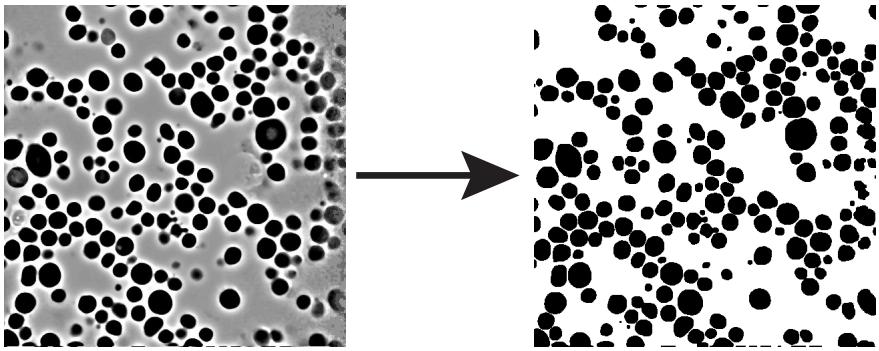

Figure 4.21: The image was then converted to binary.

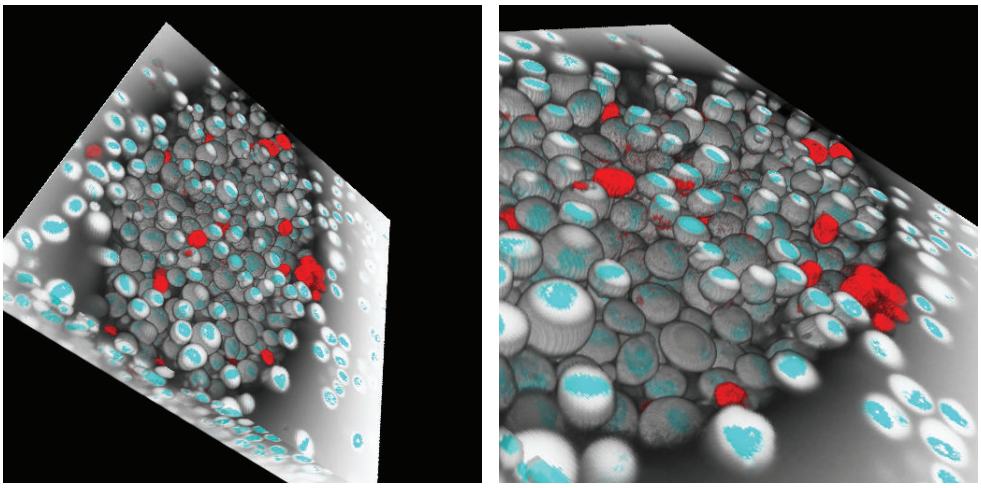

Figure 4.22: Image stack converted to a 3D image.

4.6.5 BoneJ

BoneJ [2] is a free plugin for imageJ. It was initially meant to be a tool for the study of bones structure, but it contained some interesting features that can be used to study other systems. One of these system is the 3D fractal dimension calculator from binary stacks, using a box-counting method [5]. This plugin was used to calculate the 3D fractal dimension of the imaged suspensions, giving us structural clues on the network built by the cells.

4.7 2D fractal dimension from phase contrast microscopy images

Following the method defined in [2] and [8], the fractal dimension of the cells in suspension in the three different medium have been determined. Using some images such as Figure 4.23, circles of radius R_f containing clusters have been drawn. The number of cells N is then counted manually for each aggregate. Using the following relationship, the fractal dimension D is determined:

$$\frac{R_f}{a} \sim N^{\frac{1}{D}} \tag{4.15}$$

where a is the average radius of a cell, taken equals to 7.5 µm. The images have been taken using a phase contrast microscope IX51 from Olympus. This allowed us to compare the fractal dimension measured in 2D and in 3D.

[2]Doube, M. BoneJ. 2009. Available: http://bonej.org/

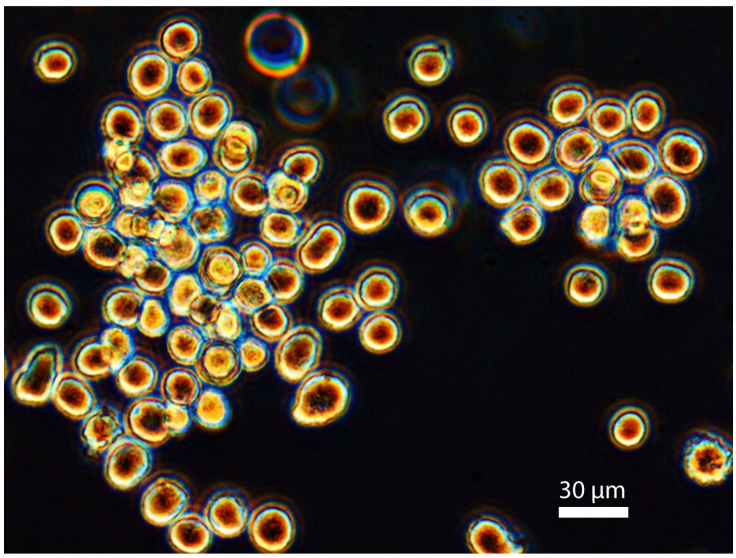

Figure 4.23: Phase contrast microscopy of NIH-3T3 suspension.

References

[1] A. Acrivos, X. Fan, and R. Mauri. On the measurement of the relative viscosity of suspensions. *J. Rheol.*, 38(5):1285–1296, 1994.

[2] C. Allain and B. Jouhier. Simulation cinétique du phénomène d'aggrégation. *J. Phys. Lettre*, 45:421–428, 1983.

[3] B.K. Chapman and D.T. Leighton. Dynamic viscous resuspension. *Int. J. Multiphase Flow*, 17:469–483, 1991.

[4] W. Denk, J.H. Strickler, and W.W. Webb. Two-photon laser scanning flumicroscopymicroscopy. *Science*, 248(4951):73 – 76, 1990.

[5] M. Doube, M.M. Klosowski, I. Arganda-Carreras, F.P. Cordelières, R.P. Dougherty, J.S. Jackson, B. Schmid, J.R. Hutchinson, and S.J. Shefelbine. Bonej: free and extensible bone image analysis in imagej. *Bone*, 47:1076 – 1079, 2010.

[6] E.C. Eckstein, D.G. Bailey, and A.H. Shapiro. Self-diffusion of particles in shear flow of a suspension. *J. Fluid Mech.*, 79:191–208, 1977.

[7] A.S. Inácio, K.A. Mesquita, M. Baptista, J. Ramalho-Santos, and W.L.C. Vaz. Surfactant structure-toxicity relationships: Implications for surfactant use in sexually transmitted infection prophylaxis and contraception. *PLoS ONE*, 6(5):e19850, 05 2011.

[8] A. Iordan, A. Duperray, and C. Verdier. Fractal approach to the rheology of concentrated cell suspensions. *Phys. Rev. E*, 77, 2008.

[9] D.S. Kalika, L. Nuel, and M.M. Denn. Gap dependence of the viscosity of a thermoplastic liquid cryscrystal copolymer. *J. Rheol.*, 33:1059 – 1070, 1989.

[10] J. Kramer, J.T. Uhl, and R.K. Prudhomme. Measurment of the viscosity of guar gum solutions to 50 000 s-1 using a parallel plate rheometer. *Polym. Eng. Sci.*, 27:598–602, 1987.

[11] D. Leighton and A. Acrivos. Viscous resuspension. *Chem. Eng. Sci.*, 41(6):1377–1384, 1986.

[12] M. Oheim, D.J. Michael, M. Geisbauer, D. Madsen, and R.H. Chow. Principles of two-photon excitation fluorescence microscopy and other nonlinear imaging approaches. *Advanced Drug Delivery Reviews*, 58(7):788 – 808, 2006. <ce:title>Multi-Photon Imaging: Diseases and Therapies</ce:title>.

[13] Peter T. C. So, Chen Y. Dong, Barry R. Masters, and Keith M. Berland. Two-photon excitation fluorescence microscopy. *Annual Review of Biomedical Engineering*, 2(1):399–429, 2000. PMID: 11701518.

[14] J.R. Stokes and G.A. Davies. Viscoelasticity of human whole saliva collected after acid and mechanical stimulation. *Biorheology*, 44:141–160, 2007.

[15] A. Yoshimura and R.K. Prud'Homme. Wall slip corrections for couette and parallel disk viscometers. *J. Rheol.*, 32:53–67, 1988.

Chapter 5

Rheology of NIH-3T3 suspensions

Contents

Part of the work described in this chapter has been published as a paper in Biomacromolecules.

Résumé du Chapitre

Dans ce cinquième chapitre, nous traitons des propriétés rhéologiques des suspensions de cellules NIH-3T3 vivantes. Les échantillons sont préparés selon les protocoles décrits dans le chapitre précédent.

La première partie traite des résultats expérimentaux obtenus, que ce soit en rhéométrie ou lors de l'étude de la structure de la suspension au repos à l'aide d'un microscope bi-photonique.

La deuxième partie est une section consacrée à la discussion de ces résultats. Le comportement observé est complexe et des mécanismes sous-jacents sont proposés. Un modèle analytique proposé dans la littérature est utilisé pour démontrer l'universalité de ces mécanismes en fonction de la fraction volumique. La force d'adhésion entre les cellules est ensuite calculée pour nos données expérimentales, et est comparée à celles reportées dans la littérature.

5.1 Introduction

The flow properties of suspensions are closely related to the nature of the particles within them. Various microscopic parameters intrinsic to the very nature of the particles being investigated, such as shape, size, affinity with other particles, elastic modulus, deformability and buoyancy, are highly correlated to tailoring the resultant macroscopic parameters relevant to continuous processing methodologies, such as viscosity and viscoelasticty [26]. Insights into the impact of these microscopic parameters on the rheology of these complex systems allows us to understand, for example, the evolution of their flow behavior under the impositions of shear or extensional flows. In the end, the ability to predict and explain the differences in non-Newtonian behaviours of these complex living systems lies in the ability to understand the evolution of the microscopic organization of the particles within the suspending fluid [26]. The use of living cells induces biological variability, an input that is inherent to cellular systems, as well as the naturally complex aggregation mechanisms involved in cell-cell adhesion mechanisms. The microstructure of suspensions of attractive particles is known to be highly sensitive to shear flow, as the cluster shape, size and compactness change with the imposition of shear stress [13, 16, 22]. Thanks to the recent developments in microrheology techniques, the rheology of individual cells has started to become, at least well documented [9, 29, 30]. However, the macroscale properties of such materials remain largely unexplored. The lack of published work in this area is highly linked to the difficulties inherent to the use of living cells in traditional rheological measurements, which include the variability of the samples or the time and cost of culturing enough cells for a single test with conventional rheometry setups.

5.2 Materials and Methods

All materials and methods used in this chapter are described in Chapter 4. The preparation of the cell suspension is described in Section 4.2.2. The protocol for the rheological characterisation of the suspensions is described in Section 4.3.1, and the two-photon microscopy protocol and analysis methods are described in Section 4.6.2 to 4.6.5.

5.3 Results

5.3.1 Rheology of cell suspensions

We first focus on the suspension behavior of fibroblast cells in standard Dulbecco's Modified Eagle's Medium (DMEM) high glucose, which is a Newtonian fluid with a viscosity of 1.09 mPa s. Over the range of shear stresses (σ) and volume fractions (φ) tested, several behaviors are exhibited (Figure 5.1). The flow curves can be divided into different parts, each giving indications of how the microstructure of the material reacts to the imposition of shear forces.

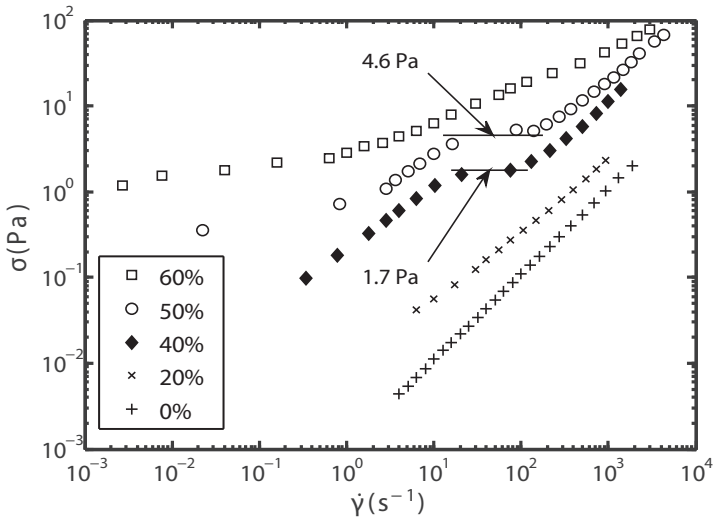

Figure 5.1: Shear stress as a function of the shear rate at different volume fractions.

First, under low shear stresses and at high volume fractions, the suspensions exhibit a yield stress. Using a Herschel-Bulkley model on this part of the curve, the yield stress was estimated to be approximately 0.35 Pa and 1.5 Pa for $\varphi = 50\%$ and 60%. The lack of data at low enough shear stresses is an issue for the accurate determination of the yield stress for the lower volume fractions. As the shear stress increases beyond the yield stress, the system displays strong shear thinning behavior, until a plateau is reached, see Figure 5.2. The appearance of such a plateau indicates a reorganization of the material to a more stable microstructure. At $\varphi = 40\%$ and 50%, this plateau-like region ends abruptly at 1.7 Pa and 4.6 Pa respectively. The viscosity drops significantly thereafter, suggesting a sharp change or rearrangement in the architecture of the cell clusters. The viscosity stabilizes again at higher shear stresses, reaching a Newtonian-like plateau prior to the end of the tests. These results suggest that the microstructure of the material does not evolve any further over the range of shear stresses tested. At very high volume fractions ($\varphi = 60\%$), the absence of these different plateaus and the drop in viscosity suggests that the mechanisms ruling the behavior of the suspension at 40 and 50% do not apply, or at least do not have the same impact, at higher volume fractions. Any changes in microstructure seemingly happen more continuously, without sharp or sudden restructuring. At

lower volume fraction (20%), the flow curve is substantially different again. The shape of this curve is similar to that displayed by semi-dilute viscoelastic particles suspensions [23], exhibiting shear thinning followed by a plateau.

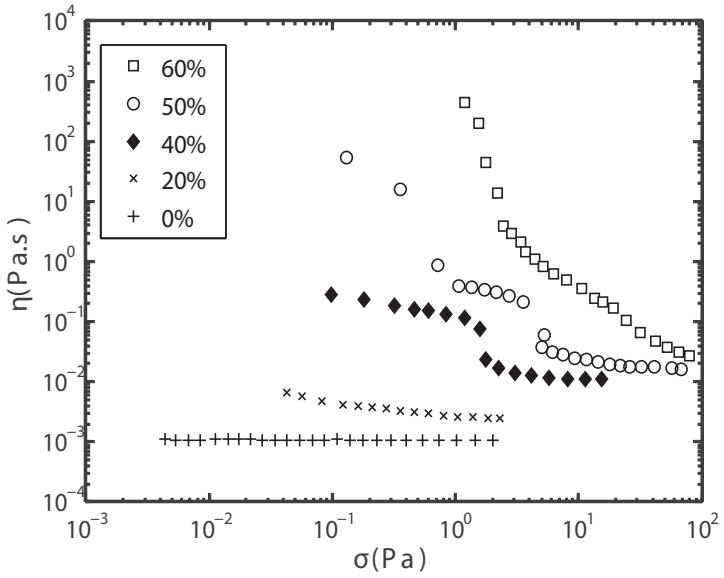

Figure 5.2: Viscosity of 3T3 suspensions in DMEM as a function of the applied shear stress at different volume fractions.

Defining the relative viscosity η_r as the ratio between the measured viscosity and the viscosity of the suspending fluid used, Figure 5.3 shows the evolution of the relative viscosity as a function of the volume fraction at different shear stresses. As discussed in the earlier chapters, non-interacting hard spheres suspensions rheology should be nearly independent of the shear applied, being ruled only by the volume fraction. Unsurprisingly, it is hardly the case in our system. Indeed, cells are not hard spheres, and above all are not non-interacting, creating clusters and network if the concentration of cells is high enough.

5.3.2 Fractal dimension of cell suspensions

If there is no repulsion between the particles, each collision induces the creation of an adhesion. This is referred to as Diffusion Limited Aggregation (DLA) and is characterized by low fractal dimension (approximately 1.7). The second is referred to as Reaction Limited Aggregation (RLA) and is characteristic of systems where the particles can have either a repulsive force, or a lower probability of adhesion when the particles come into contact [27]. In this case, the fractal dimension is generally higher, the repulsion being stronger, and we see the fractal dimension approaching 2.1. The values of the fractal dimension thus give important structural information about the architecture of the cellular aggregates. Indeed, the lower the fractal dimension, the more porous the aggregates. Therefore to obtain a compact structure, it is necessary that the porosity developed during any growth of an aggregate stay low; in other words, it is necessary to fill

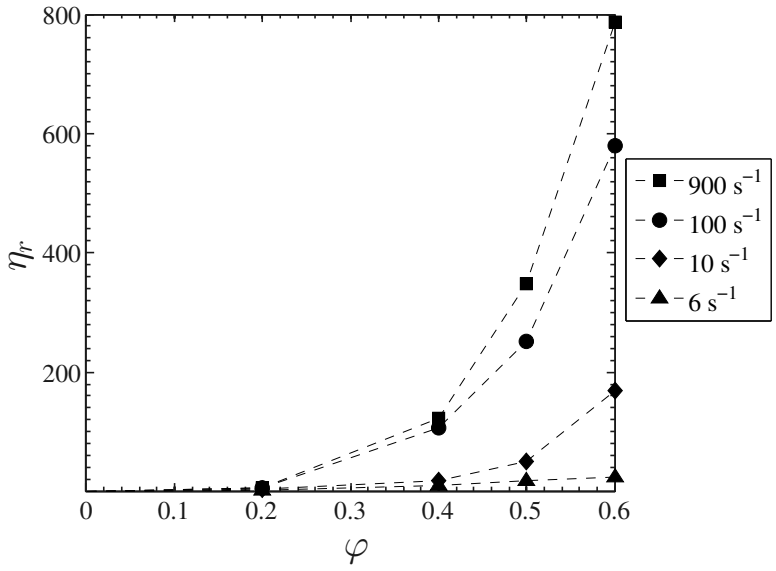

Figure 5.3: Relative viscosity as a function of the volume fraction at different shear rates.

the biggest void created after a collision between two sub units with other particles (Fig. 5.4A). When the 'sticking probability' is high, the particles tend to stay where/when they hit the other particles, whereas if the 'sticking probability' is low, particles and small clusters of particles will be able to explore several binding sites before creating a strong adhesion site. Thus, the aggregates and the particles have more chances to fill the void (Fig. 5.4B). However, when aggregation also occurs under shear (orthokinetic aggregation), the fractal dimension values tend to be higher and range between 2.1 and 2.7, according to the volume fraction, the shear experienced, the shear history and the aggregates size [4, 17, 25]. By changing the particles trajectory, the shear changes the arrangement of the aggregate. Shear forces can also breakup aggregates, finally leading to a balance between growth and breakup.

5.3.2.1 Estimating the 3D fractal dimension from 2D images

Following the protocol of Allain and Jouhier [2], the fractal dimension of our suspension can be measured in two dimensions as described in Section 4.7. Using a circle of radius R, an aggregate is isolated and the cells present in the cluster are counted. This enables us to plot Figure 5.5, where the slope of the curve represents the inverse of the fractal dimension. Figure 5.5 shows that for the fibroblast cell suspensions $df = 1.76$, which is close to 1.7. This value is within the range of values (1.48 - 1.94) previously reported for two dimensional aggregation of particles under different shear and coagulant dose conditions [7]. Ganguly et al. [10] recently proposed a relationship between 2D and 3D fractal dimensions:

$$d_{f_3D} = 0.47 d_{f_2D} + 1.78 \tag{5.1}$$

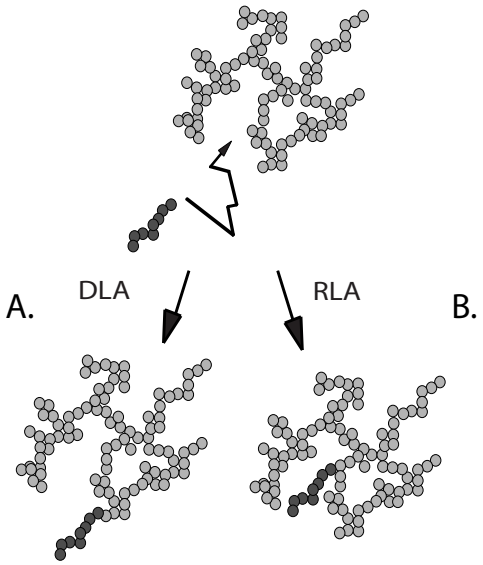

Figure 5.4: Schematic of the outcome of a collision between a primary aggregate and a smaller secondary aggregate, (A) following the Diffusion-Limited Aggregation (DLA) and (B) following the Reaction-Limited Aggregation (RLA).

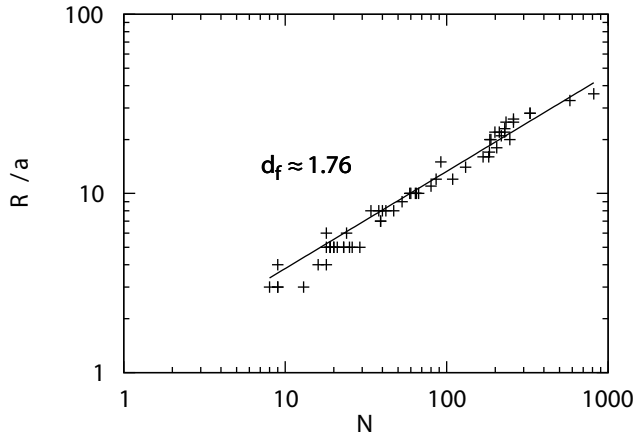

Figure 5.5: Ratio of the size of an aggregate with the size of a single cell as a function of the number of cells constituting the aggregate.

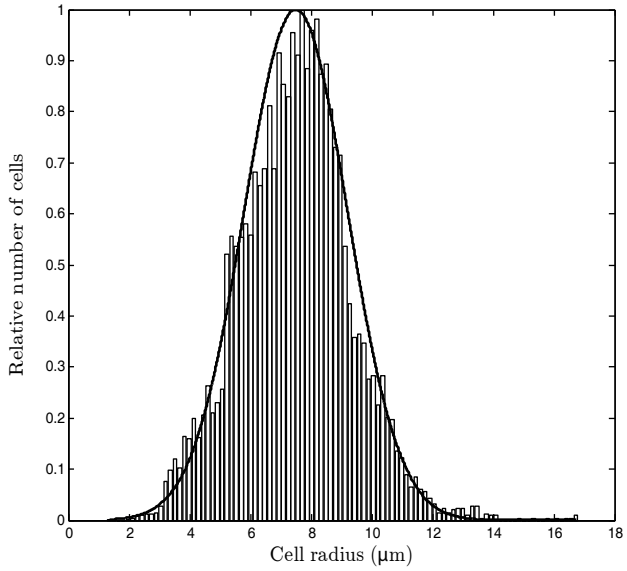

Figure 5.6: Size distribution of the cell suspension studied, the line is a normal distribution with the same average and standard deviation than the suspension

where d_{f_3D} and d_{f_2D} are the 3D and 2D fractal dimensions respectively. This relationship was found using a regression analysis between data of 2D fractal dimensions and 3D fractal dimensions of a large number of clusters. This relationship enables us to estimate the 3D fractal dimension from our 2D fractal dimension. The 3D fractal dimension of our suspension is thus expected to be close to 2.58.

5.3.2.2 3D fractal dimension from two-photon microscopy images

Using two-photon microscopy images, we managed to measure the actual volume fraction of the suspensions, the size and shape of the cells, as well as their fractal dimension, using a box-counting method. The suspensions showed noticeable polydispersity, as well as variations in cell shape and number of neighbors. The average particle radius is 7.5 μm with a standard deviation of 1.7 μm. The line in Figure 5.6 represents a normal distribution with the same average and standard deviation as our suspension.

For this complex living system, being far from the ideal soft particle suspension, it was essential that our images were representative of the overall suspension, so that we could confidently extract significant information from them. The consistency of the relationship linking measured and theoretical volume fraction between the different systems tested, see Figure 5.7-A, confirmed this. Figure 5.7-B shows that for the fibroblast cell suspensions, the fractal dimension varies from 2.27 to 2.55 according to the volume fraction. Some what surprisingly, given the non-ideal, biological nature of these living suspensions, these numbers are in very good agreement with those estimated using the method of Ganguly et al. [10], allowing one to estimate 3D fractal dimensions from 2D measurements.

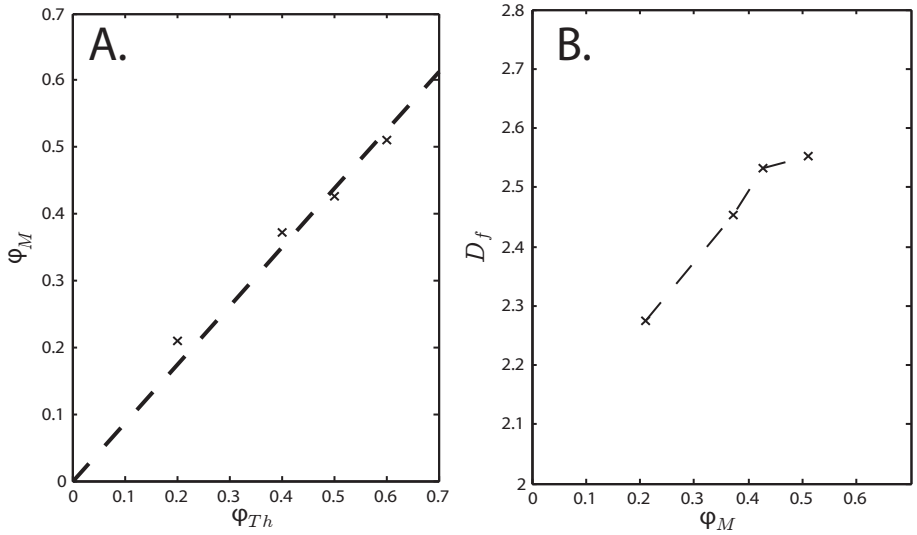

Figure 5.7: (A) Measured volume fraction as a function of the theoretical volume fraction. (B) Measured fractal dimension versus measured volume fraction.

5.4 Discussion

The evolution of the relative viscosity as a function of the volume fraction for soft particles and clusters of soft or hard particles is expected to show different behaviors according to the shear experienced [15, 18, 23]. For our cellular system, we expect that the microstructure of the system is evolving with both the volume fraction and the shear stress. This double dependency has already been observed in suspensions made of soft particles and/or particles with the ability to aggregate, and is believed to be linked to the capacity of the particles to deform and orient in the flow, in the case of disperse systems, and to the ability of the aggregates to be deformed and eroded, in the case of aggregating systems [15, 23]. This tendency to be modified with the shear changes the microstructure of the material, increasing the maximum packing volume fraction and thus inducing shear thinning. The yield stress and the shear thinning behavior are also linked to the break down of aggregates or clusters, into clusters of smaller size as well as their progressive erosion due to the shear. The density and the size of the aggregates modify the effective volume fraction of the dispersed phase, leading to a change in the dynamic of the suspension. Therefore, it is crucial to be able to characterize the structure of the aggregates as well, as a key parameter of the dynamics of the aggregation and breakup process itself [17].

All cells have the intrinsic ability to associate with other cells through a multitude of known cell-cell adhesion molecules that they display on their surfaces. Cells can thus aggregate and create large clusters, which obviously will have different dynamics to that of a single cell. The cellular clusters resulting from this aggregation have previously been referred to by Iordan et al. as objects following constitutive fractal laws [13]. Accordingly, it is possible to estimate the average size of the clusters present in the suspension under different shear

stresses [6]. The size of an aggregate is proportional to the size of the particles constituting the aggregate, [6, 8, 13], and hence the number of particles in the aggregate and its fractal dimension are as follows:

$$\frac{R}{a} = N^{\frac{1}{d_f}} \tag{5.2}$$

where R is the gyration radius of the aggregate, a is the radius of the constitutive particles, N is the number of particles and d_f is the fractal dimension.

As outlined by Snabre and Mills [22], previous experiments [24, 28] and numerical simulations [19] showed the radius R of a fractal aggregate under a shear flow follows the equation [6]:

$$\frac{R}{a} \simeq 1 + \left(\frac{\sigma^*}{\sigma}\right)^m \tag{5.3}$$

where the critical shear stress $\sigma^* = \frac{\lambda}{a}$ is linked to the adhesion energy per surface units λ and to the elementary radius a (single particle radius). The power m depends on the reversibility of the deformation experienced by the aggregates [5, 19]. Two different trends appear when one investigates the behavior of a sheared aggregate, which correlate with the upper and lower limits of the exponent m: 'hard' aggregates are characterized by an $m = 1/3$, while 'soft' aggregates have an exponent m equal to $1/2$ [6]. The hard aggregates will be fragmented into secondary aggregates of similar size because the elastic deformations are conveyed through their structure. Soft aggregates, on the other hand, are deformed by the external shear and are peeled-off into individual particles and smaller aggregates of various sizes [6, 19, 22].

In the case of the current experimental system, we hypothesise that the cellular aggregates are constituted of both hard and soft aggregate regions: the central region, where higher numbers of connections between cells exist, is akin to a hard aggregate, because of the intrinsically high modulus of the cells and a more uniformly organized micro-structure; whereas the periphery may be seen to approximate that of a soft aggregate, where branches of cells can be deformed and detached from the main body of the aggregate more easily. These soft aggregate regions of the large aggregate are built up of smaller clusters which have collided and remained linked at their contact points [3, 11, 12]. This arrangement is more porous and of lower overall link density, and hence weaker. Moreover, the cohesive strength of the hard and soft aggregates follows different trends [1, 3]. These two different dynamics have direct impact on the evolution of the microstructure, and thus are essential in the understanding of the evolution of the viscosity of the system with the shear.

Such a material should exhibit two critical stresses, a first one linked to the beginning of the detachment of the soft parts of the aggregates, and a second one linked to the destruction of the hard aggregates. The different critical stresses, as well as the different plateaus are linked to the energy equilibrium between the shear and the dynamic of both desaggregation and re-aggregation,

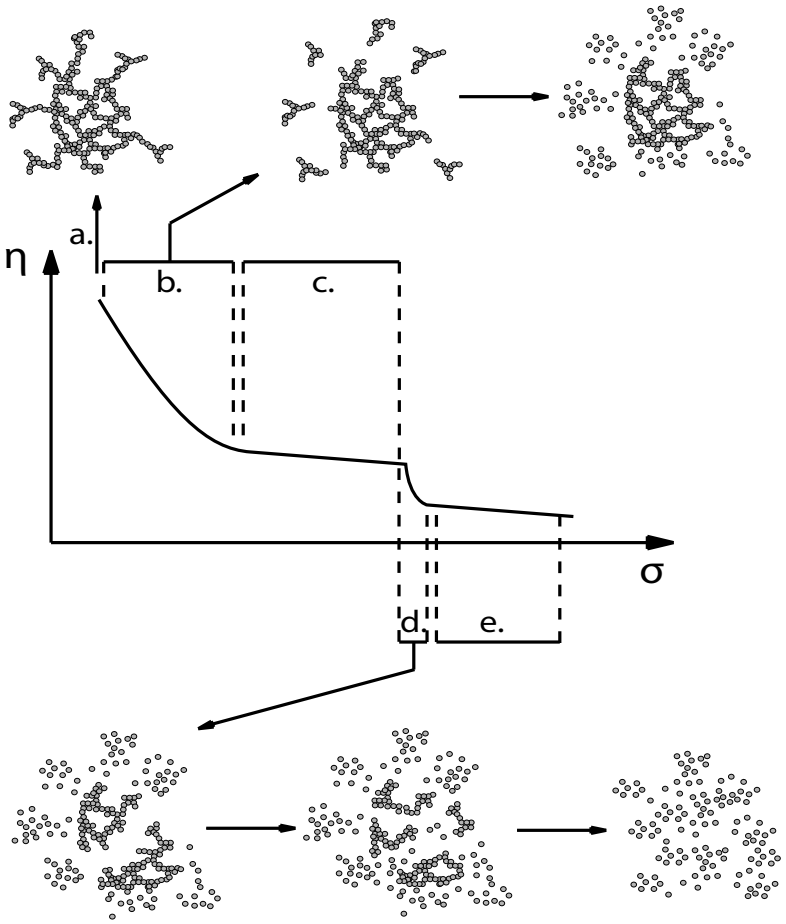

Figure 5.8: Schematic of the link between the evolution of the viscosity of the suspension and the change in microstructure of the aggregates. a. A weak network exists and induces a yield stress. b. The shear thinning is linked with the breakdown of the soft and weak part of the aggregates. c. The first viscosity plateau is correlated with a stable micro arrangement. d. The hard aggregates are broken down until the suspension is made of independent cells. e. Second plateau where the cells are all independent.

as depicted by the schematic of the mechanism in Figure 5.8.

The first critical stress is the yield stress witnessed in the flow curves as shown in Figures 5.1 and 5.2, and it corresponds (schematically) to Figure 5.8 - part a. When the shear stress increases and the general weak network is broken, the soft and weak parts of the original aggregates are detached, and broken down further (Figure 5.8 - part b). An equilibrium can be reached (Figure 5.8 - part c), where the shear is too high for the soft aggregates to reform, but too low for the hard aggregates to be broken down, resulting in the observed plateau in response to shear. This equilibrium in the structure lasts until the second critical shear stress is reached, that is, when the abrupt drop in viscosity is observed. At this point, the hard aggregates are broken down into smaller aggregates, which are then further broken down, with the system getting closer to a suspension of independent, single cells (Figure 5.8 - part d).

These two critical shear stresses evolve with the volume fraction. The

yield stress increases with the volume fraction because of the minimal space available between the different aggregates. The second critical stress increases with the volume fraction as well, because the probability of building an organized aggregate increases with the number of cells for a given volume. For $\varphi = 60\%$, only the first critical stress is visible because of the extremely small amount of space available between the different aggregates. Even if the aggregates get detached and broken down, they are so close to each other that no sudden reorganization is possible.

Several empirical laws exist to describe the evolution of the relative viscosity as a function of the volume fraction. One of the most commonly used is the Krieger and Dougherty model [14]:

$$\eta_r = \left(1 - \frac{\varphi}{\varphi_0}\right)^{-[\eta]\varphi_0} \tag{5.4}$$

where $[\eta]$ is the intrinsic viscosity, taken equal to 2.5 for hard spheres. If one fixes the volume fraction of the suspension, a decrease in φ_0 increases the relative viscosity. In our experiments however, the viscosity decreases because of another phenomenon that has to be taken into account: the aggregates are built of adhesive cells. Further, the volume fraction inside the aggregate is not equal to 1. Indeed, a part of the suspending fluid is trapped inside the aggregate. Thus the effective volume fraction in the suspension post the introduction of shear is higher than the volume fraction measured before the experiment. Moreover, the destruction of the aggregates releases the trapped fluid. The effective volume fraction φ_A is thus defined as [16, 22]

$$\varphi_A = \varphi^* \varphi \tag{5.5}$$

where φ^* is a packing factor, used to determine the maximum radius of the aggregate in the absence of shear [22] and is defined as:

$$\varphi^* = \left(\frac{R}{a}\right)^{3-d_f} \tag{5.6}$$

Using the equation 5.3, it is possible to calculate the evolution of φ^* as a function of σ:

$$\varphi_A = \varphi\varphi^* = \varphi\left(1 + \left(\frac{\sigma^*}{\sigma}\right)^m\right)^{3-d_f} \tag{5.7}$$

Inserting now φ_A into the Krieger-Dougherty model, we have:

$$\eta_r = \left(1 - \frac{\varphi_A}{\varphi_0}\right)^{-[\eta]\varphi_0} \tag{5.8}$$

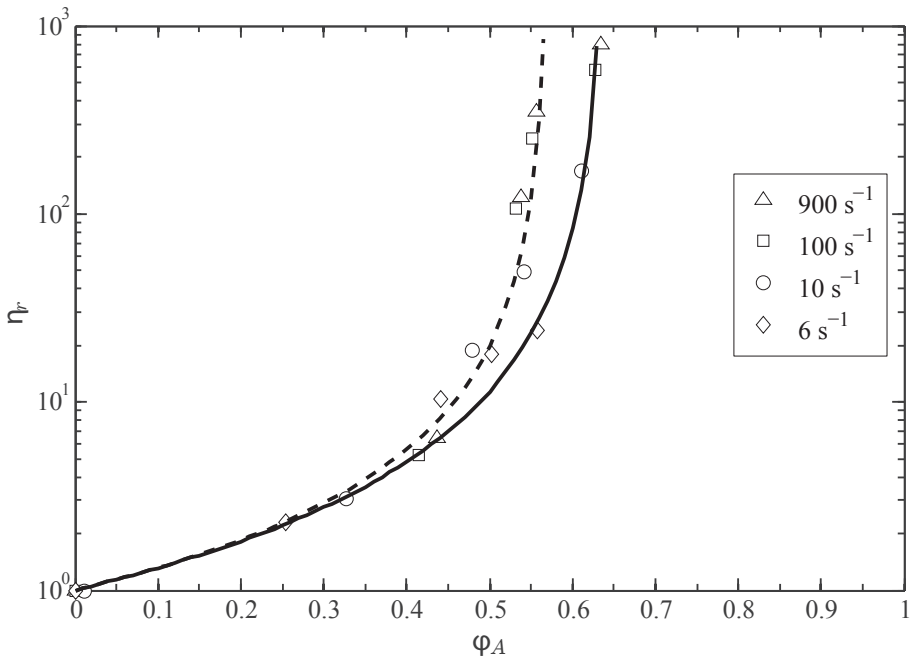

Figure 5.9: Relative viscosity as a function of the effective volume fraction for different HA concentrations and for different shear rates. The solid line is the Krieger and Dougherty model with $\varphi_0 = 0.64$, the broken line is the Krieger and Dougherty model with $\varphi_0 = 0.57$.

Taking into account our hypothesis outlined above regarding the resident structures within the suspension at different shear stresses, and using the outcomes of the analytical formalism above, Figure 6.9 shows the evolution of the relative viscosity as a function of the effective volume fraction for different shear rates. The two lines represent a Krieger and Dougherty model with a maximum packing volume fraction of 0.64 for the solid line, and of 0.57 for the broken line. Indeed, for hard spheres suspensions, the random isostatic packing fraction (0.57) describes well our experimental data for volume fractions lower than 50%, however, when the volume fraction exceeds 50%, a change in spatial distribution of particles happens, which induces an increase in the maximum packing fraction, getting closer to the close random packing fraction [22, 23]. m is taken equal to the soft aggregate limit (1/2) before the viscosity failure, and equal to the hard aggregates limit (1/3) afterwards. The different values of df are the ones measured experimentally.

The only free parameter is then σ^*, which is related with the adhesion force F^* between two cells. The value of this parameter is thus optimized to induce a collapse of the different data sets onto a mastercurve. In the case of our fibroblast cells, this parameter is calculated to be equal to 0.65 Pa. According to the Derjaguin theory [22, ?], the critical force F^* required to break a doublet is:

$$F^* \approx \sigma^* a^2 \tag{5.9}$$

with the critical shear stress σ^* defined as in the equation 5.3. This value of σ^* therefore leads to an adhesion force between cells F^* of approximately 36.5 pN, which is certainly in the range of cell-cell adhesive forces reported in the literature, which vary from 15 to 40 pN for mouse fibroblast Balb/c3T3 and up to 48 pN for WM115 melanoma cells [20, 21, 31]. This value of adhesion force is the adhesion force between two cells, averaged over the whole population, therefore over millions of cells.

5.5 Conclusion

The data and the analytical model confirm that cell-cell interactions have to be taken into account in order to explain quantitatively and qualitatively the flow behaviors of living cells suspensions. Appreciation of the dynamics of the aggregates within these suspensions of adhesive microparticles are critical in order to permit analysis and interpretation of the complicated flow curves of this kind of system. Through this method, the adhesion force between cells can be accurately measured across a population of thousands to millions of cells by simply coupling rheometry and two photon microscopy and the developed analytical model.

These results outline the necessity to understand and tailor the flow properties of cell suspensions. The yield stress behavior witnessed at high concentration especially explains the current limitation in the case of injectable systems in tissue engineering and regenerative medicine where syringes are used. The needles used being the smallest possible, in order to have the less invasive surgery possible, the shear on the cells have to be considered. Indeed, the shear rate in these systems ranges from below 10^{-2} s^{-1} in the syringe, up to several hundreds if not thousands in the needle. The pressure necessary to overcome the yield stress could therefore induce an even higher shear rate in the needle region, which could in turn potentially harm and kill the cells.

References

[1] C. Allain, M. Cloitre, and F. Parisse. Settling by cluster deposition in aggregating colloidal suspensions. *J. Colloid Interface Sci.*, 178:411–416, 1996.

[2] C. Allain and B. Jouhier. Simulation cinétique du phénomène d'aggrégation. *J. Phys. Lettre*, 45:421–428, 1983.

[3] D.F. Bagster and D. Tomi. The stresses within a sphere in simple flow field. *Chem. Eng. Sci.*, 29:1773–1783, 1974.

[4] G. Barthelmes, S.E. Pratsinis, and H. Buggisch. Particle size distributions and viscosity of suspensions undergoing shear-induced coagulation and fragmentation. *Chem. Eng. Sci.*, 58:2893–2902, 2003.

[5] G. Bossis and A. Meunier. Hydrodynamic stress on fractal aggregates of spheres. *J. Chem. Phys.*, 94(7):5064–5070, 1991.

[6] M. Boynard, L. Haïder, and P. Snabre. Etude rhéo-acoustique de la rupture d'agrégats de particules en suspension dans un champs de cisaillement: Application à la désagrégation des globules rouges. *ITBM-RBM*, 23:23–39, 2002.

[7] R.K. Chakraborti, K.H. Gardner, J.F. Atkinson, and J.E. Benschoten. Changes in fractal dimension during aggregation. *Water Research*, 37:873–883, 2003.

[8] P.G. de Gennes. *Scaling concepts in polymer physics*. Cornell University Press.Cornell University Press, 1979.

[9] B. Fabry, G.N. Maksym, J.P. Bulter, M. Glogauer, and J.J. Fredberg. Scaling the microrheology of living cells. *Phys. Rev. Lett.*, 87(14):148102, 2001.

[10] S. Ganguly, S. Basu, and S. Sikdar. Determination of the aggregate fractal dimensions in colloidal nanofluids. *Proc IMechE Part N: J Nanoengineering and Nanosystems*, 226(1), 2012.

[11] T.J. Gillespie. An extension of goodeve's impulse theory of viscosity to pseudoplastic systems. *J. Colloid Sci.*, 15:219, 1960.

[12] C.F. Goodeve. A general theory of thixotropy and viscosity. *Trans. Faraday Soc.*, 35:342 – 358, 1939.

[13] A. Iordan, A. Duperray, and C. Verdier. Fractal approach to the rheology of concentrated cell suspensions. *Phys. Rev. E*, 77, 2008.

[14] I.M. Krieger and T.J. Dougherty. A mechanism for non-newtonian flow in suspensions of rigid spheres. *Trans. Soc. Rheol.*, 3:137–152, 1959.

[15] Y.L. Lin, D.M. Wang, W.M. Lu, Y.S. Lin, and K.L. Tung. Compression and deformation of soft spherical particles. *Chem. Eng. Sci.*, 63:195–203, 2008.

[16] P. Mills and P. Snabre. The fractal concept in the rheology of concentrated suspensions. *Rhe*, 26:105–108, 1988.

[17] V. Oles. Shear-induced aggregation and breakup of polystyrene latex particles. *J. Colloid Interface Sci.*, 154(2):351–358, 1992.

[18] R. Pal. Rheology of concentrated suspensions of deformable elastic particles such as human erythrocythes. *J. Biomech.*, 36:981–989, 2003.

[19] A.A. Potanin. On the computer simulation of the deformation and break up of colloidal aggregates in shear flow. *J. Colloid Interface Sci.*, 157:399–410, 1993.

[20] P.H. Puech, K. Poole, D. Knebel, and D.J. Muller. A new technical approach to quantify cell-cell adhesion forces by afm. *Ultramicroscopy*, 106:637–644, 2006.

[21] L. Sirghi, J. Ponti, F. Broggi, and F. Rossi. Probing elasticity and adhesion of live cells by atomic force microscopy indentation. *Eur. Biophys. J.*, 37:935–945, 2008.

[22] P. Snabre and P. Mills. Rheology of weakly flocculated suspension of rigid particles. *J. Phys. III*, 6:1811–1834, 1996.

[23] P. Snabre and P. Mills. Rheology of concentrated suspensions of viscoelastic particles. *Colloids Surf., A*, 152:79–88, 1999.

[24] R.C. Sonntag and W.B. Russel. Structure and breakup of flocs subjected to fluid stresses: Ii. theory. *J. Colloid Interface Sci.*, 115(2):378–389, 1987.

[25] P.T. Spicer, S.E. Pratsinis, and M.D. Trennepohl. Coagulation and fragmentation: The variation of shear rate and the time lag for attainment of steady state. *Ind. Eng. Chem. Res.*, 35:3075–3080, 1996.

[26] J.J. Stickel and R.L. Powell. Fluid mechanics and rheology of dense suspensions. *Annu. Rev. Fluid Mech.*, 37:129–149, 2005.

[27] A. Thill. *Agregation des particules: structure, dynamique et simulation. Application au cas d'un ecoulement stratifie: l'estuaire du Rhone*. PhD thesis, Universite de Droit, d'Economie et des Sciences d'Aix-Marseille, 1999.

[28] F.E. Torres, W.B. Russel, and W.R. Schowalter. Simulations of coagulation in viscous flows. *J. Colloid Interface Sci.*, 145(1):51–73, 1991.

[29] Y. Tseng and T.P. Kole. Micromechanical mapping of live cells by multiple-particle-tracking microrheology. *Biophys. J.*, 83(6):3162 – 3176, 2002.

[30] D. Wirtz. Particle-tracking microrheology of living cells: principles and applications. *Annu. Rev. Biophys.*, 38:301 – 326, 2009.

[31] X. Zhang, A. Chen, D.D. Leon, H. Li, E. Noiri, V.T. Moy, and M.S. Goligorsky. Atomic force microscopy measurement of leukocyte-endothelial interaction. *Am. J. Physiol. Heart Circ. Physiol.*, 286:H359 – H367, 2003.

Chapter 6

Adding HA to the suspension

Contents

Part of the work described in this chapter has been published as a paper in Biomacromolecules.

Résumé du Chapitre

Dans ce sixième chapitre, nous nous focalisons sur l'impact de l'ajout d'une macromolécule naturelle: l'acide hyaluronique.

Dans une première partie, nous présentons les résultats des expériences rhéométriques réalisées sur ce système. Différentes concentrations et différents poids moléculaires sont utilisés pour avoir une spectre suffisamment large de données pour les comprendre et les interpréter. La présence des récepteurs surfaciques spécifiques à l'acide hyaluronique est vérifiée sur les cellules par cytométrie de flux. La présence de particules d'acide hyaluronique à la surface des cellules est elle aussi vérifiée en fonctionnalisant certaines des molécules avec un fluorophore et en imageant la suspension grâce à un microscope confocal. La dimension fractale de ce système est mesurée elle aussi.

Comme dans le chapitre précédent, la deuxième partie de ce chapitre porte principalement sur la discussion des résultats obtenus. Les mécanismes pouvant expliquer l'effet de l'ajout de l'acide hyaluronique dans la suspension sont étudiés. L'impact de l'acide hyaluronique sur la structure de la suspension est discuté, et le modèle analytique du chapitre précédent est modifié en conséquence.

6.1 Introduction

In this chapter, experiments similar to those described in the previous chapter are conducted. The main difference lies in the composition of the suspending fluid. Indeed, now that the rheological behaviours of live mesenchymal cell suspensions had been studied, a biomacromolecule was added to the suspending fluid: hyaluronic acid (HA). HA is widely present in the body and is known to be able to interact with cells through a set of surface receptors. It is also commonly used as a component in hydrogels for tissue engineering applications. The aim of this chapter was to investigate the impact of the addition of HA to the suspension in terms of influence on the rheology of the material, and to probe the underlying mechanisms.

6.2 Materials and Methods

All materials and methods used in this chapter are described in Chapter 4. The preparation of the cell suspension is described in Section 4.2.2. The protocol for the rheological characterisation of the suspensions is described in Section 4.3.1. The no-slip condition was verified as described in the Section 4.3.1 (data not shown). The preparation of the fluorescently labelled HA is detailed in Section 4.5.1, and the fluorescently activated cell sorting (FACS) method is outlined in Section 4.4. The two-photon microscopy protocol and analysis methods are described in Section 4.6.2 to 4.6.5.

6.3 Results

6.3.1 Rheology of cell suspensions with HA

The same set of experiments as performed in Chapter 5 was repeated after adding a high molecular mass HA (1.7 MDa) to the DMEM at concentrations of 250 µg/mL and 750 µg/mL.The addition of HA to the media at these concentrations created two Newtonian suspending fluids (over the shear rate range tested), with viscosities of 1.77 mPas and 4.85 mPas (see Figure 6.1).

Defining the relative viscosity η_r as the ratio between the measured viscosity and the viscosity of the suspending fluid used, Figures 6.2 and 6.3 show the evolution of the relative viscosity as a function of the shear stress and of the volume fraction, respectively.

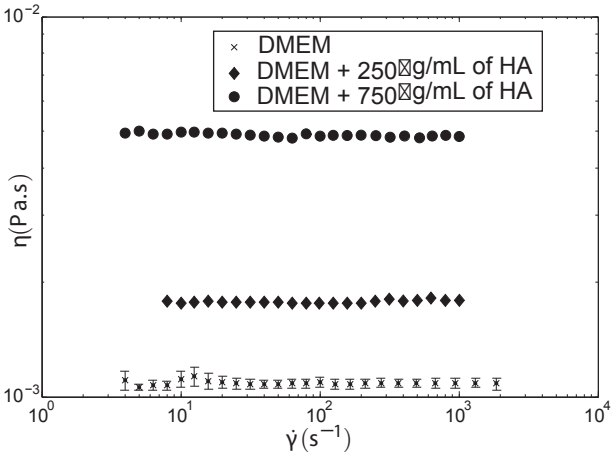

Figure 6.1: Viscosity as a function of the shear rate of the three suspending fluids.

Referring to Figure 6.2, the magnitude of the relative viscosity appears to be decreased by the presence of HA. The addition of HA also decreases the yield stress. Both trends are accentuated when the concentration of HA is increased. Indeed, at $\varphi = 50\%$ and 60% with 750 µg/mL of HA, the yield stress is reduced to 0.01 Pa and 0.09 Pa, respectively. The exponent of the Herschel-Bulkley model applied on this part of the curves increases from 0.47 to 0.8 at $\varphi = 60\%$, indicating that the magnitude of shear thinning is also affected. The sharp drop in viscosity is modified in terms of sharpness, magnitude and threshold. Overall, the presence of the HA seems to soften the drop, decrease its magnitude and reduce the shear stress at which the drops occurs (the threshold being approximately 1 Pa and 2 Pa for 250 µg/mL and 0.7 Pa and 1.5 Pa for 750 µg/mL for volume fractions of 40% and 50%, respectively). However, at $\varphi = 60\%$ the overall shape of the curve evolves with the presence of HA. The elements of the flow curves witnessed at other volume fractions but in the absence of HA start to appear, especially the appearance of two plateau at moderate and high shear stresses.

Figure 6.3 shows the evolution of the relative viscosity as a function of the measured volume fraction, at different shear rates, with and without HA. The evolution of the relative viscosity with both the volume fraction and the shear applied shows similar behaviour in each system studied, the presence of HA only reducing the magnitude of the relative viscosity, as mentioned above.

6.3.2 Presence of HA on the surface of the cells

The analysis of the evolution of the relative viscosity with increasing shear and changes in volume fraction shows that the HA has a noticeable impact on the rheology of suspensions of fibroblast cells. High resolution imaging of fibroblasts and fluorescently labeled HA was performed using a confocal microscope in order to elucidate the underlying mechanisms by which such substantial changes in behavior may occur. Figure 6.4 shows the presence of HA on the surface of each of the fibroblast cells. It seems, on closer inspection, that the HA binds

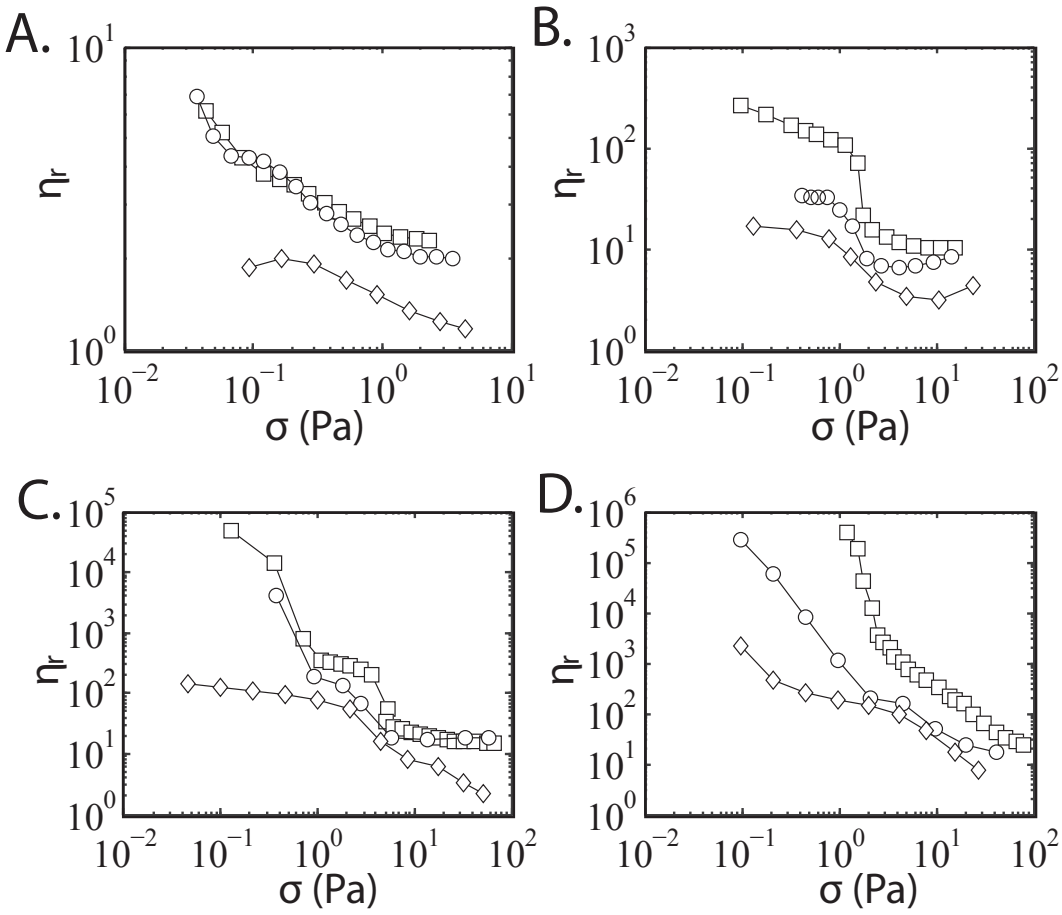

Figure 6.2: Relative viscosity as a function of shear stress for different concentration in HA ((□) without HA, (○), 250 µg/mL and (⋄) 750 µg/mL of HA) with different volume fractions. (A) φ=20%. (B) φ=40%. (C) φ=50% (D) φ=60%.

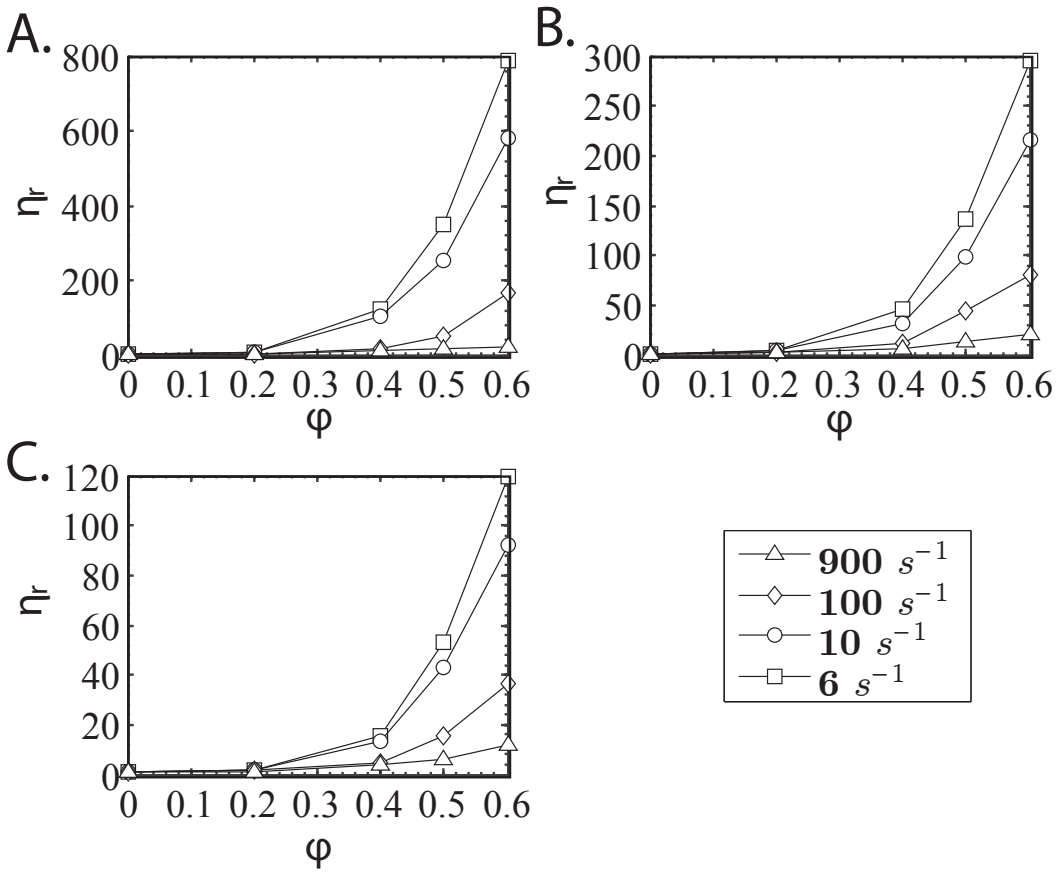

Figure 6.3: Relative viscosity as a function of the volume fraction at different shear rates. (A) Without HA. (B) With 250 μg/mL. (C) With 750 μg/mL of HA.

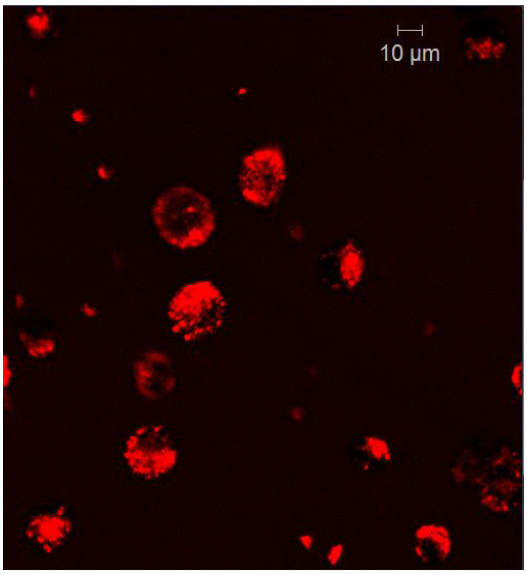

Figure 6.4: Confocal image of 3T3 with labeled HA (in red).

potentially to very specific sites, as denoted by the presence of bright punctuate red dots on the surface of the cells, and not as a diffuse layer.

HA is a macromolecule widely spread in several soft connective tissues and interacts with cells via several receptors [7]. The two primary receptors for HA are the cell surface glycoprotein (CD) 44 and the receptor for hyaluronic acid mediated mobility (RHAMM, also known as CD168). Figure 6.5 shows the result of FACS (fluorescently activated cell sorting) for this two receptors as recently reported by Hatchet *et al.* [3] . The gate was set relative to a negative control at the 1% level. Over 99% of the cells expressed both HA receptors.

6.3.3 Adding HA of different molecular weight

After confirming that the HA was indeed interacting specifically with the cells and also visualizing its mode of presentation on the surface of the cells, we thereafter decided to investigate the impact of HA molecular weight on the resulting rheology of the cell suspension. A second HA of lower molecular mass (66.3 kDa) was thus studied and used at a concentration of 30 µg/mL, in order to have the same number of molecules as in the 750 µg/mL solution of high molecular mass HA. It appears that the lower molecular weight of HA, the less effective it is at changing the rheology of the suspension, especially, the yield stress removal, as shown in Figure 6.6C. This data suggests that the length of the molecule of HA (or its hydrodynamic radius) plays a role in the disruption of network formation, with the high molecular mass HA preventing the formation of the first network, as shown schematically in Fig. 6.6A and B. This result is not surprising if one considers the differences in gyration radius, which are theoretically approximately 30 nm for the 66.3 kDa HA, and approximately 160 nm for the 1.7 MDa HA [6]. It is then expected that the higher molecular mass HA will take up more of the available surface area of the cells, affecting more screening of cell/cell adhesions.

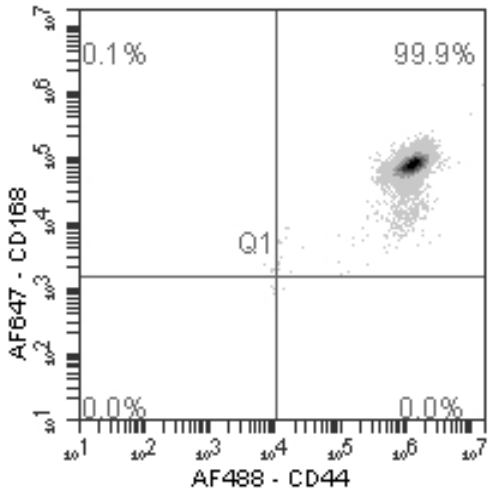

Figure 6.5: FACS plot for 3T3s. The two quarters on the right are used to show the presence of CD44, the top two the presence of CD168, thus the top right quarter shows the presence of both CD168 and CD44.

It is still however unclear mechanistically as to explicitly how the HA prevents the creation of these adhesions but it is likely due to either a.) the presentation of the HA molecule over the surface of a cell, at defined interaction sites, effectively preventing a second cell (through screening) from accessing available cell/cell receptors; or b.) the compression of the HA chains (similar to the compression of the grafted polyelectrolytes brushes in colloid stabilization [8]) between two approaching cells prevents these two cells from getting close enough to create strong adhesive bonds. In both cases, the resulting adhesion force between the two cells will be significantly decreased, effecting the observed changes in the rheological behavior of these concentrated suspensions of adhesive, deformable particles.

6.3.4 Fractal dimension

Figures 6.7 and 6.8B show the fractal dimension measured using the previously detailed 2D and 3D methods (see Sections 4.6.5 and 4.7), respectively.

The addition of HA induces an increase of the fractal dimension, which ranges from 2.32 to 2.58, and from 2.37 to 2.63, for 250 μg/mL and 750 μg/mL of HA, respectively. Some what surprisingly, given the non-ideal, biological nature of these living suspensions, these numbers are in very good agreement with those estimated using the method of Ganguly et al. and the measured 2D fractal dimensions. These data now provide the required insight into the influence of HA on the cellular suspension: aggregates become harder to form and are less porous.

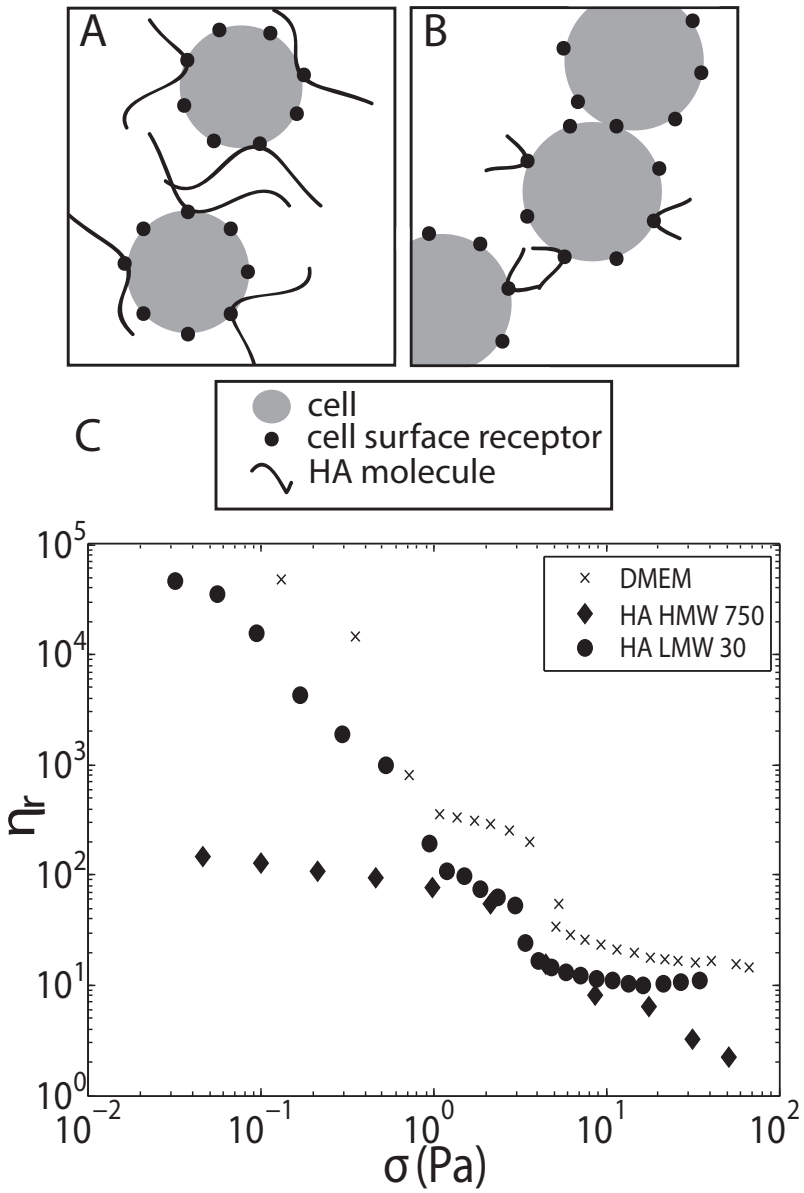

Figure 6.6: Effect of the molecular mass of HA used. (A) Schematic of the impact of high molecular weight HA. (B) Schematic of the impact of low molecular weight HA. (C) Relative viscosity as a function of shear stress for different molecular mass HA, but with the same number of molecules.

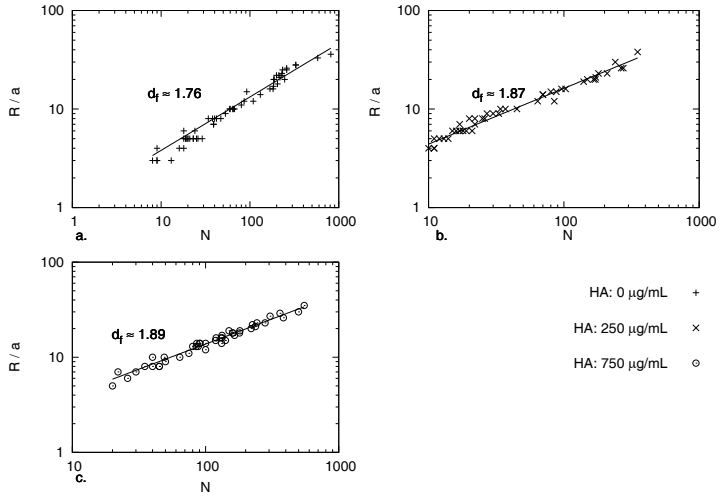

Figure 6.7: (A) Measured volume fraction as a function of the theoretical volume fraction. (B) Measured fractal dimension versus measured volume fraction.

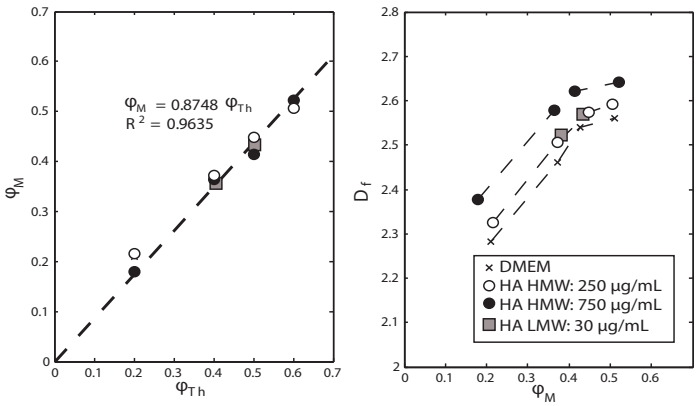

Figure 6.8: (A) Measured volume fraction as a function of the theoretical volume fraction. (B) Measured fractal dimension versus measured volume fraction.

6.4 Discussion

As mentioned in the previous chapter (see Section 5.3.2), several authors have studied the creation of fractal aggregates, and identified two different behaviors [1, 2, 5, 10, 11]. The ability of the particles to adhere and the presence of a repulsive force between them are the main parameters determining which behavior the aggregates tend to follow. If a repulsive force exists in the system, or if the particles have a lower probability to adhere to each other, the fractal dimension is generally higher [9]. As displayed in Figure 6.8-B, the measured 3D fractal dimensions when HA is added is higher than without. This indicated a reduction in the adhesion force between the cells, and thus, a reduction in the probability of two cells to adhere when in contact.

As mentioned as well in the previous chapter, the two critical shear stresses of this system evolve with the volume fraction. We now know that they evolve with HA as well. Indeed, both of these critical stresses decrease when HA is added to the suspension.

These two phenomena (increase in fractal dimension and decrease of the two critical stresses) can be explained by the adhesion of the HA molecules on the surface of the cells. The presence of HA decreases the surface available for cell-cell contact, thus lowering the magnitude of the adhesion force between each cell, reducing for example the size of the hard aggregates and increasing the fractal dimension.

Using the model explained in the previous chapter, we can plot Figure 6.9, which shows the evolution of the relative viscosity as a function of the effective volume fraction for different HA concentrations and different shear rates. The two lines represent a Krieger and Dougherty model with a maximum packing volume fraction of 0.64 for the solid line, and of 0.57 for the broken line. In the previous case (fibroblast cells without hyaluronic acid), the free parameter σ^* (which is related with the adhesion force between two cells) was calculated to be equal to 0.65 Pa, which leads to an adhesion force of around 36.5 pN. The addition of HA reduces the calculated cell-cell adhesion force to 19.7 pN and 11.3 pN for 250 µg/mL and 750 µg/mL of HA, respectively, which confirm the hypothesis that the presence of HA decreases the strength of the cell-cell adhesions.

Interestingly though, as can be seen in Figure 6.10, the data for very high shear rates (900 s^{-1}) seem to deviate from the models, following a Krieger and Dougherty model with a maximum packing volume fraction of 0.7. This can be explained by the deformability of cells, which are not absolute hard spheres. Indeed, suspended NIH-3T3 cells are more elastic spheres, with an elastic modulus of 100 Pa ± 10 Pa [12]. Their deformability at high shear rates can therefore not be neglected.

The collapse of all the curves for the different sheared configurations and the different quantities of HA used into a single master curve trend is significant, exemplifying that it is the evolution of the fractal aggregates which makes the observed flow curves different from those previously published for simple hard

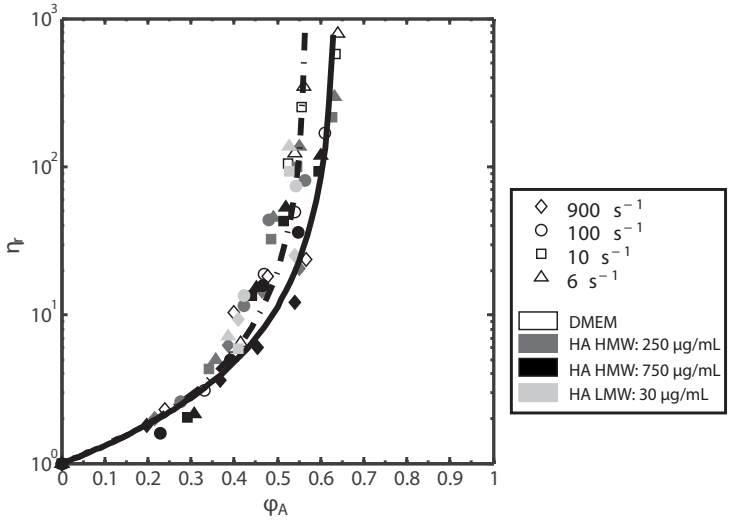

Figure 6.9: Relative viscosity as a function of the effective volume fraction for different HA concentrations and molecular weight and for different shear rates. The solid line is the Krieger and Dougherty model with $\varphi_0 = 0.64$, the broken line is the Krieger and Dougherty model with $\varphi_0 = 0.57$.

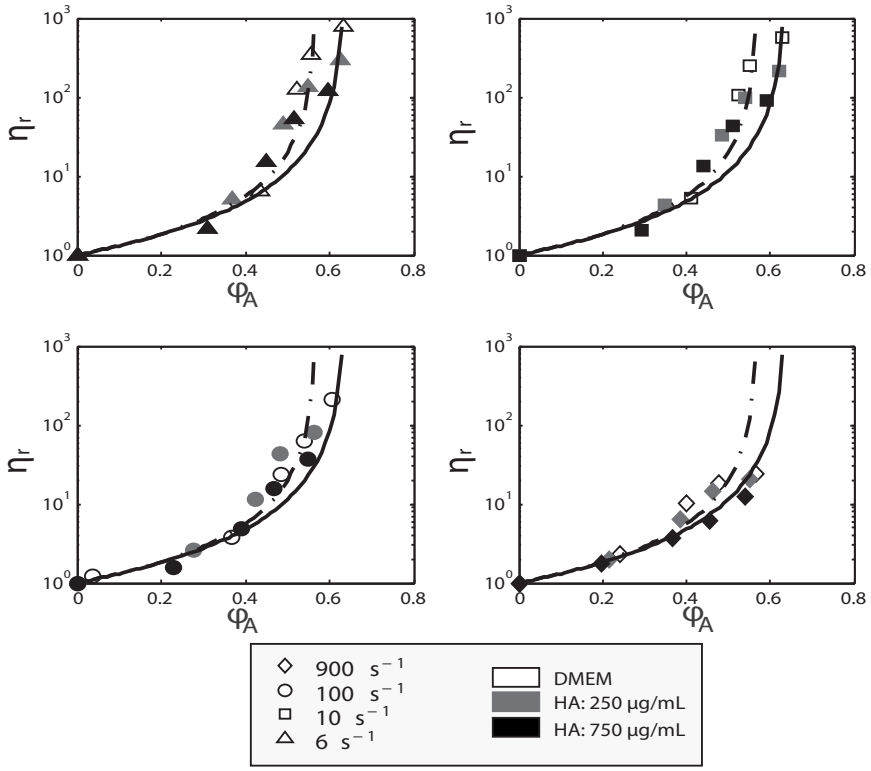

Figure 6.10: Relative viscosity as a function of the effective volume fraction for different HA concentrations and for different shear rates. The solid line is the Krieger and Dougherty model with $\varphi_0 = 0.64$, the broken line is the Krieger and Dougherty model with $\varphi_0 = 0.57$.

and non-interacting particles, and confirming our overriding hypothesis. Understanding and quantifying the links between the cells used, the biopolymer added and the shear conditions are thus essential when investigating such complex living cellular systems.

6.5 Conclusion

The introduction of macro(bio)molecules to mesenchmyal cell suspensions allowed us to interfere with cell-cell interactions, modifying the magnitude of cell-cell adhesion energies and the aggregate dynamics and thus substantially changing the rheological behavior of these living microparticulate suspensions. Importantly, we converted previously difficult-to-process high volume fraction suspensions of cells with yield stress behaviors to suspensions that simply displayed shear thinning and Newtonian-like plateaus. This customization of the flow properties of cell suspensions at high volume fractions will have impacts in several cellular engineering bioprocesses, such as monoclonal antibodies production, where difficulties establishing consistent flow fields within bioreactors and high viscosities of concentrated cell suspensions represent major limitations to throughput and quality products [4].

References

[1] D. Asnaghi. Coagulation kinetics and aggregate morphology in the intermediate regimes between diffusion-limited and reaction-limited cluster aggregation. *Phys. Rev. A*, 45(2):1018–1023, 1992.

[2] C. Cametti. Aggregation kinetics in model colloidal systems: a light scattering study. *J. Colloid Interface Sci.*, 131(2):409–422, 1988.

[3] E. Hachet, H. Van Den Berghe, E. Bayma, M.R. Block, and R. Auzely-Velty. Design of biomimetic cell-interactive substrates using hyaluronic acid hydrogels with tunable mechanical properties. *Biomacromolecules*, 13:1818–1827, 2012.

[4] B. Kelley. Very large scale monoclonal antibody purification: the case for conventional unit operations. *Biotechnol. Prog.*, 23:995–1008, 2007.

[5] M.Y. Lin, H.M. Lindsay, D.A. Weitz, P.C. Ball, R. Klein, and P. Meakin. Universality in colloid aggregation. *Nature*, 339:360–362, 1989.

[6] R. Mendichi, L. Soltes, and A.G. Schieroni. Evaluation of radius of gyration and intrinsic viscosity molar mass dependence and stiffness of hyaluronan. *Biomacromolecules*, 4:1805–1810, 2003.

[7] J. Necas, L. Bartosikova, P. Braumer, and J. Kolar. Hyaluronic acid (hyaluronan): a review. *Vet. Med. (Praha)*, 53:397–411, 2008.

[8] P. Pincus. Colloid stabilization with grafted polyelectrolytes. *Macromolecules*, 24:2912–2919, 1991.

[9] A. Thill. *Agregation des particules: structure, dynamique et simulation. Application au cas d'un ecoulement stratifie: l'estuaire du Rhone.* PhD thesis, Universite de Droit, d'Economie et des Sciences d'Aix-Marseille, 1999.

[10] D.A. Weitz and J.S. Huang. *Self-similar structures and the kinetics of aggregation of gold colloids. Kinetics of aggregation and gelation.* Elsevier Science, 1984.

[11] D.A. Weitz and M. Oliviera. Fractal structures formed by kinetic aggregation of aqueous gold colloids. *Phys. Rev. Letter*, 52(16):1433–1436, 1984.

[12] F. Wottawah, S. Schinkinger, B. Lincoln, S. Ebert, K. Müller, F. Sauer, K. Travis, and J. Guck. Characterizing single suspended cells by optorheology. *Acta Biomater.*, 1:263–271, 2005.

Chapter 7

Adding Poly(Ethylene Glycol) (PEG) to the suspension

Contents

Résumé du Chapitre

Dans ce dernier chapitre, nous étudions l'impact de l'ajout d'une molécule synthétique, i.e. non présente naturellement dans l'organisme, le polyéthylène glycol.

Les expériences sont réalisées avec trois types de polyéthylène glycol différents: PEG, PEG-NH_2 et PEG-COOH. Ceci permet d'étudier l'influence de la charge sur le comportement rhéométrique de la suspension. Plusieurs comportements complexes sont observés et sont décrits en fonction à la fois de la contrainte imposée et de la fraction volumique. L'effet de la charge est présent surtout à faible contrainte et s'estompe de plus en plus lorsque les forces hydrodynamiques augmentent. La structure de la suspension au repos est aussi étudiée pour en déduire la dimension fractale.

Différents mécanismes entrent en jeu en fonction de la fraction volumique et de la contrainte. A faible cisaillement, les mécanismes en jeu sont déterminés. A fort cisaillement par contre, plusieurs mécanismes possibles sont proposés pour expliquer le comportement surprenant de la suspension. Les conséquences de différentes hypothèses sont ensuite prises en compte dans le modèle analytique.

7.1 Introduction

The rheology of live NIH-3T3 cells in DMEM, and with an addition of an adherent biologically derived macromolecule (HA) was investigated in the previous chapters. Significant differences of behavior were witnessed, underlining the importance of investigating this kind of material in order to develop efficient bioprocesses. However, other kind of molecules can be used in these processes. In particular, the choice was made to investigate another category of biomacromolecules: synthetic biomacromolecules. These molecules are obviously not naturally present in the body, however they have received significant attention for the development of new tissue engineering scaffolds [5]. The molecule chosen for this chapter was poly(ethylene glycol) (PEG). PEG is naturally non-adherent to the cells, and can be found in a wide range of molecular weights and endgroups functionalizations. PEG has recently shown promising utility in the field of tissue engineering for two main reasons. Firstly, this polymer is relatively biologically inert and has a reduced likehood of causing any significant chronic inflammatory response [3]. Secondly, PEG molecules can be functionalized in various different ways, whether it is with proteins, peptides, growth factors or other biochemical cues affecting the interactions with cells and biomolecules [1].

7.2 Materials and Methods

All materials and methods used in this chapter are described in Chapter 4. The preparation of the cell suspension is described in Section 4.2.2. The protocol for the rheological characterisation of the suspensions is described in Section 4.3.1, and experiments were conducted with three different kinds of eight arm PEGs: PEG, PEG-NH_2 and PEG-COOH, at a concentration of $40\,\mathrm{mg}\cdot\mathrm{mL}^{-1}$. The no-slip condition was not verified experimentally for these systems, however, because of the there was no slippage in the other systems, the no-slip condition was supposed to be fulfilled here as well. The main difference between the three molecules is their charge, as they are all 8-armed PEG of molecular weight of 40kDa. The two-photon microscopy protocol and analysis methods are detailed in Section 4.6.2 to 4.6.5.

7.3 Results

7.3.1 Rheology of cell suspensions with different PEG types

The addition of biomacromolecules in the suspension influences the rheology of the system. In Chapter 6, the impact of the addition of an adherent biomacromolecule was investigated, and showed that the ability of some biomacromolecules to adhere onto the surface of cells significantly modifies the rheological footprint of cell suspensions. Other kinds of biomacromolecules used in tissue engineering, such as PEG, can not adhere to cell surface. Although, their addition to cell suspensions still modify the rheology of the material, as depicted in Figure 7.1.

According to the charge of the 8 armed PEG molecule, the effects seem to vary greatly. These effects also seem to evolve with both the shear and the volume fraction. Some of the features of these curves are similar to those observed with the HA systems, such as yield stress behavior, shear thinning, viscosity failure and a Newtonian-like plateau. In order to discuss these complex behaviors; we will discuss behaviors as a function of shear stress.

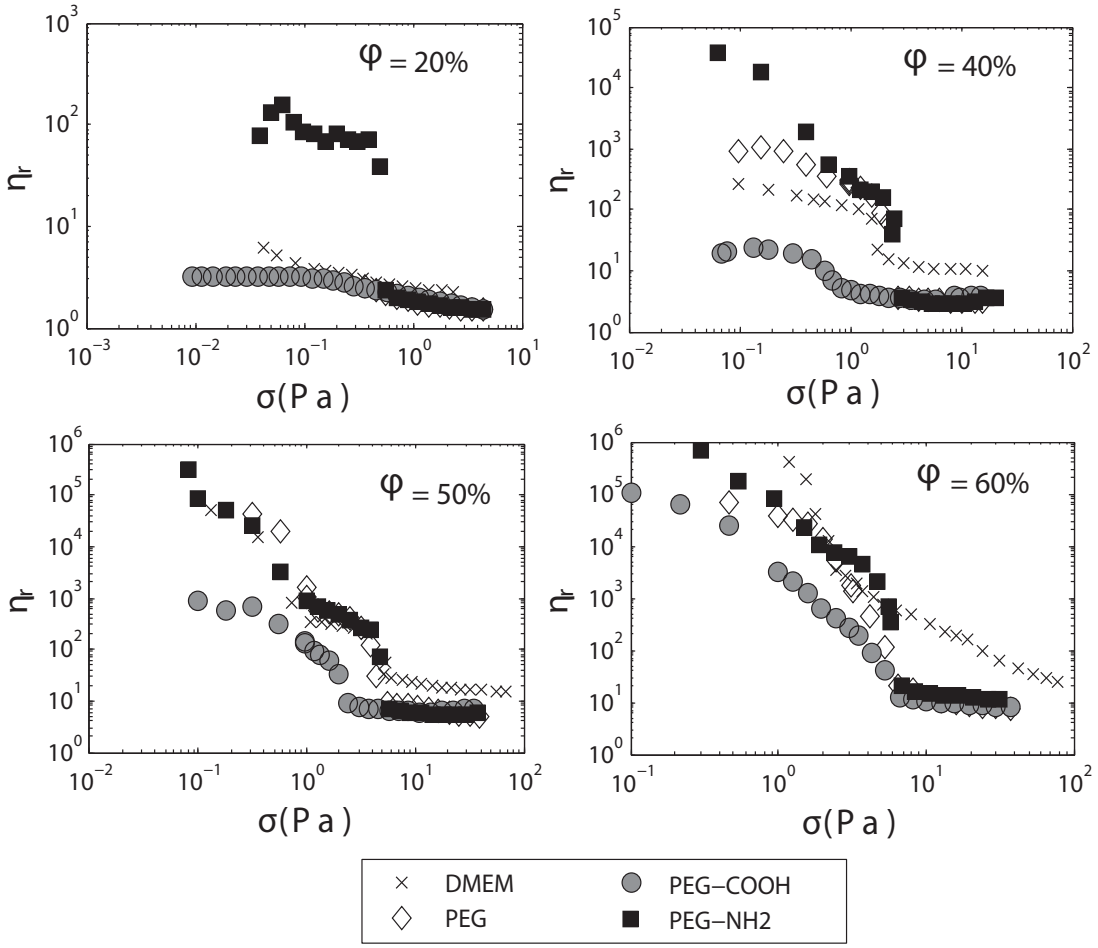

Figure 7.1: Relative viscosity as a function of shear stress for different PEG molecules at different volume fractions.

7.3.1.1 Low shear stresses (prior to the viscosity decrease)

For low shear stresses (below the critical stress at which the viscosity decreases drastically), the difference in behavior between the different kinds of PEG is very noticeable, especially when PEG-NH_2 is used. Indeed, at the lowest volume fraction used (20%), the relative viscosity measured at small shear for the suspension with PEG-NH_2 is roughly thirty times higher than any other system studied (DMEM, PEG, PEG-COOH). This tendency to increase the relative viscosity with the addition of PEG-NH_2 is also witnessed for a volume fraction of 40%, through the increase of the yield stress behavior for the lowest shear stresses tested. Interestingly though, for higher volume fractions (at least 50%), the relative viscosity of the PEG-NH_2 system at low shear stresses seems to more or less match the behavior of the suspension with only DMEM. At a volume fraction of 60%, the yield stress is lower than with the DMEM only system.

Focusing now on the PEG-COOH, the relative viscosity of this system is significantly lower than the suspension with only DMEM at volume fractions of 40%, 50% and 60%. This is less obvious at a volume fraction of 20%, except at shear stresses below 0.1 Pa. At very low shear stresses, the yield stress behavior is very nearly removed at volume fractions of both 40% and 50%. At 60%, a yield stress trend is still visible, but significantly attenuated.

The effect of the addition of PEG (without the NH_2 or the COOH groups) is different again. The relative viscosity at low shear stresses is slightly higher than that of DMEM only, but not as high as with PEG-NH_2 at a volume fraction of 40%. For a volume fraction of 50%, the relative viscosity of the suspension with PEG seems to be similar to the one of the DMEM. At 60%, the value of the relative viscosity of the PEG system at low shear stresses is lower than with DMEM only, and of magnitude similar to the PEG-NH_2 system.

From the analysis of the different systems used, it appears that several mechanisms are influencing the rheology of the suspension. At low shear stresses, these mechanisms are obviously linked with the charge of the molecules used and evolve with the volume fraction. For PEG and PEG-NH_2 particularly, the effects seem to vanish as the cell concentration approaches 60%.

7.3.1.2 Intermediate shear stresses (at the viscosity decrease)

For volume fractions of 40% and 50%, the use of PEG-COOH significantly decreases the critical shear stress at which the viscosity drastically decreases. At 60%, it is hard to define a critical shear stress though, as no abrupt change of slope in the relative viscosity profile is witnessed. The relative viscosity at volume fraction of 40% and higher is however clearly lower than of DMEM, PEG or PEG-NH_2 systems.

The behaviors of PEG-NH_2 and PEG are however slightly different. For a volume fraction of 40%, it seems that the critical shear stress for each of these suspensions is very similar and slightly higher than for the suspension with DMEM only. The relative viscosities of the PEG and the PEG-NH_2 systems are very

similar, but higher than of DMEM only. At $\varphi = 50\%$ though, the critical shear stress is the same for the PEG, the PEG-NH_2 and the DMEM systems, and the relative viscosities of these three systems are highly similar. At a volume fraction of 60% however, the critical shear stress for the PEG system is lower than of the PEG-NH_2 system. As no sharp change in viscosity is observed in the case of DMEM alone, it is unclear as if the critical shear stress for DMEM alone is higher or lower than of PEG or PEG-NH_2.

7.3.1.3 Higher shear stresses (after the viscosity decrease)

After the rapid decrease in viscosity, there are very little differences between the PEG, the PEG-COOH and the PEG-NH2 systems, regardless of the volume fractions. The three systems exhibit a Newtonian-like plateau of similar relative viscosity. Interestingly, the relative viscosity of these systems is always lower than of the DMEM alone system, again, regardless of volume fraction. The overlay of the three different kind of PEG at high shear stresses indicates that this trend is independent of the charge of the molecule, and therefore is only induced by the presence of the PEG molecules in the suspension.

7.3.2 Measurement of the fractal dimension of the suspension with the different types of PEG molecules

The fractal dimension in 3D was measured for these systems, using the previously detailed method (see Section 4.6.5), as depicted in Figure 7.2. The addition of PEG in the suspension, whatever its charge, decreases the fractal dimension. This trend is seen at any volume fraction. This results suggests that the aggregates are more porous than in the suspension without PEG. Focusing on the different PEG molecules, it appears that the PEG-COOH system is the one that has the higher fractal dimension of the three types of PEG used. The addition of PEG and PEG-NH_2 decreases the fractal dimension even more, but intriguingly, considering the significant differences in their rheological behavior, no definite distinction can be made between the two.

7.4 Discussion

A common phenomenon occurring when ungrafted molecules are added to a suspension is depletion, as discussed previously in Section 2.5.4. Through the creation of concentration gradients of the molecule added, the overall impact on the suspension can be seen as the addition of an attractive force to the system. It is seen as an attractive force because the particles of the suspension will tend to be pushed together, with the molecules being excluded from the space between some of the particles, creating a concentration gradient and thus changing the osmotic pressure locally within the material.

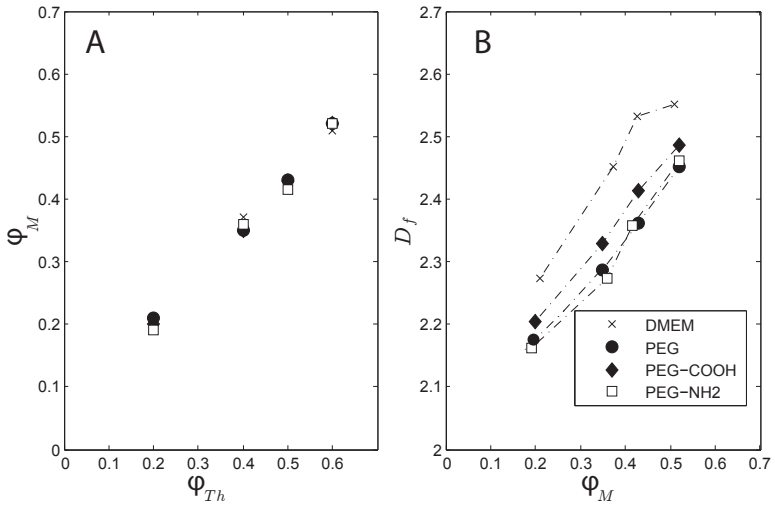

Figure 7.2: (A) Measured volume fraction as a function of the theoretical volume fraction. (B) Measured fractal dimension versus measured volume fraction.

PEG is a synthetic biomacromolecule, which is not naturally present in the body. No specific PEG receptors are known to exist on the surface of cells, thus it is highly likely that the PEG molecules do not adhere through specific receptors onto the cells. However, in the case of PEG-NH_2 or PEG-COOH, the charge of the NH_2 or the COOH group could indeed change this behavior, but this will be discussed later. Focusing on the PEG alone, signs characteristic of depletion behavior can be observed in Figure 7.1 at a volume fraction of 40%, for shear stresses ranging from low to intermediate (up to the abrupt viscosity decrease) included. Indeed, depletion will push the cells together, thus favoring the creation of a weak network and increasing the shear viscosity at low shear. However, once in contact, the adhesion strength between the cells is similar to the case of DMEM alone, as the same set of surface receptors are available. With the adhesion strength expected to be similar to the DMEM system, the critical shear stress (σ^*) should thus be similar as well, as confirmed in Figure 7.1 for volume fraction of 40% and 50%. At volume fractions of 50% and 60%, the low shear relative viscosity of the PEG system is very similar to that measured in the DMEM system. This can be explained by the fact that at these higher volume fractions, the cells are already in contact with each other, and therefore, depletion obviously does not play any major role. The behavior at higher shear will be discussed later.

As mentioned above, the charge of the PEG molecules used, through non specific charge-charge interactions may also change the flow behavior of the studied system. It is quite difficult to quantitatively know the charge of a cell. Indeed, both cationic and anionic functional groups contained in the lipid head-groups contribute to the net electric field at membrane surfaces [2]. Moreover, cell surfaces are decorated with transmembrane proteins, and also have bound extracellular matrix (ECM) proteins and fragments even after the trypsinization (as described in the cell culture methodology, see Section 4.2.1), influencing the

overall charge of the cell. The negative charge of many ECM molecules and most proteins on the cellular surface lead us to assume that these cells studied are negatively charged particles [2, 7].

Applying this insight to the data from Figure 7.1, it is possible to propose a mechanism for the influence of the charge of our polymer system on cell suspension behaviors, and therefore to understand and explain the different behavior witnessed for the PEG-NH_2 and the PEG-COOH addition. Under the pH condition tested, it is highly likely that the NH_2 group becomes a NH_3^+ group (pKa > 8 according to [4] and pKa > 9 according to [6]), and therefore is charged positively, and that the COOH group becomes a COO^- group (pKa < 5 [6]), and therefore is charged negatively.

With the surface of the cells assumed to be mainly electronegative, the charge of the NH_3^+ end group on the PEG could counteract the effects of depletion. At a volume fraction of 40%, the low shear relative viscosity is thus even higher than the one of the neutral PEG system. The yield stress is higher as well, showing an increase in network connectivity compare with the PEG system. Focusing more on the results at a volume fraction 20%, the noticeable increase in relative viscosity at low shear confirms this mechanism. Indeed, in a system where the concentration in cell would not high enough to create a network, the attraction forces between the added molecules and the cells act like an attractive force between the cells, and thus induce the creation of this weak network. At 50 and 60%, there are so many cells in the system that the impact of PEG-NH_2 is very limited, as for the neutral PEG system. The shear induced breakdown also happens at a similar critical shear stress, as this kind of PEG does not change the set of receptors used to create adhesion between the cells, but only creates weak contacts between the loose protein network on the outer periphery of the cells.

The case of the PEG-COOH system is different, but at least as interesting. Keeping in mind that a cell is globally negatively charged, a negatively charge group should therefore be repulsed by the cell surface. In this case, the adhesion strength between the cells should be reduced, as the negatively charged molecules would increase the depletion and thus prevent the formation of a network. This would induce a lower critical stress, as well as a lower relative viscosity. Looking at the Figure 7.1, it appears that indeed, the relative viscosity of the cells with PEG-COOH system is significantly lower than the DMEM system. The critical shear stress is also reduced, and the yield stress is significantly reduced or absent. The fractal dimension also shows the smallest change for all PEG systems (see Figure 7.2), suggesting that whilst depletion may be substantial, there are some structural rearrangements as a result of this negatively charge PEG that differ from the PEG and the PEG-NH_2.

Another assumption would be that short range interactions could occur between the positively charge cell surface bound proteins (or positively charged domains thereof) and the PEG-COOH molecules. This is definitely possible if the difference of size between the cells and the PEG molecules are taken into consideration. This would allow the polymer to bind within the extracellular

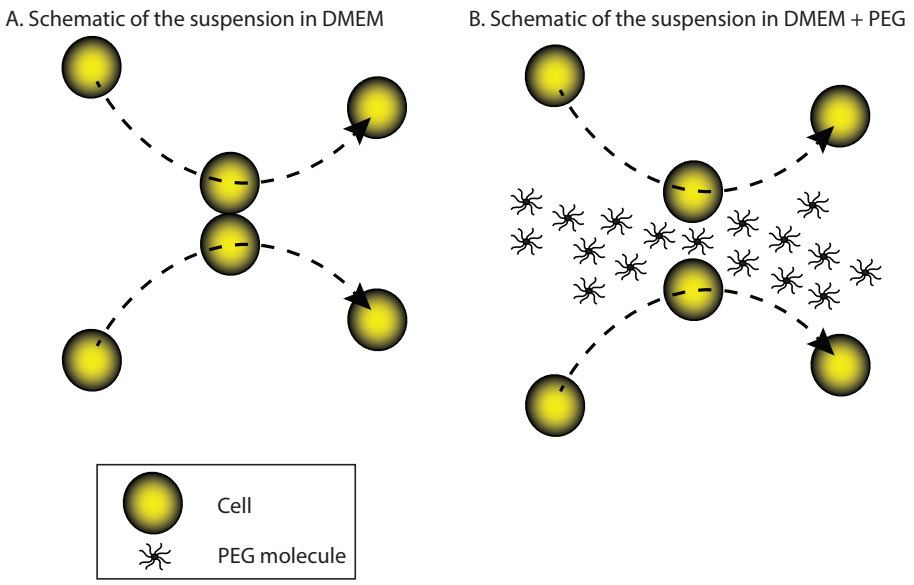

Figure 7.3: (A) Schematic of the suspension in DMEM alone, at shear stresses higher than the critical shear stress. (B) Schematic of the suspension in DMEM + PEG, at shear stresses higher than the critical shear stress.

protein layer, whilst not connecting explicitly to the cells. These interactions would be short range and diffuse within the cell surface bound protein layer. These bindings would increase the density of the cell protein coat, obscure the cell surface receptors involved in cellular adhesion and hence reduce cell-cell adhesion strength. Aggregates would thus still be able to be created and would be denser than the one created in presence of the other kind of PEG molecules, as confirmed by the values of the fractal dimension for the PEG-COOH system being slightly higher than for the PEG and the PEG-NH_2 systems. Even though, the exact mechanism remains to be precisely elucidated through complementary experiments.

When the shear stress is higher than the critical shear stress, another mechanism seems to be at play. Indeed, the relative viscosities of the three PEG systems collapsed on to one another, and are lower than the relative viscosity of the cell suspension with just DMEM. As discussed above, the different types of PEG molecules have different impacts on the rheology of the suspension, according to their charge and therefore according to how they interact with the cells. Because of this collapse at higher shear stresses, this mechanism appears to be independent of the charge, and therefore can be imputed to the presence of the PEG molecules alone. It is likely that the presence of the PEG molecules in some way reduces the transient contacts between cells that occur when the suspension is sheared (see schematic in Figure 7.3), acting like a lubricant to the system.

Using the set of equations mentioned in Chapter 5, a mastercurve-like plot can again be created, see Figure 7.4. The values of σ^* for the systems with DMEM, PEG and PEG-NH_2 were taken equal to 0.65 Pa, as the critical shear stress for the viscosity drop is roughly equal for these three systems. For the

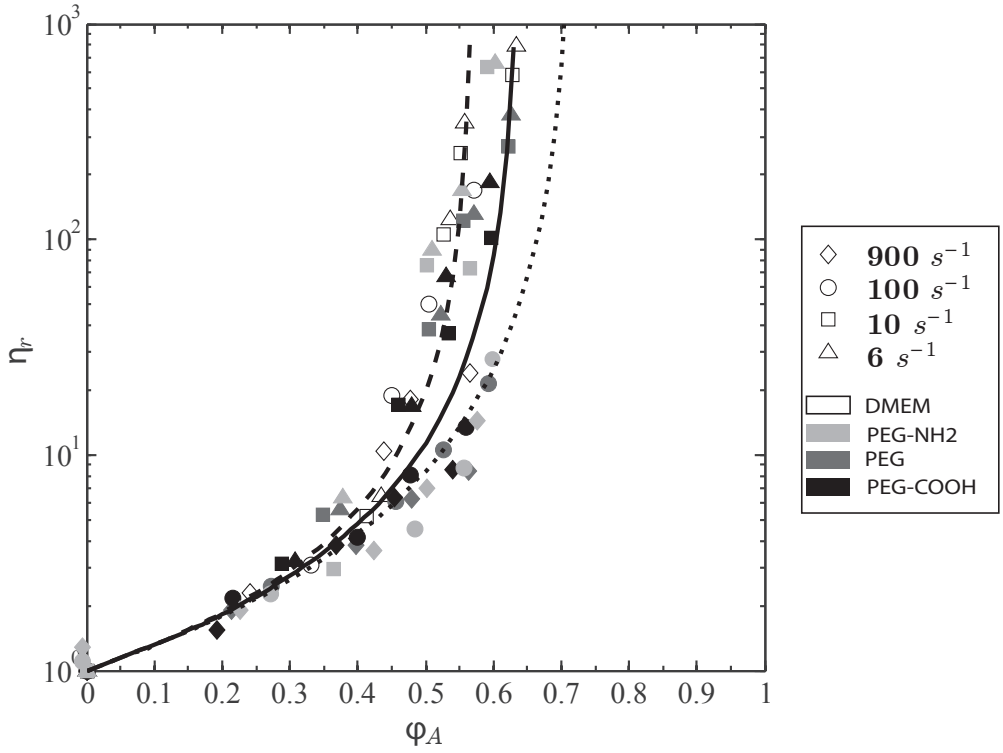

Figure 7.4: Relative viscosity as a function of the effective volume fraction for different PEG molecules and for different shear rates. The solid line is the Krieger and Dougherty model with $\varphi_0 = 0.64$, the broken line is the Krieger and Dougherty model with $\varphi_0 = 0.57$ and the dotted line is the Krieger and Dougherty model with $\varphi_0 = 0.72$.

PEG-COOH system however, σ^* had to be taken equal to 0.05 Pa in order to achieve the collapse of the curves, indicating an adhesion strength of 2.81 pN. The same considerations as utilised in the previous chapters were taken for the parameter m, and the values of the fractal dimensions were the ones measured from the two-photon microscope's images for each PEG system. Interestingly, the data at the highest shear stresses do not seem to collapse on the Krieger-Dougherty model with $\varphi_0 = 0.64$, but onto one with $\varphi_0 = 0.72$. As discussed previously, a part of this deviation is likely due to the deformability of the cells. However this deviation is stronger in the case of the PEG systems, indicating that another contribution may come from a difference in the microscopic arrangement of the suspensions and of the molecules under such shearing conditions.

Previously, it was assumed that the presence of PEG molecules in such concentrations prevented the brief adhesion between neighbouring cells under high shear, explaining the low relative viscosity. Indeed, when σ^* is taken to equal to 0 for shear stresses higher than the intermediate range (i.e. past the abrupt decrease in viscosity) for the PEG systems, the data collapse once more on the Krieger-Dougherty model with $\varphi_0 = 0.64$, as displayed in Figure 7.5. Even if the collapse looks correct, having an adhesion force strictly equal to 0 hardly makes any real physical sense. It is therefore difficult to confirm the hypothesis made, as both a change in adhesion strength and/or a change in the microscopic conformation may be the origin of the differences observed between the PEG systems and the DMEM, especially when taking into account that a change in adhesion force often leads to a different microscopic re-organization.

7.5 Conclusion

The described set of experiments have shown that adding biomacromolecules having no specific interaction domains for cell surface receptors to a cell suspension can still have a drastic impact on the rheology of such materials. In addition of the complex behaviors associated with using live cells suspensions, other phenomena appear to take place at different shear stresses: depletion at low shear and drastic microscopic re-organization at high shear. According to the charge of the chosen molecules, the mechanical properties of the suspension at low shear stresses can be modified significantly, either increasing or attenuating/removing the yield stress behavior. At high shear stresses, however, it appears that the charge of the chosen molecule does not matter. These insights into the rheology of live cells suspensions in the presence of non-adherent biomacromolecules often used in hydrogel formulations are central to the up-scaling of tissue engineering bioprocesses such as producing scaffolds seeded with cells, whether it is as a bulk injectable material or in a microfluidic device.

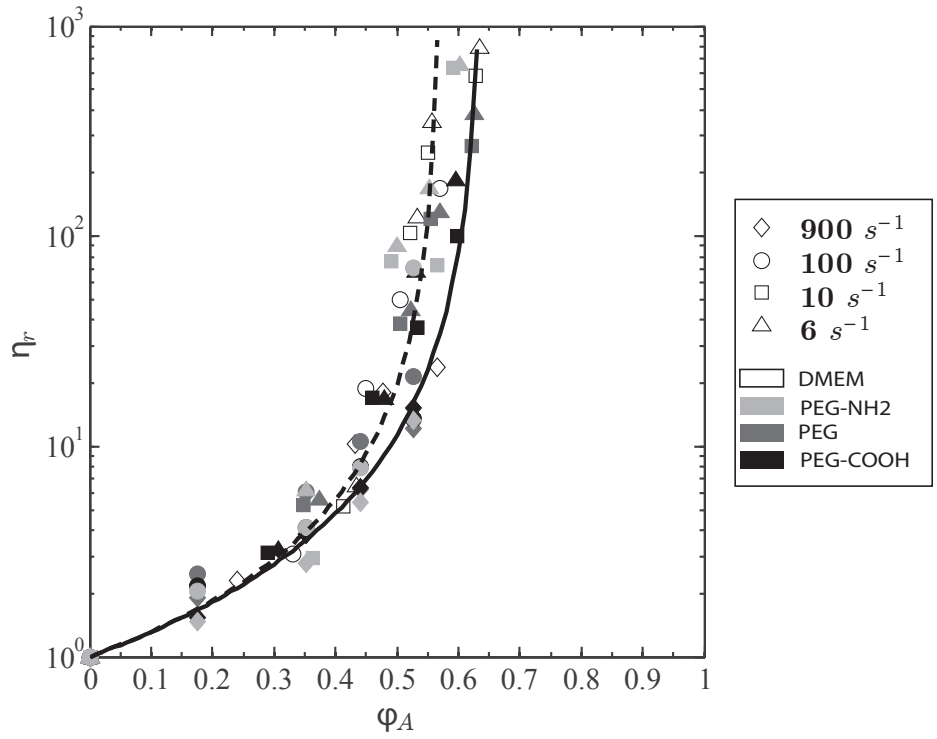

Figure 7.5: Relative viscosity as a function of the effective volume fraction for different PEG molecules and for different shear rates, but with the value of σ^* equal to 0 for the PEG systems for shear higher than the drop in viscosity. The solid line is the Krieger and Dougherty model with $\varphi_0 = 0.64$, the broken line is the Krieger and Dougherty model with $\varphi_0 = 0.57$.

References

[1] S.A. DeLong, A.S. Gobin, and J.L. West. Covalent immobilization of {RGDS} on hydrogel surfaces to direct cell alignment and migration. *Journal of Controlled Release*, 109:139 – 148, 2005.

[2] N.M. Goldenberg and B.E. Steinberg. Surface charge: A key determinant of protein localization and function. *Cancer Research*, 70:1277 – 1280, 2010.

[3] C.B. Hutson, J.W. Nichol, H. Aubin, H. Bae, S. Yamanlar, S. Al-Haque, S.T. Koshy, and A. Khademhosseini. Synthesis and characterization of tunable poly(ethylene glycol): Gelatin methacrylate composite hydrogels. *Tissue Eng. Part A*, 17:1713 – 1723, 2011.

[4] O.B. Kinstler, D.N. Brems, S.L. Lauren, A.G. Paige, J.B. Hamburger, and M.J. Treuheit. Characterization and stability of n-terminally pegylated rhg-csf. *Pharmaceutical Research*, 13(7):996–1002, 1996.

[5] D.J. Menzies, A. Cameron, T. Munro, E. Wolvetang, L. Grondahl, and J.J. Cooper-White. Tailorable cell culture platforms from enzymatically cross-linked multifunctional poly(ethylene glycol)-based hydrogels. *Biomacromolecules*, 14(2):413–423, 2013.

[6] J.P. Ryman-Rasmussen, J.E. Riviere, and N.A. Monteiro-Riviere. Penetration of intact skin by quantum dots with diverse physicochemical properties. *Toxicological Sciences*, 91(1):159 – 165, 2006.

[7] L. Sorokin. The impact of the extracellular matrix on inflammation. *Nature Reviews Immunology*, 10:712 – 723, 2010.

General Conclusion

In this piece of work, we investigated the rheology of live mesenchymal cell suspensions. The cells chosen were mouse NIH-3T3, suspended in their culture medium without serum. Unlike most suspension studies dealing with synthetic or natural particles (non-living) systems, live cells suspensions have an inherent variability in shape, size and behaviour over time, for example with cell binding or adhering to each other dynamically, creating complex living structures. When combined with the difficulty of culturing enough cells for such tests and keeping them viable during applicable testing time-frames, it may explain why this research topic has received very little attention.

Several experimental techniques were used to study this system. The mechanical properties of this system were investigated through rheometry, whereas the structure of the suspension at rest was studied using conventional (2D) and two-photon (3D) microscopy. Flow cytometry, as well as confocal microscopy were used to assure the presence of one of the biomacromolecules investigated (HA) on the cell surface, as well as the presence of some specific cell surface receptors.

In the first study, we investigated the rheological behaviour of 3T3s cells in Dulbecco's Modified Eagle's Medium (DMEM).

The results discussed in this chapter showed that this system displays complex rheological behaviours, depending on both the shear applied and the volume fraction of cells. Indeed, as the volume fraction increased, the suspension exhibited a yield stress behaviour, followed by strong shear thinning, until a Newtonian-like plateau was reached. When the shear stress was increased further, the viscosity dropped drastically to another Newtonian-like plateau. The fractal dimension of the network made by the cells at rest was investigated using conventional phase contrast (2D) and two-photon (3D) microscopy. Using a simple analytical model, the evolution of the viscosity for different shear stresses as a function of the effective volume fraction were all collapsed with a mastercurve, confirming that the evolution of the viscosity with both parameters was mainly caused by the evolution of the network built by the cells, as well as the size of the cell aggregates. Last but not least, the use of this analytical model enabled us to determine the adhesion strength between the cells.

The second part of our study concerned the addition of a biomacromolecule naturally present in tissues and often used in hydrogels for tissue engineering applications (hyaluronic acid) to the cell suspension. The impact of the

addition of hyaluronic acid on the flow properties were investigated with techniques similar those already described in Chapter 4 and used in Chapter 5.

In this chapter, we showed that NIH-3T3 cells had several kinds of surface receptors specific to hyaluronic acid. These receptors had the ability to bind the hyaluronic acid when in the media. By functionalising hyaluronic acid with a fluorescent dye, the presence of hyaluronic acid molecules bound to the cells was confirmed using confocal microscopy. The impacts of several concentrations of hyaluronic acid, as well as several molecular weights on the flow behaviour of the suspension were thereafter being observed in terms of biomacromolecule molecular weight. The highest concentration of the higher molecular weight tested changed the rheology the most with a distinct impact. The yield stress behaviour was significantly decreased, as was the extent of shear thinning, along with the relative viscosity of the suspension. The sharp viscosity drop was softened and occurred at lower shear stresses. These results suggested a decrease in network strength, a proposition that was confirmed through our observation of an increase in the fractal dimension of the network made by the cells at rest when hyaluronic acid was added, meaning that the network was also less porous. Using the same analytical model as described in Chapter 5, it was possible to have the data for the relative viscosity for different shear stresses as a function of the effective volume fraction collapsed on the same mastercurve as for the cell suspension without hyaluronic acid. Through this model, the adhesion strength between two cells across a population of millions was estimated and was shown to be significantly lower than the suspension without hyaluronic acid. It was thus hypothetised that the presence of hyaluronic acid on the surface of the cells effectively screened the surface receptors normally used by the cells in cell-cell adhesion, and therefore decreased the number of available adhesion points.

The final part of this study aimed to characterize the impact of the addition of a synthetic biomacromolecule on the rheology of the suspension. The chosen molecule was 8 armed polyethylene glycol (PEG). PEG is a widely used biomacromolecule for tissue engineering and regenerative medicine application. The fact that it is relatively biologically inert, and the possibility to functionalize it with a wide range of molecules (proteins, growth factor...) make it a promising choice for the formulation of hydrogels. With PEG having no known specific cell surface receptors, we chose to investigate three different kind of PEG molecules in order to study the effects of the charge of the chain end group (-OH (no charge), -COOH (electronegative) and -NH_2 (electropositive)) on the behaviour of the suspension.

The earlier results from the study of the NIH-3T3 cell suspension in DMEM allowed us to define a reference system, from which the differences caused by the presence of the PEG molecules, as well as their charge, were investigated. Symptoms of depletion were observed for the PEG and PEG-COOH. PEG-NH_2 had a drastic impact on the rheology of the suspension, increasing significantly the yield stress behaviour. Interestingly, the addition of either PEG or PEG-NH_2 molecules were not observed to change the critical shear stress at which the viscosity rapidly decreased. PEG-COOH had a very different impact, decreas-

ing the relative viscosity, the yield stress behaviour, as well as the critical shear stress. This was proposed to be related to the fact that cells are mainly negatively charged, as is the PEG-COOH. The PEG-COOH molecules seem to prevent the formation of the network. Another assumption would be that short range interactions could occur between the positively charge cell surface bound proteins (or positively charged domains thereof) and the PEG-COO^-, thus allowing the polymer to bind within the extracellular protein layer, whilst not connecting explicitly to the cells. These interactions would be short range and diffuse within the cell surface bound protein layer. This would increase the density of the cell protein coat, obscure the cell surface receptors involved in cellular adhesion and hence reduce cell-cell adhesion strength, acting in a similar way as the hyaluronic acid, only less efficiently, as they lack the specificity of interaction through defined cell surface receptors. However, the exact mechanism still remain to be precisely elucidated.

A very peculiar behaviour was observed for shear stresses higher than the critical shear stress: the relative viscosity for the three different kinds of PEG molecules used all collapsed onto one another at a given volume fraction, indicating that in this shear regime, the charge of the molecules used had no impact on the rheology of the suspension. The analytical model discussed in the previous chapters was used in two different ways, according to the assumption made on the reasoning for this collapse at high shear, indicating that even if the reasons for the collapse at high shear were not clear, microscopic reorganisation of the suspension was the origin of this behaviour.

The output of this study allows researcher to take into consideration the complex rheological footprint of cell suspensions when either planning their experiments or developing new methods for tissue engineering or cellular therapy. The impacts of the addition of biomacromolecules on the mechanical properties of the cell suspensions is also an important consideration when formulating hydrogels for tissue engineering applications, either for a bulk injectable system or for a microfluidic application.

Future work to continue this project could take several directions. One of it would be the use of different polymers, and/or of different cell lines. This would allow, one to study another applied system, but also to add data to the existing database in order to try and understand more in depth if a single theory for cell suspensions could be derived. This could then allow one to predict engineering problems that would occur while the processes are up-scaled. A study focussing on the same system but with a wider range of concentration and molecular weight of the chosen polymer could also be useful, especially for the PEG based systems, to either validate our hypothesis or to formulate a new one. Another direction would be to develop a method to be able to investigate the rheology of cell suspensions and image the suspension at the same time. Being able to follow what is happening within the suspension visually would give precious insights for the understanding of the mechanisms of such complex materials. Another way to get useful data would be to focus on the time response of the suspension, during or post removal of controlled step stresses. In the experiments described

in this thesis, the time response of the suspension to the applied stress was always recorded but not thoroughly exploited.

Conclusion Générale

Au cours de ce travail de recherche, nous avons étudié la rhéologie de cellules mésenchymateuses vivantes en suspension. Les cellules choisies étaient des NIH-3T3 de souris, avec leur média de culture sans sérum comme fluide suspendant. Au contraire de beaucoup d'autres systèmes étudiés, les suspensions de cellules vivantes ont une grande variabilité en forme, taille et comportement. De plus, les mécanismes très dynamiques de contacts entre les cellules conduisent à la formation de structures complexes. Ceci, ajouté à la difficulté d'avoir accès à suffisamment de cellules, peut expliquer pourquoi ce sujet de recherche n'a reçu que peu d'attention.

Plusieurs techniques expérimentales ont été utilisées pour étudier ce système. Les propriétés mécaniques ont été mesurées à l'aide d'un rhéomètre, tandis que la structure de la suspension au repos a été analysée grâce à un microscope classique (2D) bi-photonique (3D). La présence à la fois des polymères ajoutés et des récepteurs surfaciques d'intérêt ont été vérifié à l'aide d'imagerie confocal et de cytométrie de flux.

Dans la première partie de notre étude, nous nous sommes intéressés au comportement rhéologique de cellules 3T3 en suspension dans leur média de culture sans sérum (Dulbecco's Modified Eagle's Medium (DMEM) high glucose).

Les résultats discutés dans le chapitre correspondant montrent une signature rhéologique complexe, dépendant à la fois de la contrainte appliquée et de la fraction volumique. En effet, lorsque la fraction volumique augmente, la suspension commence à se comporter comme un fluide à seuil, suivi d'une forte tendance rhéofluidifiante, jusqu'à ce qu'un plateau quasi-Newtonien soit atteint. Quand la contrainte augmente encore, la viscosité chute subitement jusqu'à un second plateau. La dimension fractale du réseau créé par les cellules au repos a été explorée grâce à un microscope bi-photonique. En utilisant un modèle analytique simple, il a été possible de rassembler les évolutions de la viscosité à différent taux de cisaillement en fonction de la fraction volumique effective sur une même courbe maitresse. Ceci a permis de mettre en évidence que l'évolution des propriétés en écoulement de notre matériau était due à des réarrangements microscopiques du réseau et des agrégats formés par les cellules. Enfin, l'utilisation de ce modèle analytique nous a permis de déterminer la force d'adhésion entre les cellules et de la comparer à celle reportée dans la littérature.

La seconde partie de notre étude a porté sur l'ajout dans la suspension d'une macromolécule naturellement présente dans notre corps: l'acide hyaluronique.

L'impact de l'ajout d'acide hyaluronique sur les propriétés en écoulement du matériau a été étudié à l'aide de techniques similaires à celles décrites précédemment.

Dans le chapitre correspondant, nous avons montré que les cellules utilisées possédaient plusieurs types de récepteurs à leur surface spécifique à l'acide hyaluronique. Ces récepteurs ont la particularité de permettre à la cellule de s'accrocher et de se lier avec des molécules d'acide hyaluronique. Après avoir fonctionnalisé des molécules d'acide hyaluronique avec des fluorophores, la présence d'acide hyaluronique à la surface des cellules a été confirmée par microscopie confocal. L'impact de la concentration, ainsi que de la masse moléculaire de la molécule utilisée ont été explorés. La plus haute concentration de molécules avec la plus haute masse moléculaire est la condition qui modifie le plus les propriétés rhéologiques du matériau. Les tendances de comportement comme un fluide comportant une contrainte seuil et rhéofluidifiante sont atténuées. La viscosité relative est donc fortement réduite. La chute brutale en viscosité se produit à une contrainte plus basse, et de manière plus douce. La dimension fractale a été mesurée comme étant plus haute avec l'acide hyaluronique, indiquant une structure moins poreuse. En utilisant le même modèle analytique, les données de ces expériences ont pu être réunies sur la même courbe maitresse que celle utilisée lors de l'analyse des résultat du chapitre précédent. De part ce modèle, l'énergie d'adhésion entre les cellules a pu être estimé comme étant significativement inférieure à celle du système sans acide hyaluronique. La présence d'acide hyaluronique à la surface des cellules empêche l'utilisation d'une partie des récepteurs recrutés pour l'adhésion cellule-cellule, et ainsi fragilise le réseau.

La dernière partie de notre étude a été focalisé sur l'étude de l'impact de l'ajout d'un molécule synthétique sur le comportement de la suspension. La molécule choisie a été le polyéthylène glycol (PEG). Le PEG est une macromolécule fréquemment utilisée en ingénierie tissulaire et en médecine régénérative, principalement à cause de sa bonne bio-compatibilité et de l'aisance à le fonctionnaliser. Trois types de molécules de PEG avec des groupes de fin de chaines (-OH (neutre), -COOH (électronégatif) et -NH_2 (électropositif)) ont été utilisés de manière à pouvoir observer l'influence de la charge sur la rhéologie de la suspension.

Les résultats de l'étude des suspensions de NIH-3T3 dans le DMEM ont permis la définition d'un système de référence, par rapport auquel les effets des différentes charges ont pu être comparés. Des signes de déplétions ont été observés lorsque du PEG et du PEG-COOH ont été ajoutés à la suspension. Le PEG-NH_2 en particulier modifie grandement les propriétés en écoulement de la suspension en augmentant la contrainte seuil. La valeur critique de chute de viscosité ne semble pas être modifiée par contre. L'impact du PEG-COOH est très différent, réduisant la viscosité relative de la suspension, le comportement de fluide à seuil ainsi que la contrainte critique à laquelle la viscosité chute brutalement. Une explication, basée sur l'électronégativité à la fois des molécules de PEG-COOH, mais aussi des cellules. Une autre explication proposée est basée sur l'interaction entre les domaines électropositifs de certaines protéines à la surface des cellules et

les molécules de PEG-COOH. Dans cette optique, les molécules de PEG-COOH masqueraient certains des récepteurs responsables de l'adhésion cellulaire, et de ce fait réduiraient la force d'adhésion entre les cellules, agissant de manière semblable aux molécules d'acide hyaluronique, mais moins efficacement puisque non accrochées directement aux cellules. Le mécanisme exacte est néanmoins toujours à étudier pour pouvoir conclure de manière définitive.

Un comportement particulier a été observé pour des contraintes plus grandes que la contrainte critique: la viscosité relative des trois systèmes à une fraction volumique donnée est similaire, indiquant que dans ce régime hydrodynamique, la charge n'a plus d'effet sur la suspension. Le modèle analytique des chapitres précédents a aussi été utilisé, mais de deux façons différentes, selon l'hypothèse choisie pour expliquer cette indépendance de la charge. Ceci nous permet donc de conclure que même si les raisons de ce comportement ne sont pas encore claires, c'est une réorganisation microscopique de la suspension et de ses agrégats qui est à l'origine des comportements observés.

Les résultats de cette étude permettent aux chercheurs de prendre en considération la complexité de la rhéologie des suspensions de cellules lorsqu'ils planifient des expériences ou développent de nouvelles méthodes dans les domaines de l'ingénierie tissulaire et des thérapies cellulaires. Les impacts de l'addition de biomacromolécules sur les propriétés mécaniques des suspensions de cellules sont aussi de première importance lorsqu'une formulation d'hydrogel est mise au point, que ce soit pour être utilisé comme un système injectable ou en microfluidique.

Les travaux possibles pour continuer ce projet peuvent prendre plusieurs directions. L'une d'entre elles serait de continuer les mêmes types d'expériences avec différents polymères et d'autres types de cellules. Ceci permettrait d'étudier un système différent mais aussi d'avoir d'avantage de données pour comprendre plus en détail les mécanismes en jeu, ainsi que de se rapprocher d'un modèle unique pour les suspensions cellulaires. Une étude se focalisant sur les mêmes systèmes, mais avec de plus grandes variations de concentrations et de poids moléculaires pourrait aussi être utile, en particulier en ce qui concerne le PEG, pour soit valider nos hypothèses ou en proposer des nouvelles. Une autre direction serait de développer une méthode permettant de suivre simultanément l'évolution de la rhéologie et de la structure de la suspension. Ceci permettrait d'avoir des informations précieuses sur les mécanismes en jeu. Un autre axe d'étude serait de se concentrer sur la réponse temporelle de la suspension à des contraintes imposées. Bien que les réponses temporelles fussent enregistrées pendant les expériences de ce projet, ces données ne furent que peu exploitées.

Appendix A

Decomposition of the useful components

A.1 Components of F

Rectangular Coordinates (x, y, z)

Displacement functions:
$$x = x(x_0, y_0, z_0, t, t_0)$$
$$y = y(x_0, y_0, z_0, t, t_0)$$
$$z = z(x_0, y_0, z_0, t, t_0)$$

$$\begin{array}{lll} F_{xx} = \partial x/\partial x_0 & F_{xy} = \partial x/\partial y_0 & F_{xz} = \partial x/\partial z_0 \\ F_{yx} = \partial y/\partial x_0 & F_{yy} = \partial y/\partial y_0 & F_{yz} = \partial y/\partial z_0 \\ F_{zx} = \partial z/\partial x_0 & F_{zy} = \partial z/\partial y_0 & F_{zz} = \partial z/\partial z_0 \end{array}$$

Cylindrical Coordinates (r, θ, z)

Displacement functions:
$$r = r(r_0, \theta_0, z_0, t, t_0)$$
$$\theta = \theta(r_0, \theta_0, z_0, t, t_0)$$
$$z = z(r_0, \theta_0, z_0, t, t_0)$$

$$\begin{array}{lll} F_{rr} = \partial r/\partial r_0 & F_{r\theta} = \partial r/r_0\partial\theta_0 & F_{rz} = \partial r/\partial z_0 \\ F_{\theta r} = r\partial\theta/\partial r_0 & F_{\theta\theta} = r\partial\theta/r_0\partial\theta_0 & F_{\theta z} = r\partial\theta/\partial z_0 \\ F_{zr} = \partial z/\partial r_0 & F_{z\theta} = \partial z/r_0\partial\theta_0 & F_{zz} = \partial z/\partial z_0 \end{array}$$

Spherical Coordinates (r, θ, ϕ)

Displacement functions:
$$x = x(x_0, \theta_0, \phi_0, t, t_0)$$
$$\theta = \theta(x_0, \theta_0, \phi_0, t, t_0)$$
$$\phi = \phi(x_0, \theta_0, \phi_0, t, t_0)$$

$$
\begin{array}{ccc}
F_{rr} = \partial r/\partial r_0 & F_{r\theta} = \partial r/r_0\partial\theta_0 & F_{r\phi} = \partial r/r_0 \sin\theta_0\partial\phi_0 \\
F_{\theta r} = r\partial\theta/\partial r_0 & F_{\theta\theta} = r\partial\theta/r_0\partial\theta_0 & F_{\theta\phi} = r\partial\theta/r_0 \sin\theta_0\partial\phi_0 \\
F_{\phi r} = r\sin\theta\partial\phi/\partial r_0 & F_{\phi\theta} = r\sin\theta\partial\phi/r_0\partial\theta_0 & F_{\phi\phi} = r\sin\theta\partial\phi/r_0\sin\theta_0\partial\phi_0
\end{array}
$$

A.2 Components of the Equations of Motion

Rectangular Coordinates (x, y, z)

x-Component

$$
\rho(\frac{\partial v_x}{\partial t} + v_x\frac{\partial v_x}{\partial x} + v_y\frac{\partial v_x}{\partial y} + v_z\frac{\partial v_x}{\partial z}) = -\frac{\partial p}{\partial x} + (\frac{\partial \tau_{xx}}{\partial x} + \frac{\partial \tau_{yx}}{\partial y} + \frac{\partial \tau_{zx}}{\partial z}) + \rho g_x
$$

y-Component

$$
\rho(\frac{\partial v_y}{\partial t} + v_x\frac{\partial v_y}{\partial x} + v_y\frac{\partial v_y}{\partial y} + v_z\frac{\partial v_y}{\partial z}) = -\frac{\partial p}{\partial y} + (\frac{\partial \tau_{xy}}{\partial x} + \frac{\partial \tau_{yy}}{\partial y} + \frac{\partial \tau_{yz}}{\partial z}) + \rho g_y
$$

z-Component

$$
\rho(\frac{\partial v_z}{\partial t} + v_x\frac{\partial v_z}{\partial x} + v_y\frac{\partial v_z}{\partial y} + v_z\frac{\partial v_z}{\partial z}) = -\frac{\partial p}{\partial z} + (\frac{\partial \tau_{xz}}{\partial x} + \frac{\partial \tau_{yz}}{\partial y} + \frac{\partial \tau_{zz}}{\partial z}) + \rho g_z
$$

Cylindrical Coordinates (r, θ, z)

r-Component

$$
\rho(\frac{\partial v_r}{\partial t} + v_r\frac{\partial v_r}{\partial r} + \frac{v_\theta}{r}\frac{\partial v_r}{\partial \theta} - \frac{v_\theta^2}{r} + v_z\frac{\partial v_r}{\partial z}) = -\frac{\partial p}{\partial r} + (\frac{1}{r}\frac{\partial}{\partial r}(r\tau_{rr}) + \frac{1}{r}\frac{\partial \tau_{\theta r}}{\partial \theta} - \frac{\tau_{\theta\theta}}{r} + \frac{\partial \tau_{zr}}{\partial z}) + \rho g_r
$$

θ-Component

$$
\rho(\frac{\partial v_\theta}{\partial t} + v_r\frac{\partial v_\theta}{\partial r} + \frac{v_\theta}{r}\frac{\partial v_\theta}{\partial \theta} + \frac{v_\theta v_r}{r} + v_z\frac{\partial v_\theta}{\partial z}) = -\frac{\partial p}{\partial \theta} + (\frac{1}{r^2}\frac{\partial}{\partial r}(r^2\tau_{r\theta}) + \frac{1}{r}\frac{\partial \tau_{\theta\theta}}{\partial \theta} + \frac{\partial \tau_{\theta z}}{\partial z} + \frac{\tau_{\theta r} - \tau_{r\theta}}{r}) + \rho g_\theta
$$

z-Component

$$\rho(\frac{\partial v_z}{\partial t} + v_r\frac{\partial v_z}{\partial r} + \frac{v_\theta}{r}\frac{\partial v_z}{\partial \theta} + v_z\frac{\partial v_z}{\partial z}) = \\ -\frac{\partial p}{\partial z} + (\frac{1}{r}\frac{\partial}{\partial r}(r\tau_{rz}) + \frac{1}{r}\frac{\partial \tau_{\theta z}}{\partial \theta} + \frac{\partial \tau_{zz}}{\partial z}) + \rho g_z$$

Spherical Coordinates (r, θ, ϕ)

r-Component

$$\rho(\frac{\partial v_r}{\partial t} + v_r\frac{\partial v_r}{\partial r} + \frac{v_\theta}{r}\frac{\partial v_r}{\partial \theta} + \frac{v_\phi}{r\sin\theta}\frac{\partial v_r}{\partial \phi} - \frac{v_\theta^2 + v_\phi^2}{r}) = \\ -\frac{\partial p}{\partial r} + (\frac{1}{r^2}\frac{\partial}{\partial r}(r\tau_{rr}) + \frac{1}{r\sin\theta}\frac{\partial}{\partial \theta}(\tau_{\theta r}\sin\theta) + \frac{1}{r\sin\theta}\frac{\tau_{r\theta}}{\partial \phi} - \frac{\tau_{\theta\theta} + \tau_{\phi\phi}}{r}) + \rho g_r$$

θ-Component

$$\rho(\frac{\partial v_\theta}{\partial t} + v_r\frac{\partial v_\theta}{\partial r} + \frac{v_\theta}{r}\frac{\partial v_\theta}{\partial \theta} + \frac{v_\theta}{r\sin\theta}\frac{\partial v_\theta}{\partial \phi} + \frac{v_r v_\theta}{r} - \frac{v_\phi^2\cot\theta}{r}) = \\ -\frac{\partial p}{\partial \theta} + (\frac{1}{r^3}\frac{\partial}{\partial r}(r^3\tau_{r\theta}) + \frac{1}{r\sin\theta}\frac{\partial}{\partial \theta}(\tau_{\theta\theta}\sin\theta) + \frac{1}{r\sin\theta}\frac{\partial \tau_{\phi\theta}}{\partial \phi} + \\ \frac{\tau_{\theta r} - \tau_{r\theta} - \cot\theta\tau_{\theta\theta}}{r}) + \rho g_\theta$$

ϕ-Component

$$\rho(\frac{\partial v_\phi}{\partial t} + v_r\frac{\partial v_\phi}{\partial r} + \frac{v_\theta}{r}\frac{\partial v_\phi}{\partial \theta} + \frac{v_\phi}{r\sin\theta}\frac{\partial v_\phi}{\partial \phi} + \frac{v_\phi v_r}{r} + \frac{v_\theta v_\phi}{r}\cot\theta) = \\ -\frac{1}{r\sin\theta}\frac{\partial p}{\partial \phi} + (\frac{1}{r^3}\frac{\partial}{\partial r}(r^3\tau_{r\phi}) + \frac{1}{r\sin\theta}\frac{\partial}{\partial \theta}(\tau_{\theta\phi}\sin\theta) + \frac{1}{r\sin\theta}\frac{\partial \tau_{\phi\phi}}{\partial \phi} + \\ \frac{\tau_{\phi r} - \tau_{r\phi} + 2\cot\theta\tau_{\theta\phi}}{r}) + \rho g_\phi$$

A.3 Components of L

Reminding that $\mathbf{L} = (\nabla v)^T$, we got:

Rectangular Coordinates (x, y, z)

$$\begin{array}{lll} L_{xx} = \frac{\partial v_x}{\partial x} & L_{xy} = \frac{\partial v_x}{\partial y} & L_{xz} = \frac{\partial v_x}{\partial z} \\ L_{yx} = \frac{\partial v_y}{\partial x} & L_{yy} = \frac{\partial v_y}{\partial y} & L_{yz} = \frac{\partial v_y}{\partial z} \\ L_{zx} = \frac{\partial v_z}{\partial x} & L_{zy} = \frac{\partial v_z}{\partial y} & L_{zz} = \frac{\partial v_z}{\partial z} \end{array}$$

Cylindrical Coordinates (r, θ, z)

$$\begin{array}{lll} L_{rr} = \frac{\partial v_r}{\partial r} & L_{r\theta} = \frac{1}{r}\frac{\partial v_r}{\partial \theta} - \frac{v_\theta}{r} & L_{rz} = \frac{\partial v_r}{\partial z} \\ L_{\theta r} = \frac{\partial v_\theta}{\partial r} & L_{\theta\theta} = \frac{1}{r}\frac{\partial v_\theta}{\partial \theta} + \frac{v_r}{r} & L_{\theta z} = \frac{\partial v_\theta}{\partial z} \\ L_{zr} = \frac{\partial v_z}{\partial r} & L_{z\theta} = \frac{1}{r}\frac{\partial v_z}{\partial \theta} & L_{zz} = \frac{\partial v_z}{\partial z} \end{array}$$

Spherical Coordinates (r, θ, ϕ)

$$\begin{array}{lll} L_{rr} = \frac{\partial v_r}{\partial r} & L_{r\theta} = \frac{1}{r}\frac{\partial v_r}{\partial \theta} - \frac{v_\theta}{r} & L_{r\phi} = \frac{1}{\sin\theta}\frac{\partial v_r}{\partial \phi} - \frac{v_\phi}{r} \\ L_{\theta r} = \frac{\partial v_\theta}{\partial r} & L_{\theta\theta} = \frac{1}{r}\frac{\partial v_\theta}{\partial \theta} + \frac{v_r}{r} & L_{\theta\phi} = \frac{1}{r\sin\theta}\frac{\partial v_\theta}{\partial \phi} - \frac{v_\phi}{r}\cot\theta \\ L_{\phi r} = \frac{\partial v_\phi}{\partial r} & L_{\phi\theta} = \frac{1}{r}\frac{\partial v_\phi}{\partial \theta} & L_{\phi\phi} = \frac{1}{r\sin\theta}\frac{\partial v_\phi}{\partial \phi} + \frac{v_r}{r} + \frac{v_\theta}{r}\cot\theta \end{array}$$